PhD in Chemical Science and Technology

Cycle XXXII

INVESTIGATION OF MECHANICALLY INDUCED CO₂ STORAGE AND CONVERSION DRIVEN BY OLIVINE WEATHERING PROCESS

Scientific Disciplinary Sector: CHIM/02

PhD Student: Valeria Farina

Coordinator of the PhD Programme Prof. Stefano Enzo

Supervisor Prof. Gabriele Mulas

Final exam. Academic Year 2018 – 2019

Thesis defence: February 2020 Session

Contents

Chapter 1: Introduction

1.1   GENERAL INTRODUCTION

Fossil fuels are still today the primary energy source in the world. The continuous growth of energy demand has led to increased fuel consumption and then to the release of a huge amount of carbon dioxide, CO_2, into the atmosphere[1]. It is well known that CO_2 is the greenhouse gas which gives a major contribution to global warming. It is also recognized that natural processes cannot absorb all the anthropogenically produced carbon dioxide. As a consequence, the development of new technologies for capture and conversion is urgently required[2].

The Paris Agreement[3] set out the commitment to reduce greenhouse emissions and to limit climate change, limiting the global temperature rise to 1,5 °C. Only 153 of 197 parties of the United Nation Framework Convention on Climate Change (UNFCCC) ratified the agreement, covering 84,7% of greenhouse gas emissions at present, but these contributions are not enough to the necessary reductions by 2030 to meet the 2°C pathway (above the pre-industrial level)[4].

Human health is threatened by climate changes through direct and indirect pathways. Direct effects result from rising temperatures: it causes changes in the frequency and strength of storms, floods, droughts and heatwaves, with physical and mental health consequences. The indirect effects include changes in crop yields, burden and distribution of infectious disease, and climate-induced population displacement and violent conflict[5].

The potential benefits and opportunities of a response to climate change are enormous, including cleaning the air of polluted cities, delivering more

nutritious diets, ensuring energy, food, and water security, and alleviating poverty and social and economic inequalities[6].

The International Energy Agency (IEA) has predicted that the continuous growth in energy demand will lead to a change of roles by 2040: Middle East countries will become the major energy consumers while the US the major exporter[7]. Only the energy efficiency will halt the demand growth in advanced economies. In line with the objectives of the Paris Agreement, CO_2 emissions will be reduced by the expansion of renewable energy in the sustainable development scenario (Fig. 1.1)[8].

Global greenhouse gas emissions

Gigatons of carbon dioxide

Projections

No climate policies 4.1-4.8°C

Current policies 3.1-3.7°C

Pledges 2.6-3.2°C

2°C pathways

1.5°C pathways

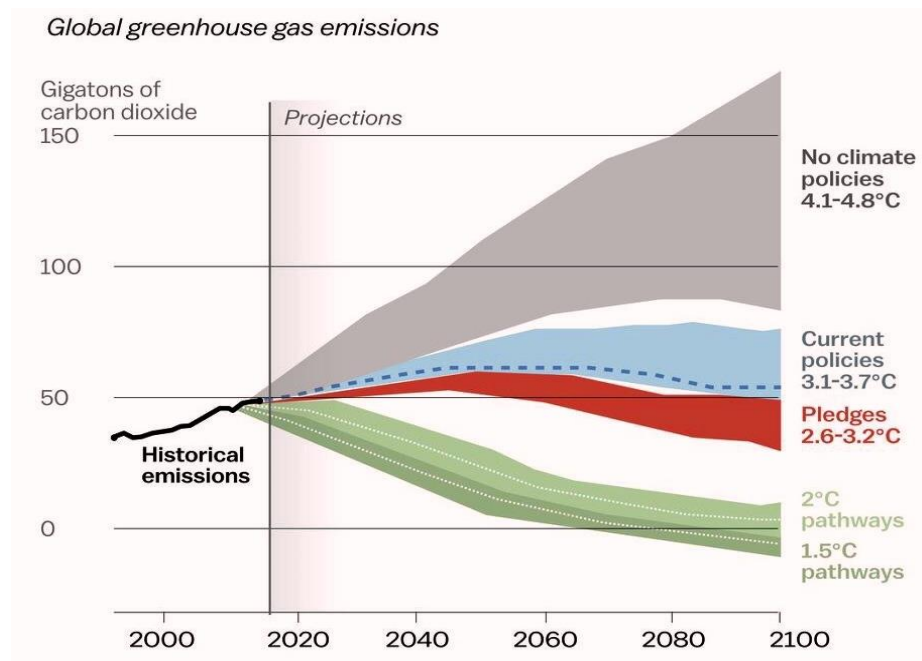**Historical emissions**

Figure 1.1: Potential greenhouse gas emissions up to the year 2100 (measured in gigatons of CO_2).

In this scenario, new and renewable energy will exceed conventional energy sources. So, in addition to the improvement of energy efficiency, the development of key technologies and strategies is required, including renewable energy, carbon capture storage technologies, etc.

Carbon capture and storage technologies were developed following the agreement taken on July 2009 by 17 partners of the Major Economies Forum (MEF) on Energy and Climate to the transition to a low-carbon economy, to promote economic growth as part of a vigorous response to climate change.

These technologies allow the capture of more than 90% of CO_2 emissions produced mainly from fossil fuels combustion in industrial processes and electricity generation. Captured CO_2 is transported (by pipeline, ship or road tanker) and securely stored underground, in depleted oil and gas fields or deep saline aquifer formation, that are located several kilometres below the Earth's surface. An alternative to CCS, or linked to it, are CO_2 Capture Utilization technologies (CCU): captured CO_2 is converted on different products via chemical, biochemical, photochemical or electrochemical reactions. These products may then be used as either feedstock for value-added chemicals (e.g. organic and inorganic carbonates, polymers, urea etc.), or as a medium for intermediate energy storage (e.g. methane, syngas). CCU technologies result in non-permanent products that are later converted back to CO_2 and may be interesting from an industrial production perspective but are not relevant for climate protection. They act as an enabler or supporter of CCS but cannot be seen as CO_2 abatement. However, CCU there must be a long-term storage component, such as the Enhanced Oil Recovery, EOR.

EOR is a well-established technology which consists of CO_2 injection in depleted oil fields. There are three large scale projects of EOR (Norway, Canada and Algeria) in which were stored 1 to 3 million metric tons of CO_2 annually for several years and that had allowed scientists to acquire the data needed to validate the capacity and potential impact of geologic CCS. In the United States, which accounts for 94% of worldwide CO_2/EOR production, about 63 million

metric tons of mostly naturally produced carbon dioxide are injected annually for this purpose[9].

Most of the potential uses of CO_2 are illustrated in the following diagram (Fig. 1.2)[10].
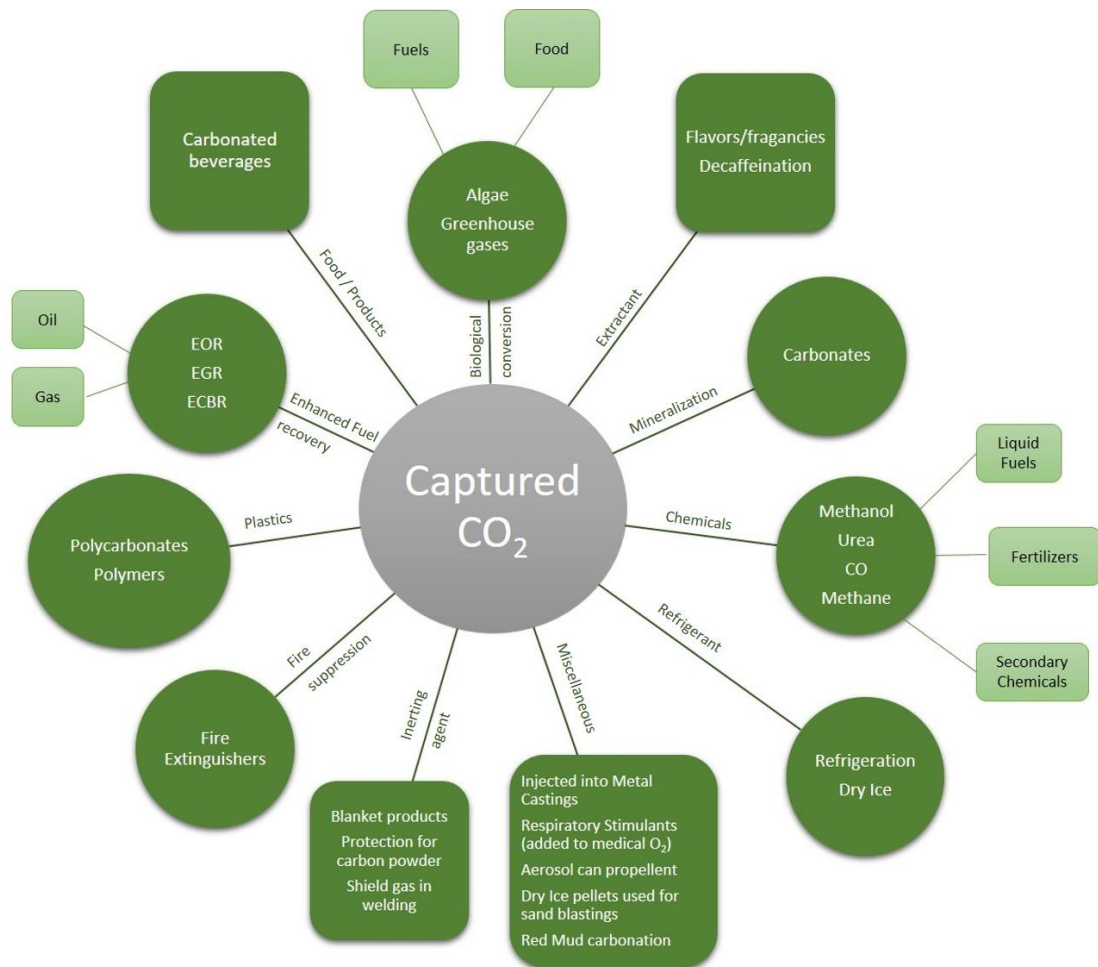
Figure 1.2: scheme of the different uses of captured CO_2.

CCU consumes about 115 million tons of CO_2 annually worldwide[11], a small amount compared to annual global carbon dioxide emissions of slightly more than 30 billion metric tons[12]. However, CO_2 recycling and conversion to chemicals are expected to increase from about 0.5 per cent of carbon dioxide emissions at present to 1–2 per cent of emissions in the future[13].

1.2 AIM OF THE THESIS

This context included the present project, which aims to study the conversion of CO_2 into hydrocarbons as a consequence of the interaction with Olivine in presence of water, simulating the *Serpentinization* process. Olivine is a natural mineral constituted by a solid solution of fayalite (Fe_2SiO_4) and forsterite (Mg_2SiO_4). In nature around 100 million tons of carbon per year, according to a slow weathering process, is bound by these minerals[14]. The CO_2 sequestration in natural silicates sometimes is accompanied by the occurrence of the *serpentinization* process. This is a widespread phenomenon on the Earth's mantle that occurs generally at temperatures less than $300°C$[14-17] and during which mineral-based silicates of Fe and Mg react with water to give H_2 and minerals of the serpentine group [$(Mg, Fe)_3Si_2O_5(OH)_4$] (Eq. 1.1). This involves the formation of extremely reducing fluids, rich in hydrogen, so any species present, such as inorganic C, can be reduced.

$6\ (Mg,Fe)_2SiO_4 + 12\ H_2O + 6\ CO_2\ \rightarrow$

$\qquad 2\ (Mg,Fe)_3[(Si)]_2O_5(OH)_4 + 2\ Fe_3O_4 + 8\ H_2 + 6\ [(MgCO)]_3 + 2\ SiO_2$ *Eq. 1.1*
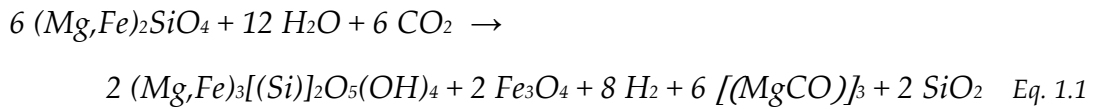
Therefore, CO_2 can react with H_2, through a Fischer-Tropsch type (FTT) or Sabatier mechanism, to form CH_4 and light hydrocarbons[15] (Eq. 1.2).

$$CO_2\ +\ 4\ H_2\ \rightarrow\ CH_4\ +\ 2\ H_2O \qquad\qquad \textit{Eq. 1.2}$$
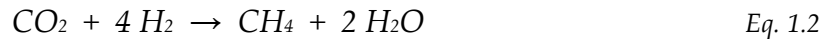
Although the whole process is thermodynamically favoured, the rate of the reaction is very slow, and, accordingly, the natural process does not allow the control of CO_2 emission levels into the atmosphere. Then, the possibility to increase the kinetics of such processes deserves interest, and, to this regard, preliminary treatment of the olivine mineral, such as mechanical activation, has been demonstrated to be successful. If, on the one hand, the CO_2 absorption

process during olivine serpentinization has been experimentally investigated, on the other hand, literature data[18-25] are not homogeneous and refer to the effects of mechanical activation on olivine, focusing mainly on its structural and surface transformation, in order to facilitate CO_2 storage. In particular, it has been shown that the mechanical grinding of olivine significantly increases its ability to form iron and magnesium carbonates making the CO_2 capture a potential stable storage method for long periods. The mechanical activation was found to be more effective if the treatment occurs in the presence of liquids such as water[26] or ethanol[27], as a consequence of the greater surface area generated in wet conditions.

Conversely, less attention has been paid, in such studies, to the chemical reduction of CO_2, to yield light hydrocarbons and corresponding oxygenated compounds. The present work just deals with such issues, and, for the first time to our knowledge, the attention has been focused on the mechanically induced production of methane and light hydrocarbons during the interaction between olivine and water under CO_2 atmosphere.

So, the purposes of this project are:

- a detailed study of the Olivine serpentinization process induced by mechanical grinding, and of the production of methane and hydrocarbons;
- investigate the mechanism of the different stages of the serpentinization process and their dependence on experimental conditions;
- quantify and optimize the production of methane and light hydrocarbons;
- evaluate potential applications.

REFERENCES:

[1]   N. Koukouzas et al. (2009), Sequestration of CO_2 in magnesium silicates, in Western Macedonia, Greece. *Int. J. Miner. Process.* **93**, 179–186.

[2]   P. Falkowski et al. (2000), The global carbon cycle: A test of our knowledge of earth as a system. *Science (80).* **290**, 291–296.

[3]   UNFCCC, New York: United Nations, **21932**, 1–32, (2015).

[4]   UNEP, The Emissions Gap Report 2016: A UNEP Synthesis Report. New Climate Institute (2016).

[5]   T. F. Stocker [ed.] et al. (2014), Climate change 2013: the physical science basis: Working Group. *Fifth Assess. Rep. Intergov. Panel Clim. Chang.* **5**.

[6]   N. Watts et al. (2018), The Lancet Countdown on health and climate change: from 25 years of inaction to a global transformation for public health. *Lancet* **391**, 581–630.

[7]   International Energy Agency, IEA. World Energy Outlook: Executive Summary. *Oecd/Iea* 11 (2018).

[8]   International Energy Agency, IEA. Energy Technology Perspectives 2017 - Executive Summary (2017).

[9]   U.S. Department of Energy, National Energy Technology Laboratory, NETL. Carbon Dioxide Enhanced Oil Recovery. 30 (2010).

[10]   U.S DOE, National Energy Laboratory, CO_2 Utilization Focus Area, http://www.netl.doe.gov/research/coal/carbon-storage/research-and-development/co2-utilization

[11]   The Carbon Dioxide Capture and Conversion (CO2CC) Program, The Catalyst Group Resources (2011).

[12]   U.S. Energy Information Administration, International Energy Outlook (2011).

[13]   U.S. Energy Information Administration, Global Energy & CO_2 Status report (2018).

[14]   E. H. Oelkers et al. (2008), Mineral carbonation of CO_2. *Elements* **4**, 333–337.

[15]   N. G. Holm et al. (2015), Serpentinization and the Formation of H_2 and CH_4 on Celestial Bodies (Planets, Moons, Comets). *Astrobiology* **15**.

[16]   T. M. McCollom et al. (2009), Thermodynamic constraints on hydrogen generation during serpentinization of ultramafic rocks. *Geochim. Cosmochim. Acta* **73**, 856–875.

[17]   A. Neubeck et al. (2011), Formation of H_2 and CH_4 by weathering of olivine at temperatures between 30 and 70°C. *Geochem. Trans.* **12**, 1–10.

[18]   R. A. Kleiv et al. (2006), Mechanical activation of olivine. *Miner. Eng.* **19**, 340–347.

[19]   P. Baláž et al. (2008), Structural changes in olivine $(Mg,Fe)_2SiO_4$ mechanically activated in high-energy mills. *Int. J. Miner. Process.* **88**, 1–6.

[20]   M. Fabian et al. (2010), The influence of attrition milling on carbon dioxide sequestration on magnesium-iron silicate. *Miner. Eng.* **23**, 616–620.

[21]   K. L. Sandvik et al. (2011), Mechanically activated minerals as a sink for CO_2. *Adv. Powder Technol.* **22**, 416–421.

[22] I. M. Power et al. (2013), Serpentinite carbonation for CO_2 sequestration. *Elements* **9**, 115–121.

[23] E. Turianicová et al.(2013), A comparison of the reactivity of activated and non-activated olivine with CO_2. *Int. J. Miner. Process.* **123**, 73–77.

[24] J. Li et al. (2015), Ultra-fine grinding and mechanical activation of mine waste rock using a high-speed stirred mill for mineral carbonation. *Int. J. Miner. Metall. Mater.* **22**, 1005–1016.

[25] I. Rigopoulos et al. (2015), Enhancing the rate of ex situ mineral carbonation in dunites via ball milling. *Adv. Powder Technol.* **27**, 360–371.

[26] E. Turianicová et al. (2008), A possible way to storage carbon dioxide on mechanically activated olivine $(Mg, Fe)_2SiO_4$. *VI Int. Conf. Mechanochemistry Mech. Alloy.* 316–319.

[27] I. Rigopoulos et al. (2015), Carbon dioxide storage in olivine basalts: Effect of ball milling process. *Powder Technol.* **273**, 220–229.

Chapter 2: Background

2.1 CO_2 UTILIZATION

It is well known that the accumulation of carbon dioxide, CO_2, in the atmosphere is mainly due to the excessive use of fossil fuels that still today represents the main source of energy on a global scale. As shown by many scientific studies, CO_2 is the most responsible gas for the greenhouse effect and therefore of global warming. Global emissions of CO_2 have been steadily increasing in the past decades and reached values 60% above the levels of 1990, when the Kyoto Protocol was stated. In order to limit the global temperature rise, CO_2 emissions should be reduced by at least 50% by 2050[1,2].

Among the various strategies under investigation, Carbon Capture Storage (CCS) and, more recently, Carbon Capture Utilization (CCU) have attracted the attention of scientists worldwide. The aim of such approaches is to capture emissions from point sources but the main difference is the destination of captured CO_2. While in CCS it is transferred to a suitable site for long-term storage, in CCU it is converted into valuable products (e.g. chemicals and fuels): both the strategies are expected to contribute to mitigating climate changes[3-10]. Compared to conventional feedstocks, CO_2 has the advantage to be a renewable source, cheaper and non-toxic[11]. The conversion of CO_2 is energy-intensive due to its thermodynamic stability[3,11], but the continuous increase of fossil-fuels prices could promote the application of these technologies.

There are three main types of CO_2 capture options: post-combustion, pre-combustion and oxyfuel combustion. In post-combustion capture, CO_2 is separated from the waste gas stream through adsorption into solvents and solid sorbents, after the conversion from the carbon source.

In pre-conversion capture, CO_2 generated in an intermediate reaction of a conversion process as an undesired co-product, like in the production of ammonia and coal gasification in power plants[5,16,17], is captured using physical solvents[16-19]. Finally, the oxy-fuel combustion can only be applied to a combustion process, such as power generation in fossil-fuel plants. Fuel is burned with pure oxygen to produce gas with high CO_2 concentrations, free from nitrogen and its derivatives[1].

Once CO_2 is captured, is then compressed and shipped or pipelined to be stored in the ground, ocean or as a mineral carbonate[5,8,20]. As for the CCS, i.e. CO_2 geological storage, it involves the injection of CO_2 into geological formations such as depleted oil and gas reservoirs at great depths. Such sequestration technique is, at present, probably one of the most promising options due to the previous experience by the oil and gas industry. In fact, the industry has a good understanding of the structural characteristics and behaviour of depleted oil and gas reservoirs and the existing well-drilling and injection techniques can be adapted for carbon storage applications[5] (e. g. CO_2-injection at Sleipner)[21,22]. The main issues with CO_2 storage are their possible leaks and the related damage that could be caused by a concentrated stream escaped into the environment. This possibility depends on the permeability of the geological structure and its faults or defects. According to the literature, annual leakage rates are in the range from 0.00001% to 1%[5,16,17].

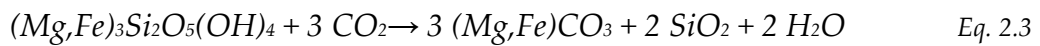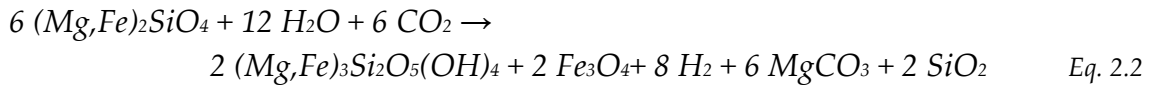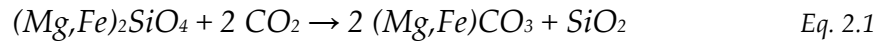Moreover, mineral carbonation, also known as 'mineral sequestration', can be considered as a storage and utilization option because involves CO_2 conversion into carbonates through the reaction with metal oxides, such as magnesium or calcium oxide[5,20]. Carbonation is an exothermic reaction that releases enough heat to make the whole process, at least in theory, self-sustaining[22]. The main

advantage of mineral carbonation is the formation of stable carbonates capable of storing CO_2 for long periods, without the risk of CO_2 leakage as in CCS[3,5,20].

The only limitation of mineral carbonation is the slow reaction kinetics on which the research has focused, to accelerate the carbonation rates. Compared with other approaches, the mineral carbonation has several advantages: permanent CO_2 storage, a wide range of materials that can be used and carbonate products environmentally friendly[23-25].

Magnesium and calcium are usually found in nature as silicate minerals such as serpentine, olivine and wollastonite. Direct carbonation takes place under high-pressure conditions in both dry or aqueous media.

Olivine and Serpentine are the most promising minerals for carbon sequestration because of their high contents of magnesium. The main carbonation reactions of these two minerals are described by the following reactions (Eq. 2.1-2.3):

$$(Mg,Fe)_2SiO_4 + 2\ CO_2 \rightarrow 2\ (Mg,Fe)CO_3 + SiO_2 \qquad\qquad Eq.\ 2.1$$

$$6\ (Mg,Fe)_2SiO_4 + 12\ H_2O + 6\ CO_2 \rightarrow$$
$$2\ (Mg,Fe)_3Si_2O_5(OH)_4 + 2\ Fe_3O_4 + 8\ H_2 + 6\ MgCO_3 + 2\ SiO_2 \qquad Eq.\ 2.2$$

$$(Mg,Fe)_3Si_2O_5(OH)_4 + 3\ CO_2 \rightarrow 3\ (Mg,Fe)CO_3 + 2\ SiO_2 + 2\ H_2O \qquad Eq.\ 2.3$$

The mineral carbonation, proposed by Seifritz in 1990[26], can be carried out in two different conditions: in-situ and ex-situ[27,28]. In-situ mineral carbonation reaction occurs underground, in hydrothermal conditions, after the injection of CO_2 into mantle basalt and peridotite deposits. Conversely, ex-situ mineral carbonation is realized in a laboratory or industry where the operative conditions can be easily controlled[29] and CO_2 can be used as a carbon source for chemical production or as a building material[4,30].

There are three pre-treatment options in mineral carbonation[31]: mechanical, thermal and chemical activation, which aim to enhance the carbonation rate of

silicates through the destruction of their crystal structure[32]. Among these, mechanical activation is at present the most effective method for olivine and serpentine mineral[33]. It can produce large surface area and disorder the crystal structure, improving the extent of carbonation. Numerous studies have been focused on the mechanical activation of magnesium-iron silicates and various operative conditions have been tested[34-44].

Similarly, enhanced oil recovery (EOR) and enhanced coal-bed methane recovery (ECBM) can be considered as storage and utilization methods, where CO_2 is used to extract crude oil from an oil field, or natural gas from unmineable coal deposits, respectively. As mentioned earlier, as an alternative to storage, captured CO_2 can be used as a commercial product, either directly or after conversion. The direct utilisation includes the use in the food and drinks industry as a carbonating agent, preservative, packaging gas and as a solvent for the extraction of flavours and in the decaffeination process[45]. Other applications are related to the pharmaceutical industry where CO_2 can be used as a respiratory stimulant or as an intermediate in the synthesis of drugs[11,45]. CO_2 can be also converted into chemical and fuels, through carboxylation reaction where is used as a precursor for organic compounds like carbonates or polymers, or in reduction reactions to produce chemicals such as methane, methanol, etc[3,4,11].

2.2 OLIVINE

Olivine is a group of silicate minerals that constitute mafic and ultramafic igneous rocks such as basalt, gabbro, dunite, diabase, and peridotite. Ultramafic rocks constitute more than 84% in volume of the terrestrial mantle, thus making Olivine one of the most abundant minerals on Earth. Figure 2.1 schematizes the
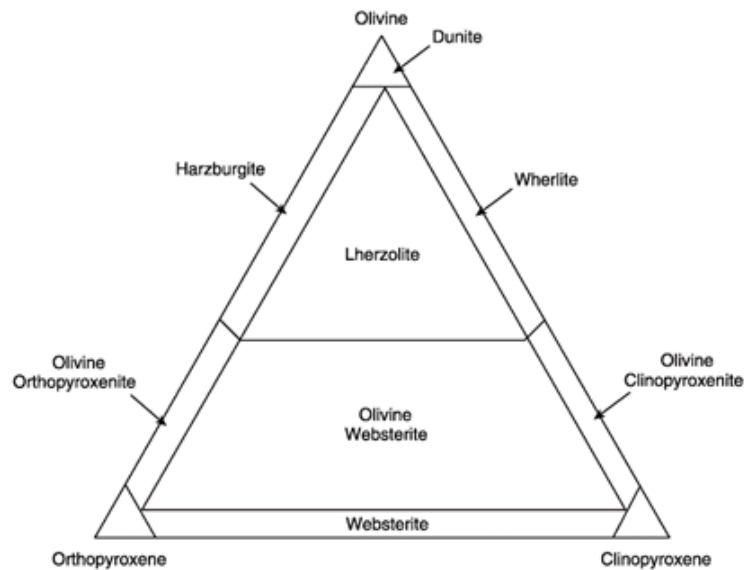
composition of ultramafic rocks[46].

Figure 2.1: Classification diagram for ultramafic rocks according to the percentages of Olivine, Orthopyroxene and Clinopyroxene.

Olivine minerals consist of a solid solution of Fayalite (Fe_2SiO_4) and Forsterite (Mg_2SiO_4), in different percentages; they are characterized by a chemical composition type A_2SiO_4, where A is generally Fe or Mg or more rarely Ca, Mn or Ni, and their crystal has an Orthorhombic structure (Fig. 2.2).
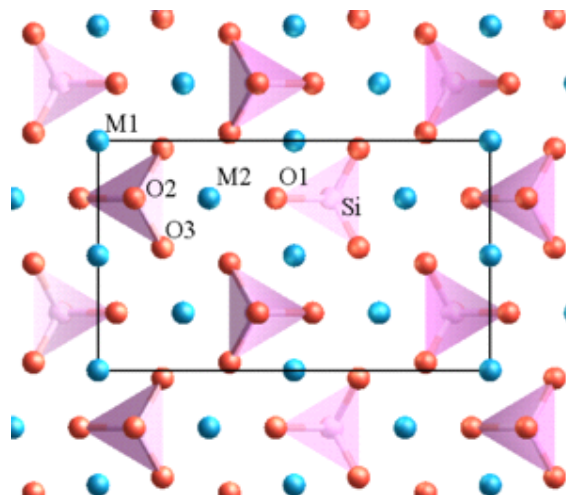

Figure 2.2: Structure of Olivine in atomic scale.

Monticellite ($CaMgSiO_4$), Kirschsteinite ($CaFeSiO_4$) and Tephroite (Mn_2SiO_4)[47] are secondary minerals of the Olivine group.

Generally, the term Olivine is used only for Iron and Magnesium mixed silicates, represented with the chemical formula $(Fe,Mg)_2SiO_4$, and has been assigned by the geologist because of the typical green colouration of the Peridotite gems, with a composition close to the pure Forsterite, already used by the ancient Egyptians[46]. However, Olivine can also take yellow-brown colour depending on the percentage of Iron in the structure[47]. Olivine crystals belong to the orthorhombic system with a *pbnm* spatial group. Their structure is constituted by isolated tetrahedra of $[SiO_4]^{4-}$ connected each other by interstitial metallic cations, typical of orthosilicates[48].

During the magma cooling process, Olivine is one of the first minerals that crystallize due to its high crystallization temperature (around 1200°C). If the cooling is slow, Olivine crystals deposit to the bottom of the magma chamber, because of their relatively high density. This process brings to the formation of rocks Olivine rich. Olivine crystals are also found in Xenoliths, inside volcanic rocks, while Forsterite can also be found in marbles formed by the metamorphism of dolomitic limestone[48].

Is also an abundant mineral in the lower portion of many ophiolites, slabs of oceanic crust (with part of the upper mantle attached) that have been thrust up onto an island or a continent. Because it is so easily altered by weathering and transformed into Serpentine, Olivine is not a common mineral in sedimentary rocks and is only an abundant constituent of sand or sediment of deposit very close to the source.

2.2.1 SERPENTINIZATION AND METHANE FORMATION

The Latin term "Serpentine", was attributed for the first time by Georgius Agrigola in 1564 in allusion to the similar appearance of the serpentinitic rocks to the snake-skin. As for Olivine, Serpentine is not a single mineral but a group of minerals with similar characteristics and structures[49,50].

They are phyllosilicates of general formula $X^{2-3}Si_2O_5(OH)_4$, where X = Mg, Fe, Ni, Al, Zn, Mn; in addition, as in silicates, the silicon atoms of the crystalline lattice can be partially replaced by atoms of aluminium and iron, resulting in excess of negative charge balanced by ions like K^+, Na^+, Ca^{2+}, Mn^{2+}.

The most representative members of the Serpentine group are Antigorite $((Mg,Fe)_3Si_2O_5(OH)_4)$, Chrysotile $(Mg_3Si_2O_5(OH)_4)$ and Lizardite $(Mg_3Si_2O_5(OH)_4)$. The structure of these minerals is characterised by a repetition of two layers, tetrahedral (SiO_4) and octahedral $(Mg(OH)_2)$, and an interlayer space that may be empty or filled with molecules of water and/or cations, depending on the nature of its charge. As a function of the distortion and disposition of these two layers we will have different varieties of serpentine. In phyllosilicates, each octahedrons layer possesses three possible sites, which, in the case of the Serpentine Group minerals, are occupied by three bivalent reactions; this structure is typical of tri-octahedral phyllosilicates. Figure 2.3 shows a schematic representation of the repetition of the layers[51,52].

This group of minerals is formed in nature by the hydration processes of olivine-rich rocks, from which the name *Serpentinization* is derived. Because of this process, the formed rocks contain about 13% of water.

These rocks, abundant in the ophiolitic contexts, are part of the so-called green stones, used in many of the ancient cultures as building materials, as well as ornamental stones utilized in jewellery and in the furnishings. They played an essential role in numerous geological contexts, for example, due to the layered

structure, during the aseismic sliding of the plaque margins, they act as lubricants and contribute to the geochemical cycle of the subduction zones[51].

Due to its fibrous nature and high heat resistance, the Chrysotile, known as white asbestos, was widely used until the '80s to produce the cement-asbestos mixture (whose trade name was Eternit) for the insulation of buildings, roofs, ships; as material for the building industry (tiles, floors, piping, paints); in the suits of firefighters, in cars (paints, mechanical parts), but also for the manufacture of ropes, plastics and cartons. In addition, asbestos dust has been widely used as an adjuvant in wine filtration. But now, its use is prohibited in many countries because of its confirmed harmfulness to health.
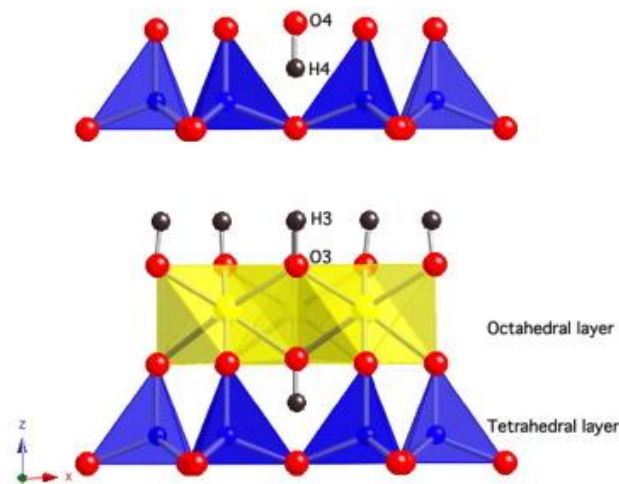
Figure 2.3: Structure of Serpentine.

The genesis of Serpentinites derives from the metamorphic process of mafic and ultramafic rocks rich in olivine, which are more common at the borders of divergent plaques and in hot-spot inside the tectonic plate centres[47]. These conditions lead to massive serpentinization phenomena after the interaction between rocks and water. For example, along the oceanic ridges, every year are emitted cubic kilometres of basaltic magmas that coming into direct contact

with the water of the ocean floor. In this context of oceanic growth is the seawater responsible for the serpentinization process. In particular, serpentinization is favoured mainly in slow diffusion dorsals, in which the episodic mag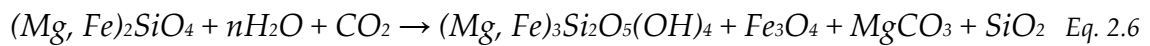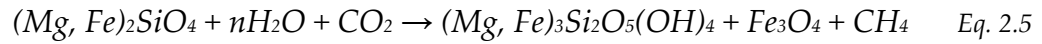matic activity allows the outcrop of the suboceanic mantle[52]. In fact, as the thickness of the crust is extremely low, fluids can penetrate deeply, influencing the underlying peridotites[53]. Another case affecting the ocean depths is the serpentinization in subduction contexts, where the formation of large faults, which can reach a depth of 20 km, allow the circulation of fluids in the upper part of the lithospheric mantle.

The hydration of mafic and ultramafic minerals also leads to the formation of secondary minerals. As already mentioned, different minerals can be formed depending on the environmental conditions and on the composition of the rocks; some of them may originate both pre and post serpentinization, acting as bearing minerals and often balance iron content[54]. In a purely magnesiferous system, the serpentinization process is described by Equation 2.4:

$$6\ (Mg,Fe)_2SiO_4 + 7\ H_2O\ \rightarrow\ 3\ (Mg,Fe)_3Si_2O_5(OH)_4 + Fe_3O_4 + H_2 \qquad Eq.\ 2.4$$
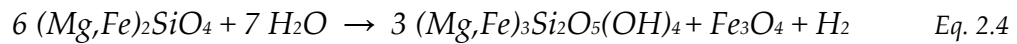
This process occurs at temperatures lower than 150°C and very high pH value (>10) conditions. It results in the oxidation of ferrous iron from olivine to form ferric iron in magnetite (Fe_3O_4) and other minerals, with a corresponding reduction of the protons of the water to give molecular hydrogen. This oxidation-reduction reaction is exothermic and leads to the formation of reducing fluids rich in hydrogen: one cubic meter of olivine can produce approximately 500 moles of H_2[55]. During the serpentinization process, rocks go through a volume expansion of 20-40%, due to the enormous quantity of water incorporated. This causes rock cracks and therefore the continuous exposure of the new reactive surface to water.

The hydrogen released from the serpentinization process may react with the dissolved CO_2 in the seawater, in highly reduction conditions, to form methane and other hydrocarbons. On the other hand, it is precisely CO_2 that can be fixed in the form of carbonates. Such serpentinization reactions in the presence of CO_2 can be described by the following equations (Eq. 2.5, 2.6):

$$(Mg, Fe)_2SiO_4 + nH_2O + CO_2 \rightarrow (Mg, Fe)_3Si_2O_5(OH)_4 + Fe_3O_4 + CH_4 \qquad Eq.\ 2.5$$

$$(Mg, Fe)_2SiO_4 + nH_2O + CO_2 \rightarrow (Mg, Fe)_3Si_2O_5(OH)_4 + Fe_3O_4 + MgCO_3 + SiO_2 \quad Eq.\ 2.6$$

The increase of the pH in the liquids, affected by the serpentinization, favours the precipitation of carbonates and, in some cases, can lead to the formation of chimney-shaped structures tens of meters tall like those of the Lost City, reported in Figure 2.4[56].
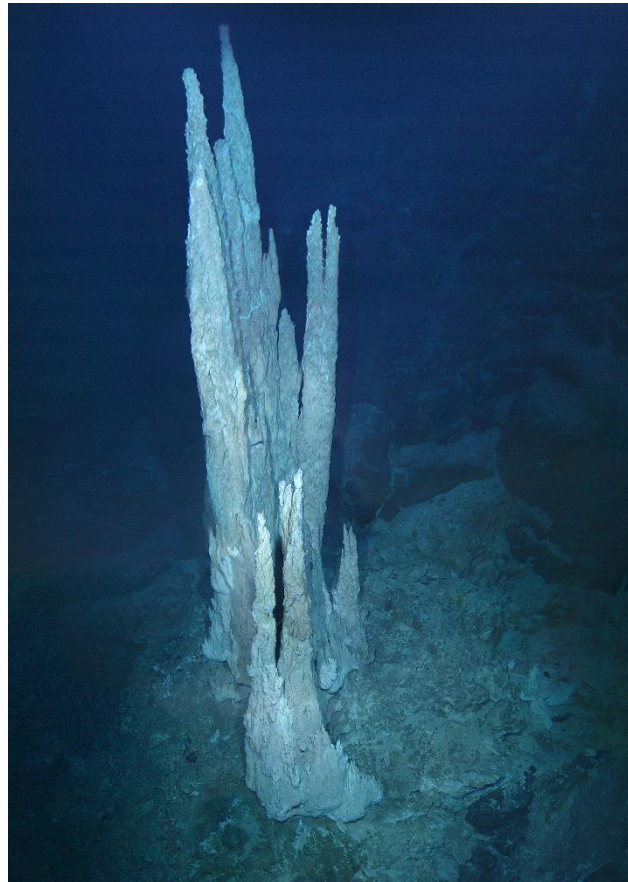

Figure 2.4: Carbonate chimney in The Lost City hydrotermal fields.

In this site, serpentinization has been going on for at least 30000 years supporting an ecosystem that ranges from colonies of micro-organisms to small invertebrates[56]; this suggests that this process could contribute to the formation and evolution of the first forms of life on Earth[57]. As a matter of fact, the serpentinization process produced abundant organic matter and also provided energy and carbon for the microbial ecosystem. These conditions made serpentinite an ideal focus for the study of the origin of life on Earth and other planetary bodies. The key reason is that hydrogen and methane represent the energy source for the metabolism of some microorganism[58]. Moreover, the high hydrogen release and the strong reducing conditions arising from the serpentinization process are favourable thermodynamic conditions for the abiogenic synthesis of organic matter like methane, alcohols, carboxylic acid and amino acids[59-62].

Different experiments pointed out that the production of H_2 and the following formation of methane is not a simple process, due to many variables such as the formation of secondary minerals, temperature and pressure conditions, pH and carbonate saturation[63-68]. First of all, the content of Fe and Mg in olivine play a fundamental role in the stability of the starting mineral and in the quantity of hydrogen that can be produced. Generally, the greater is the fayalitic component and the percentage of oxidizable iron, the greater is the corresponding quantity of potentially liberated H_2[67]. Thermodynamic studies conducted by Oze and Sharma[69] showed that the serpentinization of Mg-rich olivines, like that characteristic in the Earth's mantle, is thermodynamically favourable. While the content of Fe greater than 50% makes the process unfavourable, with H_2 production lower than what is expected by stoichiometry. However, it is necessary to point out that such modelling studies

are based on thermodynamic equilibrium conditions, far from the non-equilibrium ones typical of this geochemical process[58].

As discussed above, olivine hydrolysis generates hydrogen which can reduce the inorganic carbon through processes such as the FTT (Fischer-Tropsch-Type) synthesis[64,70-74] that can be summarized by the following reactions (Eq. 2.7 and 2.8):

$$CO_2 + 4H_2 \rightarrow CH_4 + 2H_2O \qquad \text{Eq. 2.7}$$

$$CO + 3H_2 \rightarrow CH_4 + H_2O \qquad \text{Eq. 2.8}$$

Fischer Tropsch synthesis is a catalytic reaction widely used in oil industry to synthesize methane and long-chain alkanes from H_2 and CO. Commercial catalysts used for FT process are metals such as Fe, Ni, Co, Ru, in the native state or their alloys, or their oxides such as magnetite and chromite[54]. These together with Ni-Fe alloys are quite common in hydrothermal sites. Conversely, the formation of methane from direct reduction of CO_2 and through the use of an appropriate catalyst is a specific case of the Fischer Tropsch process, known as the *Sabatier methanation process*.

According to various reports, FTT processes can also occur in absence of catalysts by exploiting the surface of the mineral such as silica[75], smectite[76] and mixtures of smectite and alumina[77], some of which are produced directly from the hydrolysis of basalts and ultramafic rocks.

Due to the complexity of the process, related to the many variables involved, laboratory experiments have helped to focus on various aspects.

For example, Jones et al.[65] carried out different tests to verify the effect of carbonate saturation on olivine hydrolysis under conditions similar to ocean hydrothermal systems. In particular, reactions were performed at 200°C and 300 bar in synthetic seawater, obtained by dissolving in deionized water KCl,

CaCl$_2$ and NaCl, excluding the presence of sulfur to simplify the system. The experiments were carried out on samples containing different amounts of NaHCO$_3$, performing periodic monitoring of CH$_4$ and H$_2$ by gas chromatography, pH, as well as Ca, Fe and Mg ion concentrations in solution. Moreover, to facilitate the carbon reduction to methane, chromite was added to the olivine in an unspecified amount. The presence of chrysotile in the residual powders demonstrates that the serpentinization process occurred in all the samples.

However, the production of H$_2$ and therefore of CH$_4$ in carbonate saturation conditions (experiment 3, Fig. 2.5) is lower than that observed in absence of the same (experiment 1, Fig. 2.5). This demonstrates that in the presence of excess CO$_3^{2-}$ ions, Fe^{2+} is rapidly incorporated to form carbonates, silicates and hydroxides, rather than being oxidized to Fe^{3+}.
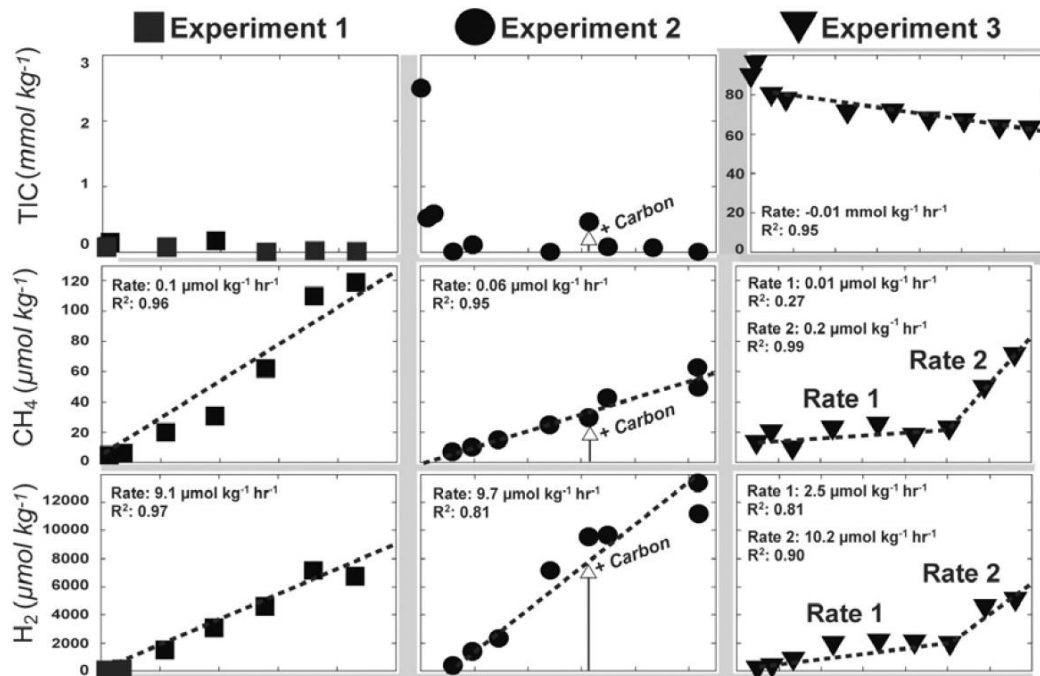

Figure 2.5: measurements related to toal inorganic carbon, methane and hydrogen in absence of NaCO$_3$ (Exp. 1) and in saturation conditions (Exp. 3).

In particular, the redox process becomes competitive with the carbonation process only when the concentration of carbonate in solution decreases. So, the production of H_2 is necessary for the following generation of methane. Although the saturated carbonate sample shows high contents of total inorganic carbon, the formation of methane begins only after the release of appreciable quantities of hydrogen.

This effect is also confirmed by the fact that the formation of magnetite, containing Fe^{3+}, generally associated with the release of H_2, is suppressed in the saturated carbonate solution.

However, it is necessary to specify that Fe^{3+} can also be included within the serpentine, thus not leading to the formation of appreciable quantities of magnetite. This result was recently reported by Klein et al. concerning a study on rock samples associated with serpentinization processes in low-temperature conditions[78].

Experiments conducted by Neubeck et al.[67] have revealed that the evolution of hydrogen and methane related to olivine hydrolysis can occur at temperatures below 100°C, although the slower kinetics. In particular, experiments at 30, 50 and 70°C have shown a linear increase in the concentration of methane over time, not showing an appreciable dependence on pH. Moreover, the evolution of gas is linearly correlated with the concentration of silicon in solution, confirming the direct dependence on olivine hydrolysis.

Related to Mg, Ni and Fe ions, it is shown a not clear dependence on time and therefore on the progress of serpentinization. In particular, below 70°C, the concentrations of the ions increased with time while at 70°C the trend is the opposite. This was rationalized by Neubeck et al. as a consequence of precipitation of secondary minerals or different processes like chelation and flocculation. The XRD and SEM (EDAX) analysis have shown the presence of

both chromite and magnetite, which would justify the low temperatures at which methane production was observed. The potential role of FTT catalyst for chromite in hydrothermal conditions has been highlighted by Foustoukos et al.[68] through experiments based on synthetic seawater added with labelled $NaCO_3$ ($\approx$99% ^{13}C) at 390°C and 400 bar. Cr_2O_3 and FeO were added in excess to the solution in order to facilitate the formation of $FeCr_2O_4$ and generate considerable amounts of hydrogen. High concentrations of $^{13}CH_4$ were detected, confirming the FTT process. Furthermore, moderate quantities of propane and ethane were observed, demonstrating the ability of the chromite to improve the quantity of hydrocarbons produced. This is shown in Figure 2.6, where the kinetics of released propane in the presence of chromite and FeO are compared. Despite the results obtained by Foustoukos et al., these are not be confirmed by recent studies performed by Oze et al.[66].
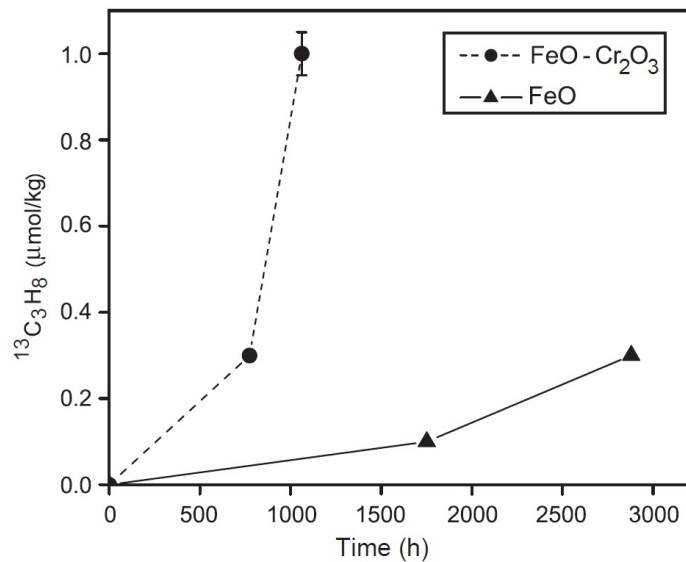

Figure 2.6: abiotic propane formation in hydrothermal conditions in presence of FeO and FeO with chromite.

They compared the production of methane during olivine serpentinization with pure olivine and with the addition of 1% of chromite, without finding

differences. They concluded that in such quantities, chromite does not act as a catalyst for the process, while a positive effect could be related to the presence of magnetite, that is formed by the reaction.

Figure 2.7 shows the trend of H_2/CH_4 ratio as a function of time, for both studies. As can be seen, initially the ratio is greater than 1, because of the higher hydrogen production compared to methane. The initial trend indicates that the FTT conversion is really slow, due to the low quantity of magnetite produced. The consequent increase in magnetite production speeds up the conversion and the H_2/CH_4 ratio decrease until the methane production reaches the maximum velocity. When the hydrogen excess has been consumed, the ratio decreases to a constant value. Oze et al. also suggest that high values of H_2/CH_4 ratio could be used as an index of abiotic methane production characteristic of serpentinization sites. The non-equilibrium conditions, typical of these systems, would involve high amount of hydrogen which could be not converted into hydrocarbons on time.
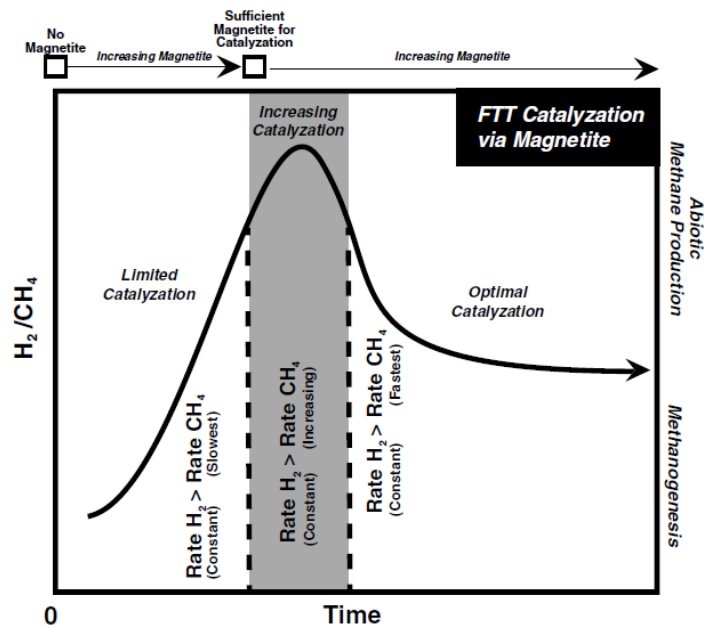

Figure 2.7: H_2/CH_4 ratio as a function of time, related to the magnetite formation.

2.3   THESIS PURPOSE

Our effort arises from the considerable scientific interest recently devoted to the capacity of ultramafic rocks to fix carbon dioxide and correlated chemical processes, which involve the transformation of CO_2 to chemical fuels or more complex systems.

In this specific context, the present work aims to give new insights into the study of the mechanically activated reaction, by BM technique, between olivine and CO_2 in presence of water. To the best of our knowledge, for the first time, the evolution of CH_4 and light hydrocarbons upon in situ ball milling of olivine under CO_2 atmosphere is presented in detail. However, even if the role of mechanical processing in activating liquid-solid and gas-solid interactions has already been established[79-85], a mechanochemical approach to the generation of light hydrocarbons from olivine powders has not been reported so far. Benefits of the ball milling process to enhance the carbon dioxide sequestration in olivine basalts and mine wastes have been clary demonstrated as corroborated by the specific literature[39,86-94].

Experimental findings evidence that serpentinization can be mechanically activated leading to the formation of hydrogen and, in a second step, to light hydrocarbons, three/four orders of magnitude higher respect to the thermally activated process. Furthermore, the structural and microstructural characterization confirms the benefit of ball milling in increasing the overall affinity of olivine toward carbon capture. These findings are of potential interest to a large audience because suggest a new approach for the conversion of carbon dioxide to light hydrocarbons. Furthermore, such results suggest that carbon conversion can occur during *in situ* ball milling of olivine under relatively low pressure of CO_2. This one-step approach represents a possible alternative to high temperatures and/or high pressures CO_2 carbon capture and

utilization process, CCU, already reported for different preactivated silicates. Finally, not less important, this work can shed light on aspect related with the origin of life, investigating the implications of mechanical effects, commonly expected in earthquakes, on the generation of methane and more complex nitrogen/carbon-based systems, in ultramafic rocks.

REFERENCES:

[1]   R. M. Cuéllar-Franca et al. (2015), Carbon capture, storage and utilisation technologies: A critical analysis and comparison of their life cycle environmental impacts. *J. CO$_2$ Util.* **9**, 82–102.

[2]   T. F. Stocker [ed.] et al. (2014), Climate change 2013: the physical science basis: Working Group. *Fifth Assess. Rep. Intergov. Panel Clim. Chang.* **5**.

[3]   P. Styring et al. (2011), Carbon Capture and Utilisation in the green economy. Centre for Low Carbon Futures.

[4]   P. Markewitz et al. (2012), Worldwide innovations in the development of carbon capture technologies and the utilization of CO$_2$. *Energy Environ. Sci.* **5**, 7281–7305.

[5]   B. Metz et al., IPCC, 2005: IPCC Special Report on Carbon Dioxide Capture and Storage. MRS Bulletin.

[6]   D. Weisser (2007), A guide to life-cycle greenhouse gas (GHG) emissions from electric supply technologies. *Energy* **32**, 1543–1559.

[7]   E. G. Hertwich et al. (2008), Life-cycle Assessment of Carbon Dioxide Capture for Enhanced Oil Recovery. *Chinese J. Chem. Eng.* **16**, 343–353.

[8]   C. Cooper (2009), A technical basis for carbon dioxide storage. *Energy Procedia* **1**, 1727–1733.

[9]   S. Nagashima et al. (2011), Life cycle assessment performed on a CCS model case in Japan and evaluation of improvement facilitated by heat integration. *Energy Procedia* **4**, 2457–2464.

[10]   P. Zapp et al. (2012), Overall environmental impacts of CCS technologies-A life cycle approach. *Int. J. Greenh. Gas Control* **8**, 12–21.

[11]   K. M. K. Yu et al. (2008), Recent advances in CO$_2$ capture and utilization. *ChemSusChem* **1**, 893–899.

[12]   T. Kuramochi et al. (2012), Comparative assessment of CO$_2$ capture technologies for carbon-intensive industrial processes. *Prog. Energy Combust. Sci.* **38**, 87–112.

[13]   B. J. Maring et al. (2013), A new simplified pressure/vacuum swing adsorption model for rapid adsorbent screening for CO$_2$ capture applications. *Int. J. Greenh. Gas Control* **15**, 16–31.

[14]   S. Krishnamurthy et al. (2014), CO$_2$ Capture from Dry Flue Gas by Vacuum Swing Adsorption: A Pilot Plant Study. *AIChE J. 60*, **5**, 1830–1842.

[15]   S. Sung et al. (2014), Highly efficient carbon dioxide capture with a porous organic polymer impregnated with polyethylenimine. *J. Mater. Chem. A* **2**, 13245–13249.

[16]   B. Singh et al. (2011), Comparative life cycle environmental assessment of CCS technologies. *Int. J. Greenh. Gas Control*.

[17]   M. Pehnt et al. (2009), Life cycle assessment of carbon dioxide capture and storage from lignite power plants. *Int. J. Greenh. Gas Control*.

[18]   N. A. Odeh et al. (2008), Life cycle GHG assessment of fossil fuel power plants with carbon capture and storage. *Energy Policy* **36**, 367–380.

[19]   P. Viebahn et al. (2007), Comparison of carbon capture and storage with renewable energy technologies regarding structural, economic, and ecological aspects in Germany. *Int. J. Greenh. Gas Control* **1**, 121–133.

[20]   L. Li et al. (2013), A review of research progress on CO_2 capture, storage, and utilization in Chinese Academy of Sciences. *Fuel* **108**, 112–130.

[21]   D. Y. C. Leung et al. (2014), An overview of current status of carbon dioxide capture and storage technologies. *Renewable and Sustainable Energy Reviews*.

[22]   A. K. Furre et al. (2017), 20 Years of Monitoring CO_2-injection at Sleipner. *Energy Procedia* **114**, 3916–3926.

[23]   E. R. Bobicki (2014), Pre-treatment of ultramafic nickel ores for improved Mineral Carbon Sequestration. Ph.D. Thesis, University of Alberta, Canada.

[24]   E. R. Bobicki et al. (2012), Carbon capture and storage using alkaline industrial wastes.*Prog. Energy Combust. Sci.* **38**, 302–320.

[25]   K. Lackner et al. (1995), Carbon dioxide disposal in carbonate minerals. *Energy*, **20**, 1153–1170.

[26]   W. Seifritz (1990), CO_2 disposal by means of silicates. *Nature*, **345**, 486.

[27]   V. Romanov et al. (2015), Mineralization of carbon dioxide: A literature review. *ChemBioEng Rev.*, **2**, 231–256.

[28]   Y. T. Yuen et al. (2016), Carbon dioxide mineralization process design and evaluation: Concepts,case studies, and considerations. *Environ. Sci. Pollut. Res.*, **23**, 22309–22330.

[29]   H. Geerlings et al. (2013), CO_2 mineralization-bridge between storage and utilization of CO_2. *Annu. Rev.Chem. Biomol. Eng.*, **4**, 103–117.

[30]   G. Gadikota et al. (2015), Carbonation of silicate minerals and industrial wastes and their potential use as sustainable construction materials. In *Advances in CO_2 Capture, Sequestration, and Conversion*; American Chemical Society: Washington, DC, USA, 295–322.

[31]   W. J. J. Huijgen et al. (2005), Carbon dioxide sequestration by mineral carbonation, Literature review update 2003-2004. Report No. 2005/11 ECN-C–05-022. Energy research Centre of the Netherlands. Petten, the Netherlands.

[32]   M. D. Aminu et al (2017), A review of developments in carbon dioxide storage. *Appl. Energy.* **208**, 1389–1419.

[33]   J. Li et al. (2018), Integrated mineral carbonation of ultramafic mine. A review. *Minerals.* **8**, 147.

[34]   P. Baláž (2008), Mechanochemistry in nanoscience and minerals engineering. Springer, Verlag Berlin Heidelberg.

[35]   S. Atashin et al. (2015), Investigation of milling energy input on structural variations of processed olivine powders for CO_2 sequestration. *J. Alloys Compd*. **618**, 555–561.

[36]   I. Rigopoulos et al. (2015a), Carbon dioxide storage in olivine basalts: Effect of ball milling process. *Powder Technol*. **273**, 220–229.

[37]   R. A: Kleiv et al. (2006), Mechanical activation of olivine. *Miner. Eng*. **19**,340–347.

[38]   C. A. Summers et al. (2005), Grinding methods to enhance the reactivity of olivine. *Miner. Metall. Process*. **22**, 140–144.

[39]   P. Baláž et al. (2008), Structural changes in olivine $(Mg,Fe)_2SiO_4$ mechanically activated in high-energy mills, *Int. J. Miner. Process*. **88**, 1–6.

[40] T. A. Haug (2010), Dissolution and carbonation of mechanically activated olivine. Norwegian University of Science and Technology.

[41] K. L. Sandvik et al. (2011), Mechanically activated minerals as a sink for CO_2. *Adv. Powder Technol.* **22**, 416–421.

[42] J. Li et al. (2016), Characterization of the microstructure of mechanically-activated olivine using X-ray diffraction pattern analysis. *Miner. Eng.* **86**, 24–33.

[43] M. Fabian et al. (2010), The influence of attrition milling on carbon dioxide sequestration on magnesium–iron silicate. *Miner. Eng.* **23**, 616–620.

[44] R. A. Kleiv et al. (2016), The effect of mechanical activation in the production of olivine surface area. *Miner. Eng.* **89**, 19–23.

[45] NETL. Carbon Dioxide Enhanced Oil Recovery. 30 (2010).

[46] G. E. Brown (1982), Olivines and Silicate Spinels. In: Ribbe PH (ed) Orthosilicates, Vol 5. Reviews in Mineralogy. Mineral Soc Am USA 275: 365.

[47] R. F. Flint et al. (1977), Physical geology: New York, John Wiley and Sons.

[48] https://www.esci.umn.edu/courses/1001/minerals/olivine.shtml

[49] http://www.minerals.net/mineral/serpentine.aspx

[50] M. Mookherjee et al. (2009), Structure and elasticity of serpentine at high-pressure. *Earth Planet. Sci. Lett.* **279**, 11–19.

[51] D. Shelley (1992), Igneous and metamorphic rocks under the microscope, Springer.

[52] M. Cannat (1993), Emplacement of mantle rocks in the seafloor at mid-ocean ridges. *J. Geophys. Res.* **98**, 4163–4172.

[53] D. S. O'Hanley (1991), Fault-Related Phenomena Associated with Hydration and Serpentine Recrystallization during Serpentinization. *Can. Mineral.* **29**, 21–35.

[54] N. G. Holm et al. (2015), Serpentinization and the Formation of H_2 and CH_4 on Celestial Bodies (Planets, Moons, Comets). *Astrobiology* **15**.

[55] M. Mumma et al. (2009), Strong Release of Methane. *Science (80).* **323**, 1041–1045.

[56] D. S. Kelley et al. (2005), A Serpentinite-Hosted Ecosystem: The Lost City Hydrothermal Field. *Science (307).* **5714**, 1428-1434.

[57] M. O. Schrenk et al. (2013), Serpentinization, Carbon, and Deep Life. *Reviews in Mineralogy and Geochemistry*, **75**, 575.

[58] X. B. Wang et al. (2014), Serpentinization, abiogenic organic compound, and deep life. *Sci. China Earth Sci.* **57**, 878-887.

[59] T. M. McCollom et al. (2013), Serpentinites, hydrogen, and life. *Elements* **9**, 129–134.

[60] E. L. Shock (1990), Geochemical constraints on the origin of organic compounds in hydrothermal systems. *Origins Life Evol. Biosphere* **20**, 331–367.

[61] E. L. Shock et al. (1998), Organic synthesis during fluid mixing in hydrothermal systems. *J. Geophys. Res.* **103**, 28513–28527.

[62] J. P. Amend et al. (1998), Energetics of amino acid synthesis in hydrothermal ecosystems. *Science* **281**, 1659–1662.

[63] J. Horita et al. (1999), Abiogenic methane formation and isotopic fractionation under hydrothermal conditions. *Science (80).* **285**, 1055–1057.

[64] T. M. McCollom et al. (2001), A reassessment of the potential for reduction of dissolved CO_2 to hydrocarbons during serpentinization of olivine. *Geochim. Cosmochim. Acta* **65**, 3769–3778.

[65] L. C. Jones et al. (2010), Carbonate control of H_2 and CH_4 production in serpentinization systems at elevated P-Ts . *Geophys. Res. Lett.* **37**.

[66] C. Oze et al. (2012), Differentiating biotic from abiotic methane genesis in hydrothermally active planetary surfaces. *Proc. Natl. Acad. Sci.* **109**, 9750.

[67] A. Neubeck et al. (2011), Formation of H_2 and CH_4 by weathering of olivine at temperatures between 30 and 70°C. *Geochem. Trans.* **12**, 1–10.

[68] D. I. Foustoukos et al. (2004), Hydrocarbons in Hydrothermal Vent Fluids: The Role of Chromium-Bearing Catalysts. *Science (80).* **304**, 1002–1005.

[69] C. Oze et al. (2005), Have olivine, will gas: Serpentinization and the abiogenic production of methane on Mars. *Geophys. Res. Lett.* **32**, 1–4.

[70] G. Proskurowski et al. (2008), Abiogenic hydrocarbon production at Lost City hydrothermal field. *Science,* **319**, 604-607.

[71] T. M. McCollom et al. (2009), Thermodynamic constraints on hydrogen generation during serpentinization of ultramafic rocks. *Geochim. Cosmochim. Acta,* **73**, 856-879.

[72] T. M. McCollom et al. (2010), The influence of carbon source on abiotic organic synthesis and carbon isotope fractionation under hydrothermal conditions. *Geochim. Cosmochim. Acta,* **74**, 2717-2740.

[73] T. M. McCollom (2013), Laboratory simulations of abiotic hydrocarbon formation in Earth's deep subsurface. *Rev. Mineral. Geochem.,* **75**, 467-494.

[74] J. L. Charlou et al. (2002), Geochemistry of high H_2 and CH_4 vent fluid issuing from ultramafic rocks at the Rainbow hydrothermal field (36°14'N, MAR). *Chem. Geol.,* **191**, 345-359.

[75] F. Asinger et al., *Paraffins Chemistry and Technology*, Pergamon, Oxford, 1968

[76] D. Yoshino et al. (1971), Origin of organic matter in early solar system-III. Amino acids: Catalytic synthesis. *Geochim. Cosmochim. Acta* **35**, 927–938.

[77] E. Anders et al. (1974), Interstellar molecules: Origin by catalytic reactions on grain surfaces?, *Astrophys. J.,* **192**, 101-105.

[78] F. Klein et al. (2014), Magnetite in seafloor serpentinite-Some like it hot. *Geology* **42**, 135–138.

[79] P. Baláž et al. (2013), Hallmarks of mechanochemistry: From nanoparticles to technology, *Chem. Soc. Rev.* **42**, 7571–7637.

[80] F. Delogu et al. (2004), Mechanical work and conversion degree in mechanically induced processes, *Mater. Sci. Eng. A.* **382**, 280–287.

[81] S.A. Humphry-Baker et al. (2016), Melt-driven mechanochemical phase transformations in moderately exothermic powder mixtures, *Nat. Mater.* **15**, 1280–1286.

[82] S. Garroni et al. (2017), Mechanically activated metathesis reaction in $NaNH_2$–MgH_2 powder mixtures, *J. Mater. Sci.* **52**, 11891–11899.

[83] G. Mulas et al. (2011), Hydrogenation of carbon monoxide over nanostructured systems: A mechanochemical approach, *Appl. Surf. Sci.*

[84] F. Delogu et al. (2009), Hydrogenation of carbon monoxide under mechanical activation conditions, *Appl. Catal. A.*

[85] R. Eckert et al. (2017), Preferential Carbon Monoxide Oxidation over Copper-Based Catalysts under In Situ Ball Milling, *Angew. Chemie* - Int. Ed. **56**, 2445–2448.

[86] A.M. Kalinkin et al. (2004), Mechanochemical interaction of Ca silicate and aluminosilicate minerals with carbon dioxide, *J. Mater. Sci.* **39**, 5393–5398.

[87] M. Fabian et al. (2010), The influence of attrition milling on carbon dioxide sequestration on magnesium-iron silicate, *Miner. Eng.* **23**, 616–620.

[88] E. Turianicová et al. (2008), A possible way to storage carbon dioxide on mechanically activated olivine $(Mg,Fe)_2SiO_4$, VI Int. Conf. Mechanochemistry Mech. Alloy, 316–319.

[89] I. Rigopoulos et al. (2015), Carbon dioxide storage in olivine basalts: Effect of ball milling process, *Powder Technol.* **273**, 220–229.

[90] J. Li et al. (2016), Carbon dioxide adsorption isotherm study on mine waste for integrated CO_2 capture and sequestration processes, *Powder Technol.* **291**, 408–413.

[91] J. Li et al. (2017), Structural and chemical changes in mine waste mechanically-activated in various milling environments, *Powder Technol.* **308**, 13–19.

[92] J. Li et al. (2017), Ultra-fine grinding and mechanical activation of mine waste rock using a planetary mill for mineral carbonation, *Int. J. Miner. Process.* **158**, 18–26.

[93] J. Li et al. (2015), Ultra-fine grinding and mechanical activation of mine waste rock using a high-speed stirred mill for mineral carbonation, *Int. J. Miner. Metall. Mater.* **22**, 1005–1016.

[94] J. Li et al. (2018), Mechanical activation of magnesium silicates for mineral carbonation, a review, *Miner. Eng.*

Chapter 3: Experimental methods

In this chapter, the experimental techniques and characterization methods used during the PhD thesis will be introduced. All details are reported in the following sub-chapters.

3.1 MECHANICAL MILLING[1]

As introduced in the previous chapters of this thesis, most of the study focuses on chemical processes, related to CO_2 conversion, activated through the application of mechanical energy. It is, this one, the focus of the Mechanochemistry, term introduced by Ostwald in 1891, and which, according to Heinicke definition, "is the branch of chemistry concerned with chemical and physicochemical transformation of substances in all states of aggregation produced by the effect of mechanical energy".

In spite of the fact that the use of mechanical energy to activate chemical transformations dates back to the beginning of human history, (i.e. the activation of combustion processes), however, the born of modern mechanochemistry is generally considered the end of the 19th century with the works of Ostwald and Carey Lea. Since then a wide varied of investigations have been carried out involving basic science and technological application, and a very large number of literature data is now available.

Without going here into the details of the different area of interest of mechanochemistry and mechanical treatment, it is relevant for the present thesis to remember shortly some issues concerning the different terms which are commonly used in literature to denote the processing of powders particles in high-energy ball mills. Mechanical Alloying (MA) is usually used to indicate

the solid-state synthesis by mechanical treatment, from parent elements, of amorphous alloys, nanostructured intermetallic compounds and more in general of metastable systems.

The term Mechanical Milling (MM) is then more general and often used as a synonym of mechanical treatment, but is also employed to address the mechanical treatment of equilibrium crystalline phases, in order to obtain microstructural grain refinement.

Finally, the words Reactive Milling (RM) are usually reserved to indicate mechanical activation of solid phases (metals) under reactive atmosphere: H_2, O_2, N_2, CO, NH_3, to the direct formation of hydrides, oxides, nitrides, carbides. The mechanical alloying process was developed around 1966 by Benjamin and his colleagues at the International Nickel Company, as a result of a long study for the production of a nickel-based superalloy. MA is, generally, a dry high-energy ball milling technique to induce chemical reactions, i.e., mechanochemical reactions at room temperature or at least at much lower temperatures than normally required to produce pure metals, nanocomposites, and a variety of commercially useful materials.[2,3]

The mechanical process starts by mixing powders in the right proportion and by loading the powder mix into the mill along with the grinding medium, that is generally steel balls. This mix is then milled for the desired time until the composition of every powder particle is the same as the proportion of the elements in the starting powder mix.

Different types of equipment are used to carry out the mechanochemical activation processes, which differ in their capacity, efficiency of milling, geometry, milling dynamics, vial and milling bodies materials, etc.

Two main types of ball mills are generally used at laboratory level: shaker or vibration mills, and planetary mills. In the vibrating mills, the reaction vial (or

mechanochemical reactor) is rapidly oscillated from side to side, so that causing the milling bodies (usually spheres) to shear and grind the reagents together. In planetary mills, the reaction vessels are spun at high speed, counter-rotatory to the main spinning "sun wheel": this originates the term planetary. As a result, the balls can grind the solids within the vial walls.

In the present work, the mechanochemical treatment processes were carried out using either shaker-type either planetary mills and in the following a short description of the two types is presented.

Among the vibrating mills, the SPEX mod 8000 Mixer/Mill is widely used for laboratory investigations and has one vial which allows to process up to 10-20 grams of materials at a time, depending on chemical characteristics and density. The vial, filled with the powdered sample and grinding balls, is secured in the clamp and energetically rotates back and forth. This motion is combined with lateral movements of the ends of the vial so that it appears to be describing an 8-like figure as it moves. At each rotation, the balls impact against the sample powders milling and mixing it.

Such SPEX mills can be considered as a high-energy variety because the ball velocities and consequently the force impact is high, due to the amplitude and speed of rotation. A variety of vial materials is available for these mills, including hardened steel, alumina, tungsten carbide, zirconia, stainless steel, silicon nitride, agate, plastic, and methacrylate.

Another milling equipment widely used for MA is the planetary ball mill. Several planetary mills are nowadays commercially available including Fritsch Pulverisette, as well as Retch etc. These are characterised by larger vials which allow to mechanically treat up to a few hundred grams of powders at a time. Its vial is secured on a rotating support disk and a special mechanism forced it to rotate around its axis, according to a planet-like movement. The centrifugal

force produced by the rotation, act on the grinding balls contained in the vial, that run causing the grinding of the sample. The rotation speed can be controlled in the modern version of the miller. Also for planetary mill are available grinding vials and balls in different materials: agate, silicon nitride, sintered corundum, zirconia, chrome steel, Cr-Ni steel, tungsten carbide, and plastic polyamide. Even though the linear velocity of the balls in this type of mill is higher than that in the SPEX mills, the frequency of impacts is much higher in the SPEX mills. So, in comparison, Fritsch Pulverisette can be considered lower energy mills. In Figure 3.1 are shown the milling equipment used in this work: a) Spex mixer mill 8000 (University of Sassari); b) Fritsch Pulverisette 6 (CNEA, San Carlos de Bariloche).
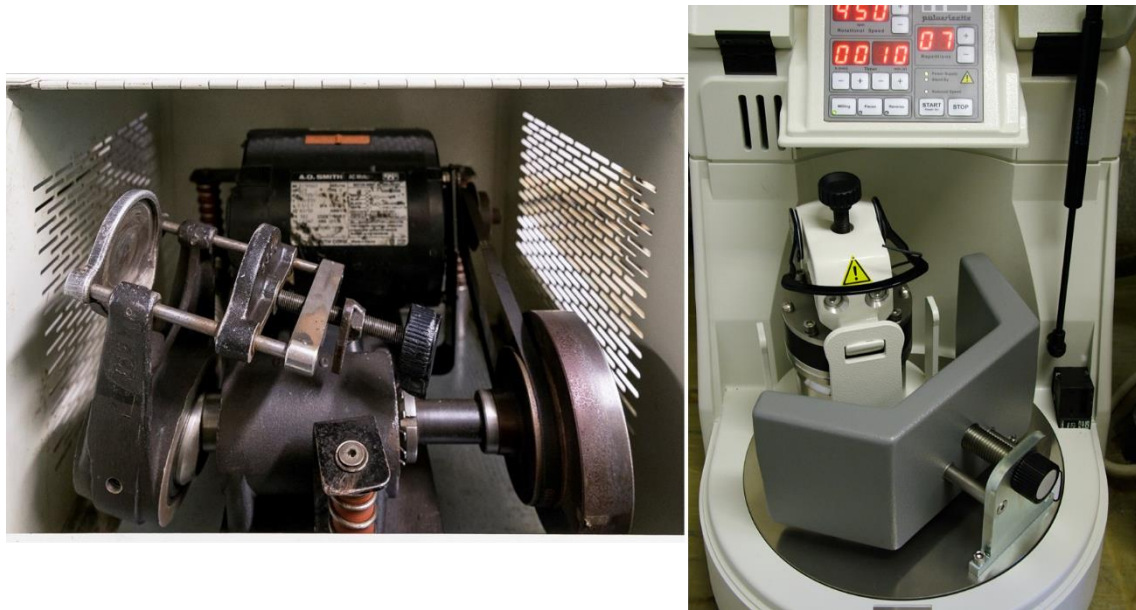

Figure 3.1: a) Spex Mixer mill mod.8000; b) Fritsch Pulverisette 6 mill.

3.2 X-RAY DIFFRACTION

The knowledge of the crystal structure is a fundamental requirement in many disciplines besides chemistry. The discovery of X-rays by Roentgen in 1896 allowed to derive systematically the crystal structure knowledge even in complex systems. Only after 15 years the crystallographers could formulate and propose to the community an adequate theory ables to explain the observed diffraction experiments, enabling to retrieve the mutual arrangement in the 3-D space[4]. This successful theory allowed to relate the location of atomic species or molecules in 3-D *real* space, starting from the relative diffracted intensities collected in the Ewald sphere, to the *reciprocal* 3-D space (Figure 3.2).

The main result of crystallography is often enunciated with the 14 Bravais lattices, reported in Figure 3.3.
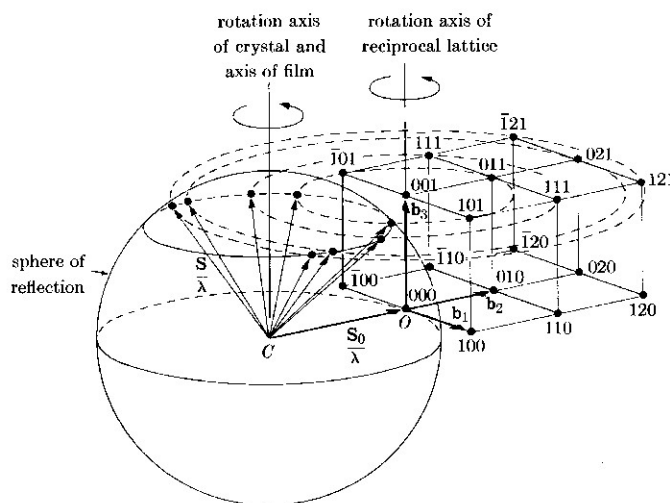

Figure 3.2: Edwald sphere.

Through the Bravais lattices, the matter can be considered in abstract form with a periodical arrangement of atoms or molecules located in correspondence of the *lattice point*. These allow defining the origin anywhere in the crystal and to describe the geometric and symmetric properties of the crystal arrangement (7

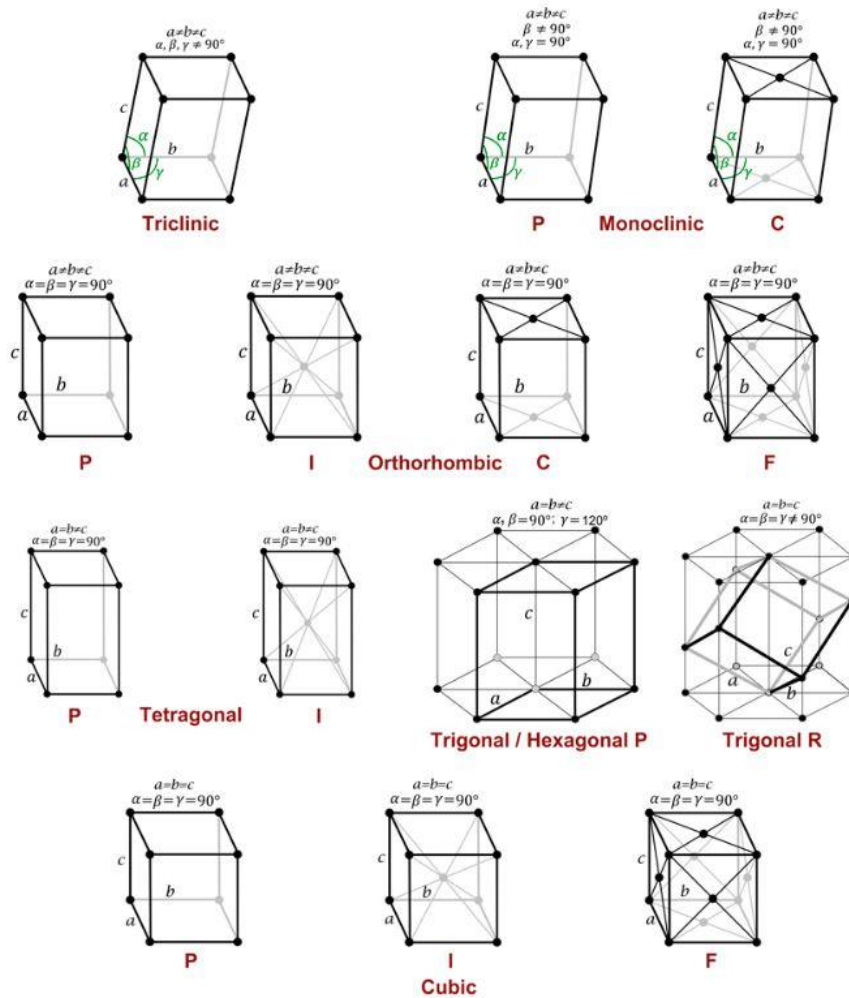geometric systems arranged according to 14 fundamental lattices due to Bravais).

Figure 3.3: the Bravais lattices

The definition of the smallest basic unit, *unit cell*, which must keep all the chemical and physical properties observed macroscopically, is necessary to describe the periodical arrangement in three dimensions of a crystal.

For example, the number of atoms in the unit cell volume must be compatible with the whole density determined by Archimedean methods.

Such lattices can be further finely classified by the symmetric properties, grouping the crystals according to the combinations of symmetry operations (32

point groups) that they may possess. The point group classification comes from the set of operations leaving at least one point unchanged in the course of the transformation, involved to bring the system onto itself.

Such operations are combinations of the rotation around selected axes, the mirroring across a selected plane, the inversion operation concerning a selected point, the combination of rotation and inversion operations, the combination of mirroring with inversion.

So, the number of total possibilities to account properly the translational periodicity in infinite crystals rises to 230 space groups. This classification scheme is finite and represents a key to describe the dependence of macroscopic properties after determination of structural properties.

Thus, for the 7 classified geometries according to the lattice parameters of the unit cell and to the symmetry operations compatible with periodicity, the number of sites available to arrange atomic species inside the unit cell is determined by the observed density of crystal and, more important, by the site fractional coordinates determined in agreement with the possibilities of transformations onto the original crystal.

This information is collected into CIF files (Crystallographic Information Files), that consists in a standard list reporting the space group adopted by the crystal, containing geometry, lattice parameters of the unit cell, type of atomic species occupying sites expressed by spatial fractional coordinates, together with multiplicity generated after carrying out the possible transformations. Each space group may have analogous correspondence in the reciprocal space, corresponding to nodes on the Ewald sphere. Its surface is made available to locate the intensities of rays diffracted in any direction away from the direction of the incident beam. The specific directions of diffracted X-rays, for which

enforcement of scattering amplitudes are observed, may be determined with the geometric conditions of the so-called Bragg law (Eq. 3.1):

$$\lambda = 2d \ sin\vartheta \qquad\qquad Eq. \ 3.1$$

The International tables have developed for each space group, the general features available in the real space, but also the corresponding characteristics in the reciprocal space, such as general and special reflection conditions, the symmetry of special projections, asymmetric unit, and symmetry operations. This makes possible, at least in principle, to solve the structure not only of single crystals but also of polycrystalline materials and of systems in powder form, provided that their diffraction pattern refers to a single-phase condition.

X-ray diffraction analyses allow, of course, to recover much more information than the qualitative phases composition of the investigated systems: they are a powerful tool to get quantitative data relevant to phases abundance, microstructural features, etc.: to this regard, it is necessary to correctly relate the observed intensity with the electron density, responsible for the X-ray scattering process. Two major cases can be encountered for solid mixtures: i) all the component phases are crystalline; ii) an amorphous component is present in addition to the crystalline substances in the powder. Both possibilities can be successfully implemented in a laboratory according to two methods: the Quantitative Phase Analysis (QPA) and the Rietveld method[5]. In QPA, the experimental relative intensities can be better normalized for quantitative purposes with the use of an internal standard. Of course, this procedure may become difficult when many samples should be examined. Besides, this procedure may have limited success in case of partial overlapping of peak profiles from different phases, due to the difficulty in separating the contribution of one phase from the other.

Using the Rietveld approach, these uncertainties can be removed in most cases, because it is a refinement method for structure solution extended to multi-phase samples and proposed in an organized manner since the '80.

Among the different available applicative codes, in the experimental activity of the present work, we resorted to using the MAUD software (constantly under development by L. Lutterotti), which offers several appreciable specific features including the easy and friendly access to the structural parameters, that must be kept under control to fit the experimental diffraction data with a hypothesized electron density distribution within the unit cell.

Several advantages derived by the use of the Rietveld approach addressed with MAUD:

1) Diffraction data of various formatting can be flexibly inspected according to various weighting schemes to check the quality of the experiment.

2) Once determined separately from a standard sample free from crystal size and defect broadening, the instrument is made to convolve the model pattern proposed to fit the experimental data.

3) Loading the CIF files from various archives is straightforward, if the CIF files may respect exactly the storage protocols.

4) The program offers easy procedures to model the background polynomial and the commonly encountered numerical behaviour.

5) It can be used for demo and teaching purposes.

6) The equations for peak broadening are developed explicitly as a function of the average crystallite size $<D>$ and lattice disorder content $[<\varepsilon>^2]^{1/2}$ enabling the user to evaluate the results in comparison with his expectations.

7) The number of structure parameter set as adjustable in the course of the minimization turns out easy to check and to modify.

8) Several implemented routines at different level of complexity can be incorporated using alternative models: anisotropic broadening, anisotropic temperature factors, stacking fault occurrence, texture etc..

9) "Ab-initio" inspection of alternative structure solutions may be explored for systematic absences.

Every X-ray diffraction (XRD) analysis of this work has been collected by using a SMARTLAB diffractometer (Figure 3.4, CeSAR of University of Sassari) with a Copper rotating anode, working at a power of 40 kV and 100 mA. The diffractometer is also equipped with a graphite monochromator in the diffracted beam and a detector based on a scintillation tube. Quantitative analysis of the crystalline phases, structure and microstructure parameter determinations were performed with the previously described MAUD program (Materials Analysis Using Diffraction).

Figure 3.4: SMARTLAB diffractometer.

3.3 INFRARED SPECTROSCOPY

An infrared spectrum represents a fingerprint of a sample. Infrared radiation (IR) generally refers to that part of the electromagnetic spectrum between the visible region and the microwaves. The portion of the most practical interest is the region between 4000 and 400 cm^{-1}. The absorption peaks correspond to the frequencies of vibrations between the bonds of the atoms of the material. The IR spectra consist of a set of peaks, whose amplitude is related to a certain amount of rotational energy, associated with the variation of vibrational energy. The frequency or wavelength of absorption depends on the relative masses of the atoms, by the force constant of the bonds and the geometry of atoms. The position of the bands in the IR spectrum are often indicated by wavenumber values (cm^{-1}). The peaks intensity can be expressed as transmittance (T) or as absorbance (A). Transmittance is the ratio between the incident power radiation and the power radiation transmitted by the sample. The absorbance is expressed by the following relation:

$$A = log_{10}\ (1/T)$$
<div align="right">*Eq. 3.2*</div>

There are two types of molecular vibrations: *stretching* and *bending*. A *stretching* vibration is a rhythmic movement along the binding axis resulting in an increase or decrease in the interatomic distance. A *bending* vibration is due to a variation in the bonding angle. Figure 3.5 illustrates these concepts[6].
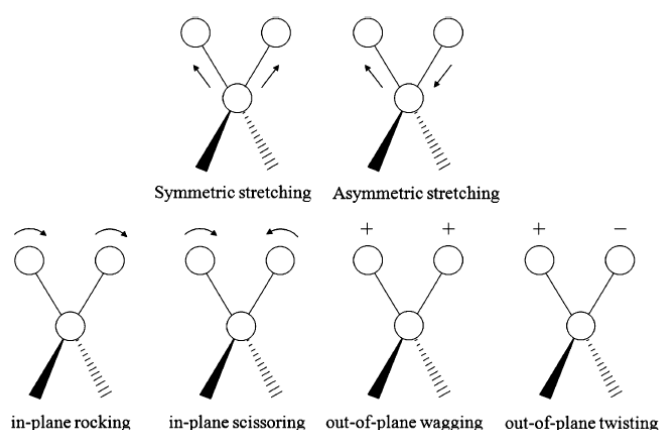
Figure 3.5: Schematic representation of the different molecular vibration modes

Only the vibrations that lead to a variation of the dipole moment, in the molecule, can be observed. This restriction is called the *selection rule*. Stretching frequency calculations can be approximated by applying Hooke's law. According to this model, two atoms and the related bond are considered as a simple harmonic oscillator. The following equation, derived from the Hooke's law, connect the oscillation frequency, the atomic masses and the strength constant of the bond:

$$\bar{v} = \frac{1}{2\pi c} \sqrt{\frac{f}{(M_x M_y)/(M_x + M_y)}} \qquad Eq.\ 3.3$$

Where $\bar{v}$ is the vibration frequency (cm^{-1}), c is the speed of light (cm/s), f is the strength constant of the bond (dine/cm), M_x and M_y are the masses of the atom x and y, respectively.

The Fourier Transform IR spectroscopy (FT-IR) is the most widely used technique; it is achieved using an interferometer, which allows the simultaneous scan of all the frequencies present in IR radiation sources. The scanning is due to a moving mirror that produces an optical path difference, which results in constructive or destructive interference with the reflected beam by a fixed mirror (Figure 3.6).
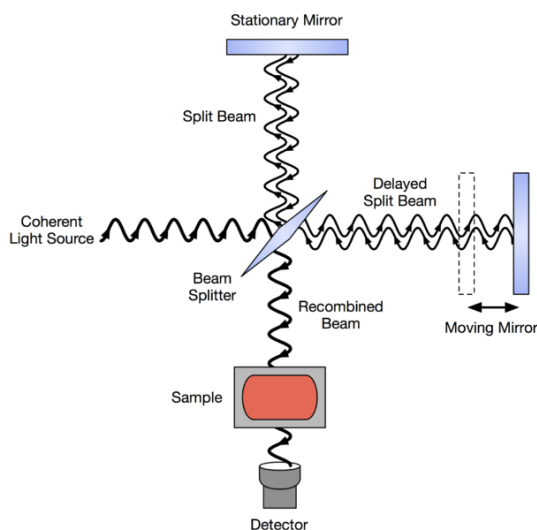

Figure 3.6: FT-IR interferometer.

This technique allows collecting an interferogram that shows the representation of the intensity in the domain of time. Applying the Fourier Transform, the infrared spectrum obtained is the representation of the intensity in the frequency domain. Figure 3.7 shows the Perkin Elmer FT-IR Spectrometer, used to analyse the composition of the gas phase of the tests carried out in Argentina (CNEA, San Carlos de Bariloche).

Figure 3.7: Perkin Elmer FT-IR Spectrometer.

3.4   RAMAN SPECTROSCOPY[7]

Raman spectroscopy is a technique based on inelastic scattering, applied to detect vibration in molecules, that provides information about chemical structures and physical forms, to identify substances from a characteristic spectrum, called fingerprint, as for IR spectroscopy mentioned above. It allows to analyse solid, liquid or vapour samples but is less used than IR absorption

because of the problem of sample fluorescence. However, recent advances in instrument technology have simplified the equipment and reduced the problems substantially.

The inelastic scattering of light was observed experimentally for the first time in 1982 by Raman and Krishnan. When light interacts with matter, photons may be absorbed or scattered, or may not interact with the material and pass straight through it. It is also possible that the photon interacts with the molecule and scatters from it. The scattered photons can be observed by collecting light at a certain angle to the direction of the incident light beam.

The differences between Infrared and Raman spectroscopies are shortly depicted in the following. In infrared spectroscopy, a range of frequencies in the infrared range is directed onto the sample. Absorption occurs where the frequency of the incident radiation corresponds to the energy gap between two vibrational states of the molecule so that it is promoted to a vibrational excited state. The loss of this frequency of radiation from the beam after it passes through the sample is then detected. In contrast, Raman spectroscopy uses a single frequency of radiation to irradiate the sample and the radiation detected is the one scattered by the molecule, one vibrational unit of energy different from the incident beam. Thus, in Raman scattering, the light interacts with the molecule and polarizes the cloud of electrons around the nuclei to form an unstable state from which the photon is quickly re-radiated.

If the scattering involves only electron cloud distortion, the photons will be scattered with very small frequency changes. This process is called elastic scattering (Rayleigh scattering for molecules) and is the dominant process. However, if the scattering induced the nuclear motion, energy will be transferred either from the incident photon to the molecule or from the molecule to the scattered photon. In these cases the process is inelastic and the

energy of the scattered photon is different from that of the incident photon by one vibrational unit. This is Raman scattering. Intense Raman scattering occurs from vibrations which cause a change in the polarizability of the electron cloud around the molecule. Usually, symmetric vibrations cause the largest changes and give the greatest scattering.

Raman spectroscopy is a powerful tool for the examination of inorganic materials or those containing inorganic components. It allows to positively identify and characterize both elements and molecules.

Modern Raman spectrometers are constituted by a microscope, which is an integral part of it. This configuration has many advantages, including the possibility to examine small samples and to detect a very small amount of material, despite the scattering is weak. Further, it can discriminate against fluorescence from a sample matrix since only the chosen microscopic feature in the sample is irradiated at high power, particularly when the microscope is set up confocally.

Figure 3.8 shows the LabRAM ARAMIS apparatus, used to carry out Raman analysis at the ICGM, Montpellier (France).

Figure 3.8: Raman microscope spectrometer apparatus.

3.5 MÖSSBAUER SPECTROSCOPY[8]

The Mössbauer spectroscopy is a nuclear gamma resonance (NGR) spectroscopy, a relatively sophisticated and sensitive technique that provides detailed information about the physicochemical state of atoms of selected elements.

In 1957, Rudolf Ludwig Mössbauer discovered the recoil-free nuclear gamma resonance, better known as Mössbauer effect (ME).

During the first few years after this discovery, research on the ME was mainly focused on understanding the physics behind it. At the same time, this phenomenon was used as the basis to develop an autonomous spectroscopic method, called Mössbauer spectroscopy. This technique provides valuable information on oxidation states, magnetic hyperfine fields, coordination symmetry, and lattice vibrations through the extremely high accuracy in the analysis of the nuclear energy levels.

The application of this spectroscopy concern many fields: chemistry, metallurgy, geology, etc. Most remarkable is surely the recent study of the soil on Mars surface which provided also the final proof of the presence of liquid water in the planet[9,10]. However, the application of Mössbauer spectroscopy is relatively limited because only iron, tin, antimony, iridium, ruthenium and gold are suitable for this study. The extensive application is mainly for iron and tin, while the other elements mentioned above are used sporadically. This is mainly due to the low energies of the nuclear transitions for both ^{57}Fe and ^{119}Sn (and to some extent ^{121}Sb), which allow measurements at ambient temperature, and to the relatively long half-life of the respective ^{57}Co and ^{119m}Sn parent nuclides feeding the nuclear transitions, which allows the use as sources for many months. Some advantages of the use of Mössbauer spectroscopy are the possibility of applications to in-situ measurements and its relatively lower cost,

compared with techniques such as photoelectron spectroscopy or electron microscopy, for instance.

The ME is the recoil-free resonance absorption of γ-quanta emitted when a radioactive nuclide decays to a stable daughter nucleus in a crystal.

A radioactive isotope usually decays to the stable ground state of a daughter nuclide by passing through different excited states. This transitions between different electronic states occur by the emission of electromagnetic radiation: photons, which are usually called γ-quanta. Such photons may be reabsorbed by a nucleus of the same isotope by a process called *resonance absorption* because its energy is just right for the excitation of the energy level in the absorbing nucleus (Figure 3.9).
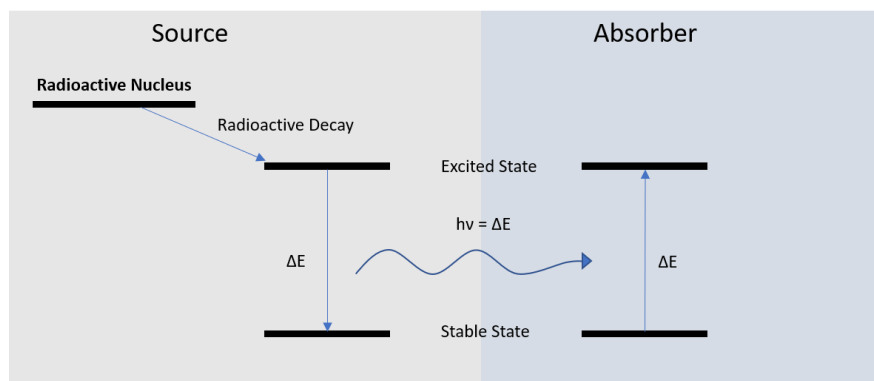

Figure 3.9: scheme of nuclear resonance transition between the exited and ground states in two nuclei of the same isotope.

However, this resonance adsorption phenomenon was very difficult to observe. Because of the momentum carried by the emitted or absorbed photons, the nuclei are usually undergoing a recoil during the emission or the adsorption of γ-quanta. The energy of the emitted photon is slightly lower than the energy required for resonance absorption. So the energy emitted during the recoil is high enough to preclude resonance absorption. For example, in the common case of ^{57}Fe, the natural linewidth C of the emission and absorption line is about $5 \cdot 10^{-9}$ eV, whereas the high energy of the 14.4 keV nuclear transition gives rise to

a recoil energy of about $2 \cdot 10^{-3}$ eV, which is about six orders of magnitude higher than the natural width of the emission and adsorption line. It follows directly that the separation between the adsorption and the emission energies is far too large to allow the resonant adsorption of γ-quanta by free nuclei. When embedded in a solid lattice, however, an atom cannot recoil as if it were free, therefore, there is a finite probability that emission and absorption processes take place without recoil.

In Mössbauer spectroscopy, a small quantity of a radioactive nuclide is used as a source: during its decay, it passes through the excited state of the daughter isotope to be studied, producing an intense beam of highly monochromatic recoil-free γ-photons. In the case of [57]Fe Mössbauer spectroscopy, the [57]Fe excited state is populated by the electron captured by decay of the radioactive isotope [57]Co (Figure 3.10). The latter has a half-life of 270 days and is commonly produced by bombarding [56]Fe nuclei with 9.5MeV deuterons in a cyclotron following the reaction [56]Fe(d,n)[57]Co. Owing to its relatively long half-life, a [57]Co Mössbauer source can often be used for several years.
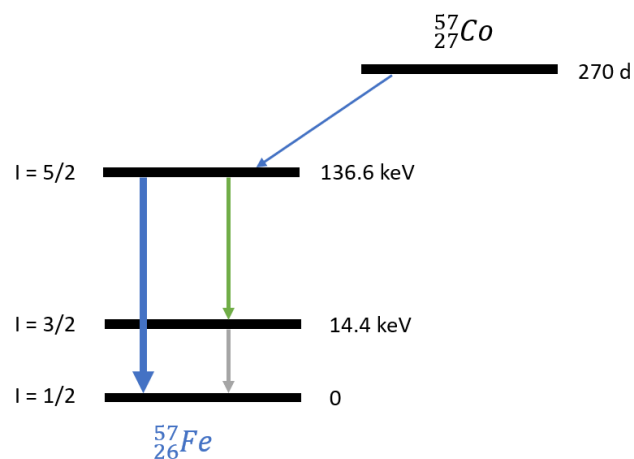

Figure 3.10: nuclear transition and energy level of [57]Fe.

The high-energy resolution of Mössbauer spectroscopy allows the detection of the interactions between the nuclei and the electrons in a solid, and hence to obtain information on the chemical environment of the nuclei. These interactions, called hyperfine interactions, are:

a) the electric monopole interaction, which causes a shift of the resonance lines called isomer shift. Basically, it corresponds to the energy difference between the source and absorber nuclei, resulting from effects including differences in valence state, spin state and coordination of adsorber atoms.

b) the magnetic dipole interaction, between the dipole moment of the nucleus and a hyperfine magnetic field which causes a splitting of the nuclear energy levels, called magnetic hyperfine splitting;

c) the electric quadrupole interaction, due to the splitting of the energy levels caused by the interaction between the nuclear quadrupolar moment and an electric field gradient at the nucleus, which causes the so-called electric quadrupole splitting.

The interpretation of a Mössbauer spectrum involves several steps, from the preparation of the data to the least-squares fit of the resonance lines. From a Mössbauer analysis, two mirror-symmetrical spectra are obtained. These spectra are commonly folded and added one to another around a folding point F in order to obtain the final Mössbauer spectrum. The folding point F is usually assigned to the point when the source is moving away from the absorber with its maximum velocity. The absorption spectrum is generally represented by a superposition of several spectral lines, which can be combined in multiplets (doublets, sextets, etc.). These multiplets are characterized by the parameters typical of the hyperfine interactions, previously mentioned: the isomer shift (d), the quadrupole splitting (D), and the magnetic field (B). Each spectral line is characterized by an experimental width at half-height (Гexp),

and, in the approximation of thin absorbers, has a Lorentzian shape. Finally, the total and relative intensities of the resonance lines are also important for identifying specific multiplet shapes or for estimating the relative concentration of coexisting phases producing different subspectra. These parameters are obtained by performing the best fit of the experimental data, optimizing appropriate combinations of Lorentzian lines by least-squares fit routines based on specific mathematical methods. These optimizations are commonly performed by computer programs devoted to the treatment of Mössbauer spectra.

The Mössbauer isotope of iron, ^{57}Fe, has a natural isotopic abundance of 2.19%. The stable ground state has nuclear spin 1/2, whereas the 14.4 keV excited state has nuclear spin 3/2 and a lifetime of 140 ns, which corresponds to a linewidth of 0.097mms^{-1}. In a Mössbauer spectrum, therefore, the measured linewidth cannot be smaller than twice this value, that is, 0.19mms^{-1}. The measurement of spectra at different temperatures often allows providing additional information by revealing the presence of temperature-dependent effects, such as paramagnetic relaxation or changes in the magnetic properties.
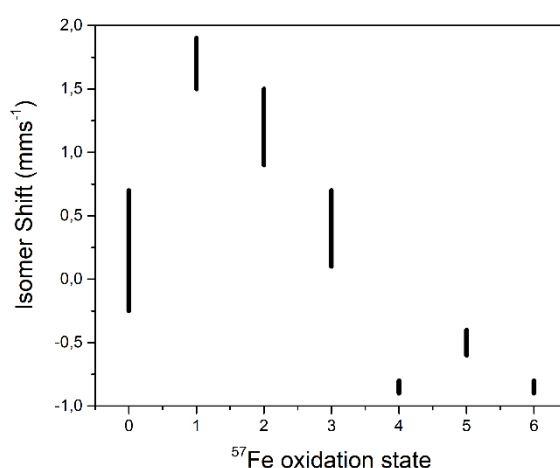

Figure 3.11: ^{57}Fe isomer shifts for ionic compounds.

3.6 SCANNING ELECTRON MICROSCOPY

The Scanning Electron Microscopy (SEM) allows to study and characterize heterogeneous organic and/or inorganic materials, from micrometric to nanometric scale. This technique can provide different information about the sample:

1. Topography: surface characteristic of the sample, like shape, dimension, etc.;

2. Composition: element present and their percentage;

3. Crystallographic: atoms disposition in the crystals.

This set of information allows a relevant surface characterization of the sample under investigation, the identification of its microstructure and, therefore, of the derived macroscopic properties.

SEM can be considered as consisting of two main parts, the column where electronic optics and detectors are contained, and the console that includes the Control Panel, the display and the calculator. A scheme of SEM structure can be found in Figure 3.12(a). The electron beam can be generated by thermionic emission of a filament of tungsten or lanthanum hexaboride, or by field emission. The produced electrons are then accelerated by the electric field between the cathode (filament) and the anode, which may be found at a potential difference that usually varies between 500V and 30kV, reaching energies between 500eV and 30keV. The beam is then focused on objective lenses that are generally electromagnetic. Together with the objective lenses, the scanning coils are also integrated, which allow directing the beam towards the sample. A pair of lenses deviate the beam of an angle θ relative to the vertical direction, while another is deflected by an angle 2θ in the opposite direction. Once the interaction between the electron beam and the sample has occurred,

can be obtained different information about, through various types of detectors. Several detectors are usually available on the apparatuses, and, accordingly, different operational modes are usually considered. Among these the most common are: the use of *secondary* electron, *backscattered* electron and *X-rays microanalysis*. The secondary electrons (SE) are generated by inelastic scattering, expelled from an orbit around the nucleus, after the ionization of the atoms by the incident beam. They are characterized by lower energy, from 0 to 50 eV, so they come from a region very close to the sample surface (5-10 nm). Therefore, secondary electrons provide only morphological information.

The backscattered electrons (BSE) are generated by elastic diffusion. They have higher energy with respect to the SE, which is similar to that of the electron beam (~50eV) and come from depths greater than 1 to 2 μm, so they provide information related to the layers immediately below the surface. The backscattering electron rate used increases with the increase of the atomic number. The main advantage of using BSE electrons is due to their sensitivity towards the atomic number.

The microanalysis is a spectroscopic technique, often also named as EDAX (Energy Dispersive X-ray Analysis): this technique, often integrated into the SEM apparatus, allows determining the elements present in the sample and quantify them also in traces.

Surface morphology of the samples powders was investigated by scanning electron microscopy using a FEI Q250 microscope (CeSAR of University of Sassari), reported in Figure 3.12(b).
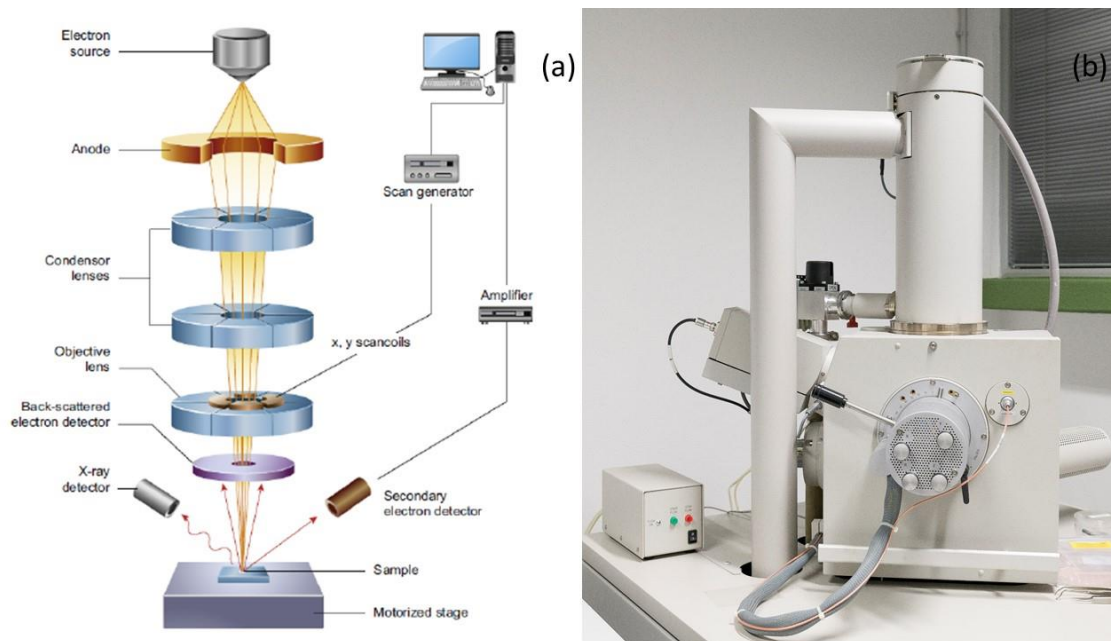
Figure 3.12: (a) scheme of optical components in a basic SEM; (b) SEM apparatus.

3.7   PHYSISORPTION PHENOMENON ANALYSIS AND B.E.T. METHOD

Gas adsorption analysis commonly used to evaluate the surface area and porosity of solid materials. Consists of exposing solid samples to gases or vapours at different experimental conditions and evaluating either the weight or the sample volume uptake. Analysis of these data provides physical information, characteristics of the solid sample, like porosity, total pore volume and pore size distribution. The BET technique is the most common method for determining the surface area of powders and porous materials. It takes the name from Stephen Brunauer, Paul Hugh Emmett and Edward Teller, that in 1938 originating the theory behind the multi-molecular adsorption process[11]. They extended the concept of Langmuir, allowing measurements of adsorption

phenomenon to be correlated to physical relevant properties of a material such as total surface area, pore-size distribution, micro-pore analysis and porosity.

Nitrogen gas is generally employed as the probe molecule and exposed to the solid under investigation at liquid nitrogen temperatures, 77 K. At this temperature a specific number of gas nitrogen molecules are attracted to the surface of a solid by Van der Waals forces. This process is known as *physisorption* and is characterized by low interaction energy, which distinguishes it from *chemisorption*. Physisorption is a thermodynamically reversible phenomenon, while chemisorption is not. The number of physisorbed molecules on the sample surface depends on the N_2 relative pressure, that is the ratio between the partial vapour pressure of adsorbate gas (P) and the saturation pressure of adsorbate gas (P_0), i.e. the pressure at which the unconfined gas condenses. Sometimes, Kr is used instead of nitrogen for low specific surface area measurement, because it is more suitable. The cross-sectional area of Kr and N_2 are 0.202 nm^2 and 0.162 nm^2 respectively. Kr molecules are larger by about 25%, so assuming both molecular sizes equal and adsorption pressure equal to 50 Pa, the pressure change measured for N_2 is equal to 0.16% (=50/30450), while for Kr is 38% (=50/130) at the same relative pressure (P/Po=0.3, N_2=30400Pa, Kr = 80Pa).

The surface area of the solid is evaluated from the measured monolayer capacity and knowledge of the cross-sectional area of the molecule being used as a probe (Figure 3.13). A typical adsorption isotherm is shown in Figure 3.14(a)[12]. The hysteresis between adsorption (lower) and desorption (upper) curves, indicate the existence of mesopores (pores in the range of 2-50 nm) and provides information on the connectivity of the porous network. The initial part of the isotherm is used to calculate the surface area since it depends by monolayer coverage of N_2 on the surface. In contrast, the total pore volume is

evaluated by the maximum amount of condensed N_2, so is calculated from the upper part of the isotherm. BET analysis allows characterizing materials with pores of dimension between 2 and 150 nm.

Pore size distribution analysis is performed by capillary condensation experiments, such as N_2 adsorption and the application of various forms of the Kelvin equation which relates the average pore size filled at a particular relative pressure.
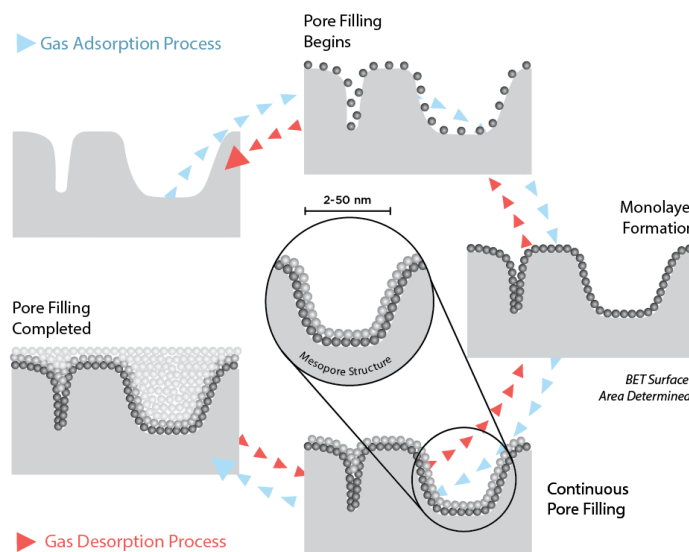

Figure 3.13: description of the adsorption/desorption process.

Figure 3.14(b) displays a well-defined pore size distribution from a modified Kelvin analysis, using a BJH thickness curve.
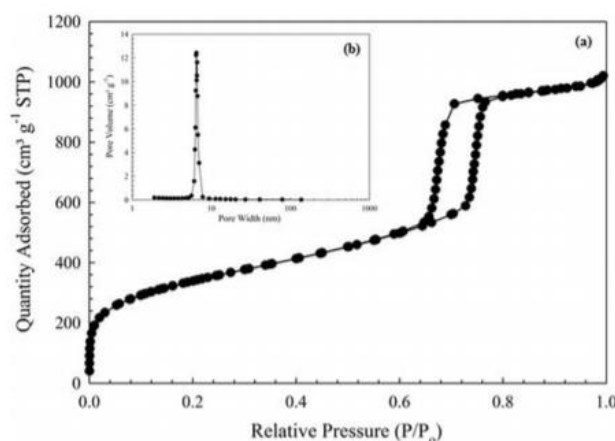

Figure 3.14: (a) typical adsorption/desorption isotherm for a mesoporous material; (b) pore size distribution.

The preparation of the sample, before the adsorption analysis, is a key aspect of material characterization. To perform a relevant analysis, it is necessary to remove from the surface of the sample, gases and vapours which could have adsorbed from the ambient air. Otherwise, the surface area measurement can be non-reproducible. The preparation run consists of heating a sample under conditions of dynamic vacuum or purging with inert gas. High-temperature activation, therefore, can either increase or decrease the porosity.

Figure 3.15 shows the Fisons Sorptomatic 1990 apparatus, used to evaluate the surface area of the prepared samples.

Figure 3.15: BET analysis apparatus.

3.8   THERMOGRAVIMETRIC ANALYSIS

The thermogravimetric analysis is an experimental method to characterize element, compound or mixture by measuring changes in physicochemical

properties as a function of increasing temperature up to elevated temperatures[13]. This technique provides several information relating to physical phenomena, for example, vaporisation, sublimation, absorption, adsorption and desorption; or chemical phenomena like decomposition, desolvation, solid-state reaction and oxidative degradation. Thermogravimetry cannot provide information about fusion, crystalline transition or those solid-state reactions that occur without a weight change.

The basic instrument requires a precise balance and a furnace programmed for a linear temperature rise with time. The data of a thermogravimetric experiment is often presented by weight versus temperature (or time). The weight axis should be scaled as a percentage of the total weight. Figure 3.16(a) reported an example of a thermogravimetric experiment: A(1), A(2) and A(3) are plateaux, indicative of constant weight, in the decomposition curve, B is a point of inflexion where the value of the derivative is a minimum (but not zero) and may involve the formation of an intermediate phase.
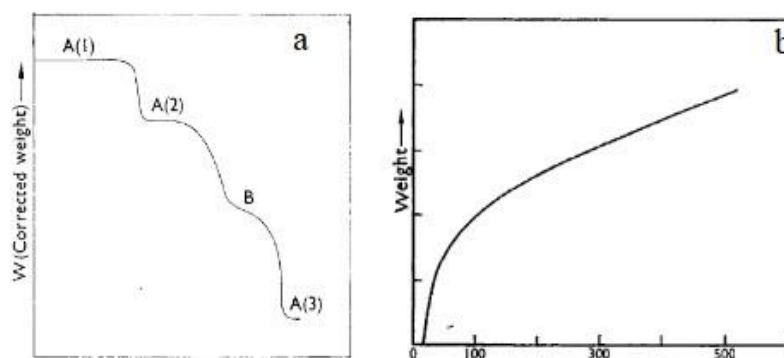

Figure 3.16: (a) Thermogravimetric curve and (b) typical correction curve [86].

Figure 3.16 (b) shows an apparent change in weight with increasing temperature for an empty crucible. As we might expect, by heating an empty crucible we should not notice a weight gain. However, this phenomenon is very common and can be observed even with a full crucible, during a measurement.

This apparent weight change is caused by a complex combination of several factors such as air buoyancy, convection effects within the furnace, crucible geometry, the atmosphere in the furnace and many others so it is necessary to use the correction curve to arrive at the actual weight change occurring in the sample. The thermogravimetric analyses were carried out by a Setaram Labsys DTA-TGA, shown in Figure 3.17.

Figure 3.17: TGA apparatus.

3.9 GAS CHROMATOGRAPHIC ANALYSIS[14]

The official definition of the IUPAC (International Union of Pure and Applied Chemistry) of chromatographic technique is: "*Chromatography is a physical method of separation in which the components to be separated are distributed between two phases, one of which is stationary (stationary phase) while the other (the mobile phase) moves in a definite direction*". The term chromatography was coined by Tswett in 1906, who scientifically described the process for the first time. The word *chromatography* derived from the Greek words *chroma*, colour, and *graphien*, to write. The first applications of this technique, indeed, included

column and paper chromatography. Although different chromatographic methods developed, they have several factors in common: samples are dissolved in the mobile phase, which travels through the stationary phase and separation is possible because different compounds have different affinities for the mobile and stationary phases. This affects the distribution between the two phases and the behaviour of the sample in the system.

Gas chromatography is a specific type of chromatography in which the mobile phase is an inert gas and the stationary phase a solid.

The components of a gas chromatograph (GC) are shown in Figure 3.18.

The sample is injected into the GC via the inlet valve (or injector); the mobile phase, carrier gas, passes through the inlet and drag the sample onto the column, where the stationary phase is. The column is enclosed in a temperature-controlled oven. The chromatographic separation takes place when the mixture goes through the column: once separated, the components of the sample exit from the column and reach the detector, which provides an electronic signal proportional to the concentration of the eluting analytes.
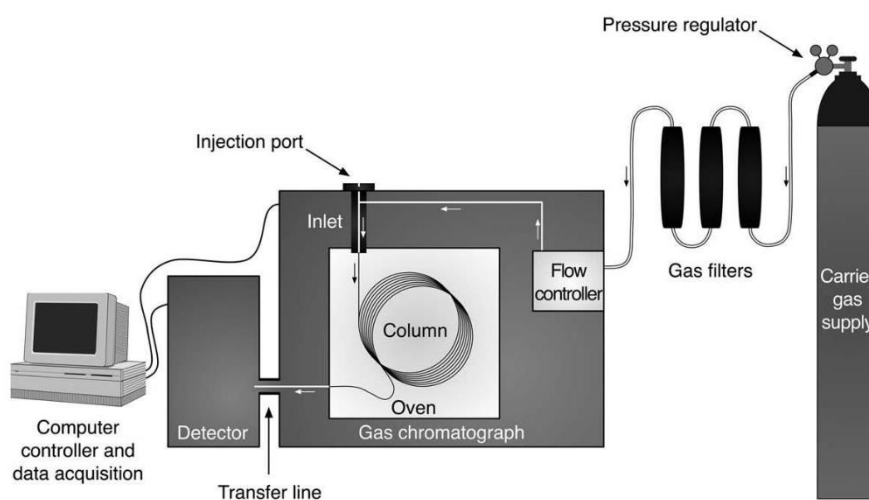

Figure 3.18: generic setup of a gas chromatograph.

As previously mentioned, the mobile phase is the carrier gas, that does not interact with the analytes. The choice of the carrier is related to the type of detector used, on its efficiency and availability and also on how it performs under specific experimental conditions. The most commonly used gases for gas chromatography are helium, hydrogen and nitrogen. For example, using a flame ionization detector, helium and nitrogen are suitable, whereas hydrogen is not. Water and oxygen are some of the most common and damaging contaminants; their presence in a carrier gas can degrade expensive chromatographic columns, in addition to causing high background and spurious peaks.

In order to guarantee a good injection, the sample should be introduced instantaneously as a *plug* onto the column. There are several different types of inlets for GC systems, each with its own purpose. The injection port consists of a septum, used to seal the inlet and maintain the carrier gas head pressure, which is necessary to establish the flow through the column. Generally, septa are made of heat-resistant polymeric silicone, with self-sealing capacity following injection by a syringe. They have a limited lifetime and need to be changed frequently depending on the amount of use. When a septum is no longer efficient, many problems may occur, such as leaks, decomposition, sample loss, change in split ratio, ghost peaks, and column degradation.

The column is the heart of a GC, where the chromatographic separation takes place. The selection of an appropriate column is one of the most important decisions to make because the chemical nature of the stationary phase has a great impact on the quality of the separation. The choice completely depends on the type of sample to be analyzed. There are four main variables to take into account: chemical nature of the stationary phase, thickness, column length and diameter. The most important is the enough strong interaction between the

stationary phase and analytes, otherwise, there will be limited retention and, therefore, limited separation. The column is located inside an oven, whose temperature can be easily changed to suit various applications and should be high enough so that the samples have a significant vapour pressure, allowing their separation in a reasonable time. To obtain a suitable separation for samples with numerous analytes the best solution is the temperature programming: starting at a low temperature, for the most volatile components, and then gradually increasing it, for the least volatile ones.

Finally, the task of a GC detector is to produce a measurable electronic signal in response to species eluting from the column. There is a great variety of detectors, some of them sensitive only to a specific type of chemicals compounds, whereas others capable of detecting almost everything, considered "universal". As a general rule, the more selective the detector, the greater its sensitivity. Universal detectors such as the flame ionization detector, FID, and the thermal conductivity detector (TCD), have sensitivities in the 10^{-11} g and 10^{-9} g respectively. Gas chromatographic analyses were performed using a GC Perkin Elmer 8500 equipped with a capillary column (GSQ 115-3432-J&W Scientific) and an FID and a TCD detectors respectively for hydrocarbons and CO_2 detection, whereas a Fisons 8000 equipped with a molecular sieves column (10 Å) and a TCD detector, to evaluate H_2 and permanent gases (Fig. 3.19).

Figure 3.19: GC appartuses

REFERENCES:

[1]   C. Suryanarayana (2004), Mechanical alloying and milling. *Mech. Alloy. Milling* **46**, 1–472.

[2]   Von G. Heinicke (1984), Tribochemistry. Berlin, Akademie-Verlag.

[3]   P. G. McCormick (1995), Application of Mechanical Alloying to Chemical Refining (Overview). *Materials Transactions, JIM* **36**, 161–169.

[4]   P. P. Ewald (1979), A review of my papers on crystal optics 1912 to 1968. *Acta Crystallogr. Sect. A* **35**, 1–9.

[5]   R. A. Young, The Rietveld Method. Oxford University Press (1993).

[6]   W. M. Van Gulik et al. (2012), Microbial Systems Biology: Methods and Protocols - Fast Sampling of the Cellular Metabolome. *Methods in Molec. Biology*, **881**.

[7]   E. Smith et al. (2005), *Modern Raman Spectroscopy - A Practical Approach*. *Modern Raman Spectroscopy - A Practical Approach*.

[8]   L. Stievano & F. E. Wagner, Mössbauer Spectroscopy, Ch. 10. Characterization of Solid Materials and Heterogeneous Catalysts: From Structure to Surface Reactivity. Wiley-VCH Verlag GmbH & Co. KGaA (2012).

[9]   G. Klingelhöfer et al. (2004), Jarosite and hematite at Meridiani Planum from opportunity's Mössbauer spectrometer. *Science (80).* **306**, 1740–1745.

[10]   R. V. Morris et al. (2004), Mineralogy at Gusev crater from the Mössbauer spectrometer on the Spirit rover. *Science (80).* **305**, 833–836.

[11]   S. Brunauer et al. (1938), Adsorption of Gases in Multimolecular Layers. *J. Am. Chem. Soc.* **60**, 309–319.

[12]   Z. U. Ahmad et al. (2019), Neodymium embedded ordered mesoporous carbon (OMC) for enhanced adsorption of sunset yellow: Characterizations, adsorption study and adsorption mechanism. *Chem. Eng. J.* **359**, 814–826.

[13]   S. R. Sandler et al. (1998), Thermogravimetric analysis. *Polym. Synth. Charact.* **1**, 108–119.

[14]   A. E. O'Keeffe (1965), Mass spectrometry and gas chromatography. *Chem. Eng. News* **43**, 4.

Chapter 4: Results and Discussion

4.1 INTRODUCTION

As previously mentioned in the first chapter, the main focus of this thesis is the study of the interaction between Olivine and CO_2 in the presence of water, and of the subsequent induction of the serpentinization process by mechanical grinding. Attention has been focused on the investigation of the different stages of the mechanism and to the consequent production of light hydrocarbons.

In this context, various strategies have been adopted in order to achieve these objectives.

The first strategy, based on previous preliminary results, involved the study of the mechanochemical activation of Olivine in the presence of water and CO_2, with different reaction stoichiometry and at different partial pressures of CO_2, focusing on the structural nature of the transformation. The mechanical treatments were carried out by employing high energy laboratory-scale ball mills, Spex Mixer/Mill, Mod.8000: these were suitably modified in order to control the engine rotation speed, and the milling vials were equipped with a leak-proof valve to be properly used as mechanochemical batch reactors. Structural characterization of the samples was carried out by resorting to several different complementary instrumental techniques, with the aim to reach a deep reaction mechanism comprehension.

In the second strategy, on the other hand, we modified some operating parameters, such as the milling power, the type of mill (Fritsch Pulverisette), the mass to powder ratio and the pressure conditions, in order to verify how such parameters may affect the whole process.

4.2 EXPERIMENTAL BACKGROUND

The present work aims at providing new insights into the study of the mechanically activated reaction between olivine and CO_2 in the presence of water to form hydrogen and light hydrocarbons.

In situ reactive ball milling was performed using a dedicated mechanochemical reactor which allows processing powders under CO_2 atmosphere. A detailed structural and microstructural characterization by *ex situ* XRD and FT-IR analysis of the pre- and post-activated powders was carried out with the aim of gaining new insights into the mechanism. The first results evidenced that, under the mechanochemical activation conditions reported in this work, the production of methane and other hydrocarbons occurred with faster kinetics and higher yields if compared with the thermally activated reaction.

The below reported data have recently been published (doi:10.1016/j.powtec.2019.10.080) in *Powder Technology* and are here listed and discussed.

4.2.1 EXPERIMENTAL METHODS

Materials.

Olivine powders were provided by Sibelco Europe (Norway). X-ray fluorescence analysis provided by the supplier, indicated, approximately, 50% of MgO, 41.5% of SiO_2, and 7.3 % of Fe_2O_3, outlining that forsterite was the main component. Small amounts of secondary minerals such as Cr_2O_3 (0.29 %), Al_2O_3 (0.44 %), NiO (0.32 %), MnO (0.09 %), CaO (0.12 %), Na_2O (0.01 %) and K_2O (0.03 %), were also detected. Before each test, in order to remove finer particles

and adsorbed organic material, powder samples were washed in acetone in an ultrasonic bath for 5 minutes and subsequently dried at 150°C under vacuum[1].

Mechanical and thermal processing.

Mechanical treatments were performed by a SPEX Mixer/Mill 8000 operating at 875 rpm, charging 8 grams of olivine for each experiment. The powders were treated with different amounts of deionized water and the slurry obtained was then introduced in a stainless steel jar (volume of 76 cm^3). The reactor was equipped with two valves: one was used to introduce CO_2 in the reactor while the second allowed the gas sampling through a rubber septum. In order to remove air from the vial, flushing with CO_2 was carried out for 10 minutes before closing the sampling valve. Three experiments were conducted with increasing water amounts under CO_2 atmosphere. Mechanical treatments of 90, 140 and 210 minutes were performed using 2 ml, 4 ml and 6 ml of water, respectively, applying an initial pressure of 3 bar of CO_2. For these three experiments, one steel ball of 7.50 grams was used ensuring a ball-to-powder ratio of almost 1 (0.94) and inelastic collisions regime[2]. Gas samples were taken with a gas syringe (with a reduced volume) and analysed by means of gas chromatography. A Perkin Elmer 8600 equipped with a wide-bore column (GSQ 115- 3432-J&W Scientific) and a FID detector, was used for CH_4 and light hydrocarbons. A Fisons 8000 equipped with a molecular sieves column (10 Å) and an HWD detector, was used to evaluate H_2 and other permanent gases (CO). Specific standards for the quantitative analysis of CH_4 and hydrocarbons, and high purity carbon dioxide gas (N5 – 99.999%; CH_4 < 1ppm) was provided by Sapio (Italy). A representation of the experimental setup used for the mechanochemical tests, is reported Figure 4.2.1. To exclude catalytic effects of the grinding media, an experiment was conducted without introducing olivine powders: no hydrocarbons were detected above the detection limit.
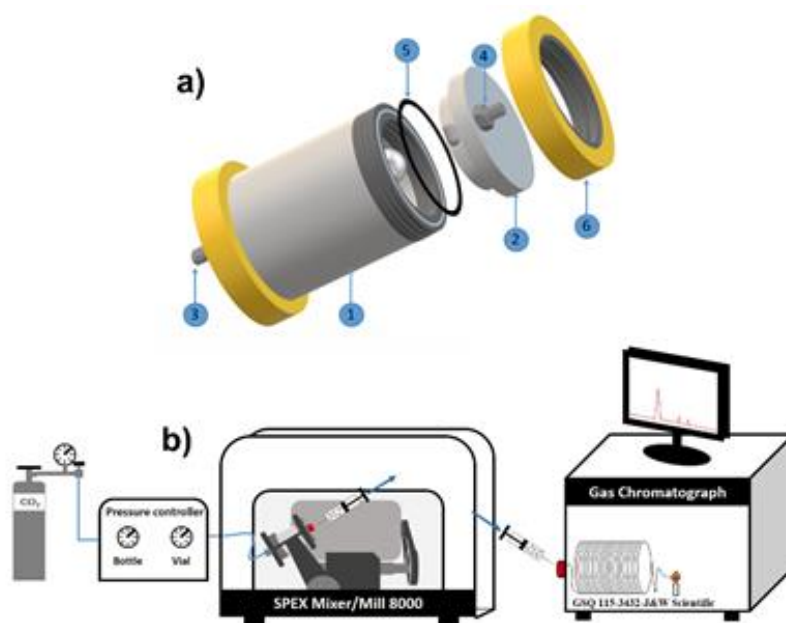
Figure 4.2.1: a) Mechanochemical reactor adapted for reactive high-energy ball milling: 1. External wall made of stainless steel. 2. Cap adapted for flowing gases. 3. Gas inlet with 1/8' Swagelok connection. 4. Gas outlet with 1/8' Swagelok connection. 5. O-ring. 6. Metal ring made of stainless steel. b) Scheme of the experimental setup for the investigation of the mechanochemical reaction.

A further experiment was performed under hydrothermal condition using a stainless-steel Parr reactor for high-pressure reaction, equipped with gas valves and temperature controller. As for BM experiments, 8 grams of olivine were used and an initial pressure of 3 bar of CO_2 was applied. 6 ml of deionized water were then introduced and the wet powders heated from RT to 300°C (heating rate of 20°C/min). Sampling started when the temperature reached 300°C (at lower temperature the formation of hydrocarbons was not valuable). Experiments performed under Ar atmosphere for both the mechanochemical and hydrothermal processes did not reveal any organic compound, excluding discernible amounts of background organic carbon and possible contaminations. Moreover, experiments performed under dry conditions showed no evolution of gaseous products.

Characterization methods.

Phases and microstructural evolution of the milled powders were characterized by means of Rigaku X-ray Diffractometer (XRD) with a Bragg–Brentano geometry using Cu Ka radiation (λ = 1.54178 Å) and a graphite monochromator in the diffracted beam. The microstructural parameters were evaluated by fitting the full XRD patterns using MAUD (Materials Analysis Using Diffraction), a diffraction/reflectivity analysis program based on the Rietveld method. The Rwp (weighted-pattern factor) parameter was used as numerical criterion for the quality of the agreement between calculated and experimental diffraction data[3]. In this regard, the Rietveld method has already been reported as the most suitable approach to characterize the microstructure of olivine and mine waste materials containing olivine[4]. Fourier transform infrared spectroscopy (FT-IR) measurements were carried out by the Jasco 480 Plus instrument. All samples were ground with ultra-dry KBr and pressed into the shape of pellets. N_2 sorption isotherms were collected on a Sorptomatic 1990 instrument and the data were analysed according to BET and BJH to evaluate surface area and total pore volume of powders previously degassed at 120 °C under high vacuum.

Structural and texture characterization of pristine olivine.

Olivine powders provided by Sibelco Group were further characterized by X-ray diffraction and the experimental pattern analysed by the Rietveld method (Figure 4.2.2a).
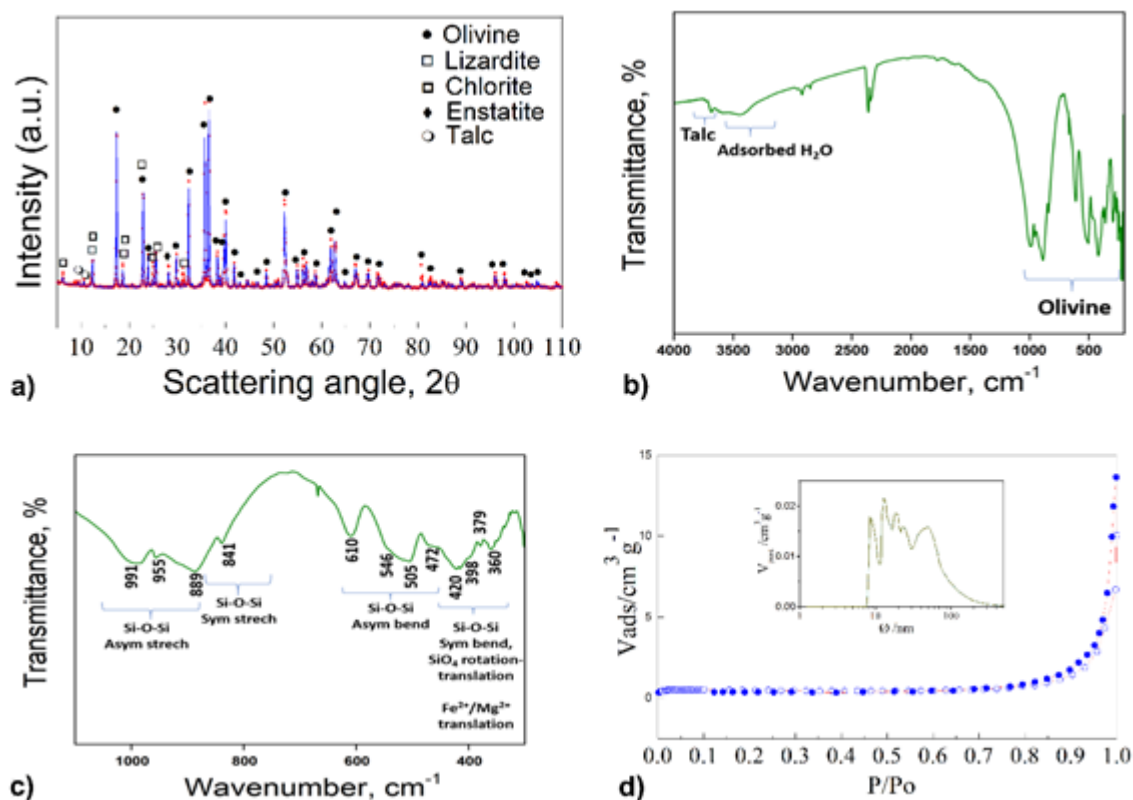
Figure 4.2.2: a) X-ray diffraction pattern of the raw olivine supplied by Sibelco. The experimental pattern and the Rietveld profile are indicated by red squares and full blue line, respectively. b) FT-IR spectrum of the pristine olivine. c) detail in the wavenumber range of 1100-300 cm^{-1}. d) N$_2$ sorption (empty blue circles) and desorption (full blue circles) isotherms of pristine olivine. The pore volume distribution (green line) is depicted in the inset.

The quantitative analysis showed that olivine was the primary phase (84.2 wt.%) while secondary phases as lizardite $Mg_3Si_2O_5(OH)_4$, enstatite $(Mg,Fe)SiO_3$, talc $(Mg,Fe)_6(Si_8O_{20})(OH)_4)$ and chlorite $(Mg,Fe^{2+},Fe^{3+})_6AlSi_3O_{10}(OH)_8$ were present with percentages of 0.9 wt.%, 7.4 wt.%, 1.1 wt.% and 6.4 wt.%, respectively. The estimated composition, reported in Table 4.2.1, together with microstructural parameters, was in line with the expectation observed by Turianicová et al.[5]. The FT-IR spectrum of the olivine powders is shown in Figure 4.2.2b. The comparison of the peak positions with the data reported in the literature confirms the XRD results. The bands in the regions 1200 and 300 cm^{-1} can be attributed to olivine while the peak around 3677 cm^{-1} is characteristic of the O-H symmetric stretching in talc[6,7]. In addition, the intensity and the shape of the olivine peaks prove the prevalence of the

71

forsteritic component, with a percentage of about 90 wt.%. Such percent ratio agrees with that found by normalisation of the analytical data produced by XRD and XRF analysis performed on natural olivine from other deposits[4].

Phases	a, Å	b, Å	c, Å	α, °	β, °	γ, °	<D>, Å	r.m.s %	Wt. %
Olivine	4.758	10.215	5.989	-	-	-	>1500	0.0597	84.2
Lizardite	5.513	5.393	7.154	86.961	91.917	122.175	1400	0.0632	0.9
Enstatite	18.233	8.828	5.223	-	-	-	1500	0.0607	7.4
Talc	9.973	18.098	5.387	-	107.543	-	1190	0.0594	1.1
Chlorite	5.227	9.226	14.368	91.270	95.968	90.103	1502	0.0605	6.4

Table 4.2.1: Structural and microstructural parameters estimated by Rietveld method on the patterns of the supplied olivine.

Specifically, in Figure 4.2.2c, the peaks at 991, 955 and 889 cm^{-1} correspond to the asymmetric stretching of the Si-O groups while the band located at 841 cm^{-1} is referred to the symmetric stretching. For the same functional group, the asymmetric bending peaks are observed at 610, 546, 505 and 472 cm^{-1}. The residual absorption bands in the range of 500-300 cm^{-1} are associated with the rotational and translational symmetric bending of the SiO_4 group and to the bivalent cations, Fe and Mg, contained in the pristine olivine. Specific surface area, pore dimension and volume of the olivine powders were estimated through nitrogen physisorption (Figure 4.2.2d). As expected, the as-received olivine showed very low surface area, equal to 1.46 m^2/g, slightly higher than the values reported in the current literature[8,9]. According to the IUPAC classification, the experimental isotherm depicted in Figure 4.2.2d, can be associated with a type IV, typical of mesoporous materials. However, a wide pore size distribution (inset in Figure 4.2.2d) ranging from 10 to 200 nm, is observed, which implies the presence of disordered pores in the mesoporous

and macroporous region. Finally, the cumulative pore estimated corresponds to a 0.0211 cm³/g.

4.2.2   RESULT AND DISCUSSION

Mechanical activation of the olivine powders under CO₂ atmosphere.

Powders were initially exposed for 40 minutes to the gaseous atmosphere under static conditions, but as expected, no measurable CO_2 conversion could be observed. The mechanical processing of the wet olivine induced the conversion of the carbon dioxide in the ball milling reactor, as it can be observed in the evolution of light hydrocarbons measured by GC and shown in Figure 4.2.3a (2 ml H_2O).
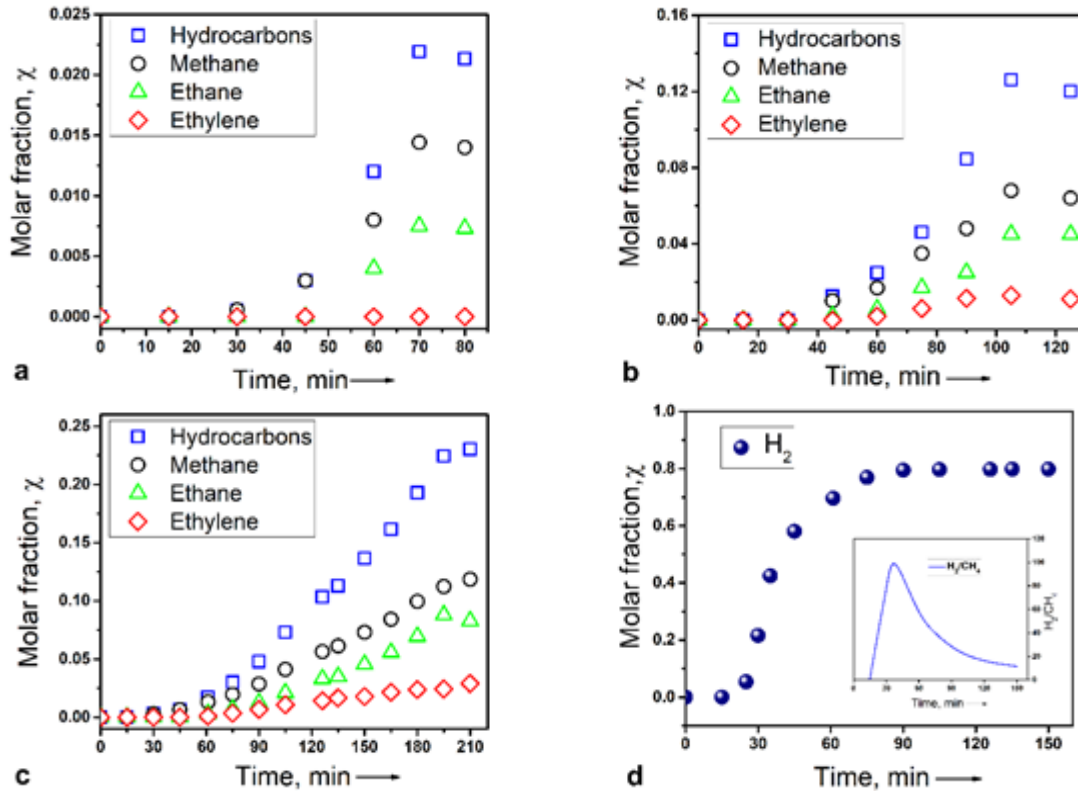

Figure 4.2.3: Kinetics of hydrocarbons generation during BM of olivine in presence of 2 (a), 4 (b) and 6 (c) ml of water. (d) H_2 production and H_2/CH_4 ratio (inset) of the system milled with 6 ml of water plotted as a function of the milling time.

After an induction period of about 30 minutes, hydrocarbons formation increased almost linearly up to a maximum rate of r = 6.15×10^{-2} µmol s^{-1}, while the amount of methane (black circles) approached asymptotically to 0.13 mmol. However, only 5% of the CO_2 initially introduced in the reactor was converted to hydrocarbons when 2 ml of H_2O was used. In order to optimize the process, further experiments were then performed in the presence of higher amounts of water. A better conversion performance was recorded in the system milled with 4 ml of water (Figure 4.2.3b). Methane was detected after 30 minutes of milling and the formation rate of the total hydrocarbons increased up to a maximum value of r = 0.25 µmol s^{-1}, four times higher than the value reported for the system containing 2 ml of water. The contribution of the ethane (green triangles) and ethylene (red rhombus) to the total hydrocarbons produced, was significantly higher with respect to the first experiment. While a similar selectivity was observed in the system milled with 6 ml of water (Figure 4.2.3c), a further increase of the total hydrocarbons produced was detected, reaching a maximum value after 200 minutes of milling.

A production rate of r = 0.22 µmol s⁻¹ resulted from this experiment, similarly to that of the system milled with 4 ml (0.25 µmol s⁻¹). However, the final amount of methane was around 1 mmol, significantly higher than the value obtained in the olivine treated with 4 ml of water (0.6 mmol). Conversion rates and yields of the three systems are resumed in Table 4.2.2.

Sample	Gas	Yield µmol	Specific yield µmol kg⁻¹	Conversion rate µmol s⁻¹	Specific Conversion rate µmol s⁻¹ kg⁻¹
Olivine + 2 ml H₂O BM	CH₄	131	16.375	3.9*10⁻²	4.87
	CH₃CH₃	68	8.500	3.09*10⁻²	3.86
	CH₂CH₂	-	-	-	-
	Total	199	24.875	6.15*10⁻²	7.69
Olivine + 4 ml H₂O BM	CH₄	618	77.250	1.04*10⁻¹	13.00
	CH₃CH₃	410	51.250	6.77*10⁻²	8.46
	CH₂CH₂	117	14.625	2.58*10⁻²	3.22
	Total	1.146	143.250	2.5 *10⁻¹	31.25
Olivine + 6 ml H₂O BM	CH₄	1.021	127.625	1.03*10⁻¹	12.87
	CH₃CH₃	799	99.875	9.19*10⁻²	11.48
	CH₂CH₂	263	32.875	2.77*10⁻²	3.46
	Total	2083	255.250	2.2*10⁻¹	27.50
Olivine + 6 ml H₂O 300° C	CH₄	315	39.375	5.43*10⁻²	6.78
	CH₃CH₃	-	-	-	-
	CH₂CH₂	-	-	-	-
	Total	315	39.375	5.43*10⁻²	6.78

Table 4.2.2: Yield, conversion rate and specific conversion rate of the hydrocarbons obtained under mechanical and thermal activation.

In this regard, it is worth mentioning that the amount of methane obtained upon the mechanical treatment of olivine with water and carbon dioxide is significantly higher than that (0.0838 mmol) previously reported for low-temperature thermal conversion of carbon dioxide and hydrogen using reduced Rh/Al₂O₃ heterogeneous catalysts[10]. Considering that both processes operate at room temperature, and the cost of the starting materials, the reactions here studied can be then considered quite promising for practical applications. From a qualitative point of view, the observed hydrocarbons distribution is similar to

that obtained under hydrothermal conditions by Foustoukos et al., which measured methane, ethane and propane but not ethylene[11]. Other hydrocarbons are, in fact, typically generated during thermally catalysed Fischer-Tropsch-Type (FTT) processes, while the role of BM in triggering condensation and polymerization processes is well supported by previous experiments already reported in the literature[12-14]. The ratio of hydrocarbons with increasing C numbers is usually constant in FTT reactions and its distribution is represented by the Schulz-Flory relationship where the log of the gas concentration at the final stage is linearly correlated to C number[15]. In the present work the C_2/C_1 ratio was roughly 0.33 (where 1 and 2 are the number of carbon atoms corresponding to methane and, ethane and ethylene, respectively), in line with previous studies, which indicate a high probability for C-C bonding with respect to C-H. Indeed, a value of 0.33 was reported for an extended range of hydrocarbons produced through FTT reactions catalysed by magnetite, Fe_3O_4. This mineral is often formed during the serpentinization process (see reaction 1) and was shown to trigger the generation of hydrocarbons by catalysing the conversion of carbon-based compounds in the presence of molecular hydrogen[14,15]. In the present work, the generation of H_2 was followed during the mechanical processing of olivine in order to provide a further evidence of the serpentinization mechanism. As an example, the evolution of H_2 during the BM of olivine in the presence of 6 ml of H_2O is reported as a function of the milling time in Figure 4.2.3d (navy full circle). As expected, a large amount of hydrogen gas was detected, confirming that reaction 1 can be mechanically activated. Moreover, the release of H_2 showed an induction period of 20 min, which is significantly lower compared to those observed for methane and other C-H based gases (30-40 min). The ratio of H_2 to CH_4 generated, represented by the blue line in the inset of Figure 4.2.3d, is similar to those reported by Oze and

collaborators[16]. This trend was related to the FTT process catalysed by *in situ* generated magnetite during the serpentinization reaction, confirming the Schulz-Flory relationship emerged in this work.

Structural investigation on the processed powders.

To further corroborate the features resulted from the gases evolved during ball milling and get more insights on the mechanism behind the process, structural and microstructural characterizations were performed by X-ray diffraction and FT-IR spectroscopy on the post milled olivine (6 ml H_2O). With respect to pristine olivine, the mechanical processing under CO_2 leads to generalized reflections broadening and amorphization, together with the formation of a significant amount, 12.5 wt.%, of magnesite (pale blue line in Figure 4.2.4a) with a cell volume Vc of 289 $Å^3$. To this regard, Jones et al. previously reported that, together with Mg^{2+}, also part of Fe^{2+} ions of olivine were rapidly incorporated into siderite ($FeCO_3$) when oversaturated carbonate was used under hydrothermal conditions[17].

It can be then supposed that a solid solution composed by $MgCO_3$ *($Vc \approx 280Å^3$)* and $FeCO_3$ *($Vc \approx 293Å^3$)*, namely $(Mg,Fe)CO_3$, was formed after BM of olivine and water under CO_2 atmosphere. Carbonate precipitation represents a non-oxidative inorganic pathway for carbon sequestration, competing with the serpentinization reactions[17-20].

The incorporation of Fe^{2+} into carbonates, under specific conditions is, in fact, faster with respect to oxidation processes related to serpentinization. Several works proved that mechanical preactivation of substrates can strongly improve the direct aqueous mineral carbonation of silicates[5,21,22].

Different reaction pathways have been proposed for the formation of magnesite through the weathering of olivine under CO_2 atmosphere. For example, Turianicová et al., suggested that pre-milled olivine reacts with water forming,

in a first step, brucite (Mg(OH)$_2$) which, in a second step, interacts with CO$_2$ gas to give a hydrated form of magnesite, (MgCO$_3$)$_4$ Mg(OH)$_2$*4H$_2$O, energetically favoured with respect to the anhydrous species[5].
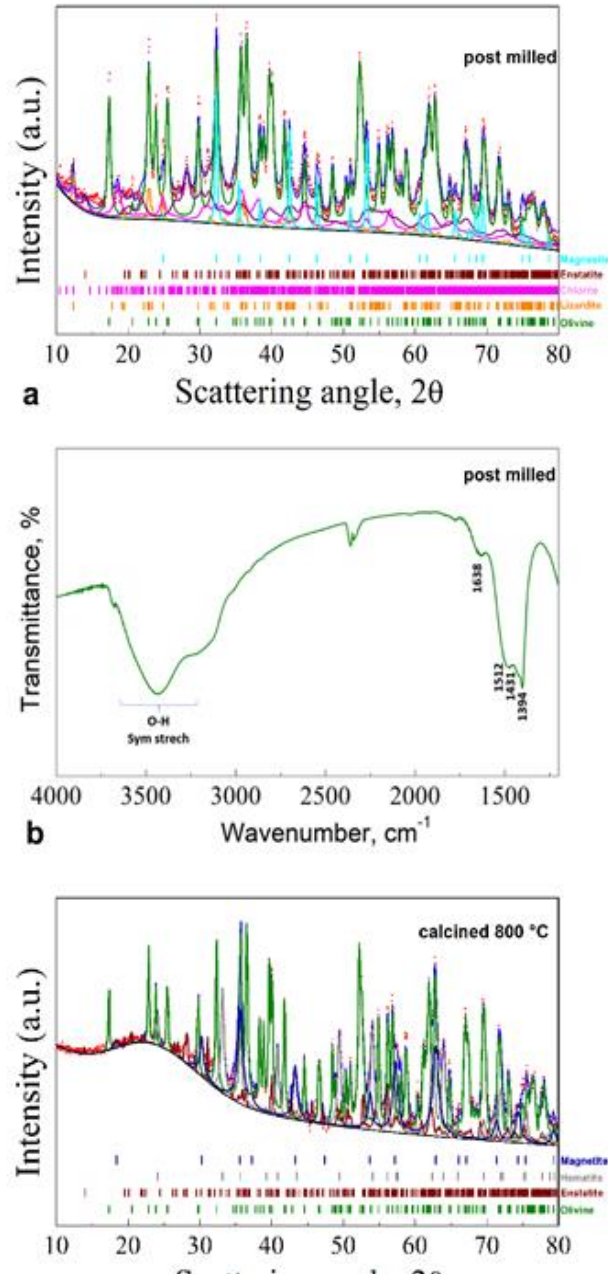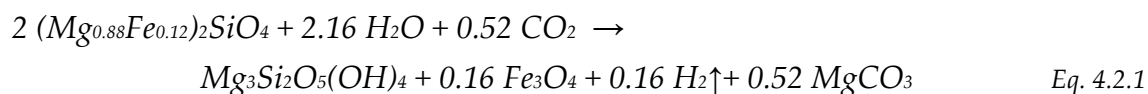

Figure 4.2.4: X-ray diffraction pattern (a) and FT-IR spectrum (b) of the post milled olivine. (c) X-ray diffraction pattern of the post milled olivine calcined at 800 °C. XRD intensities are in logarithmic scale.

However, in this work, no intermediate phases could be observed and magnesite was detected instead of the hydrate phase, highlighting that different experimental conditions can affect the carbonation process and its related products. Finally, the quantitative analysis of XRD pattern reported in Figure 4.2.4a, shows a significant decrease of the olivine phase (73.5 wt.%) after BM, while lizardite, the most common product of the of serpentine minerals, increases up to 4.5 wt.%, confirming that the reaction of serpentinization occurs under these mechanochemical conditions. Furthermore, with respect to olivine, serpentine minerals easily undergo amorphization during milling[4]. It is then plausible to consider that the amount of lizardite produced could be greater than that estimated by Rietveld refinement, which is based only on the crystalline fraction of the sample. The remaining minerals, namely chlorite and enstatite count to 2.5 and 7 wt.%, respectively, while talc (< 1 wt.%) is below the detection limit. FT-IR measurements performed on the post milled system and shown in Figure 4.2.4b, indicate the presence of two new characteristic bands, related with the carbonate groups, centred at 1512 and 1431 cm^{-1}, in agreement with the XRD results[5,8]. FT-IR also evidenced the occurring of a partial serpentinization process, showing a very intense and broad absorption peak around 3500 cm^{-1} ascribable to the symmetric stretching of O-H groups formed on the olivine surface[5,8,23]. The peak at 1638 cm^{-1} typical of OH-bending can be also related with H_2O adsorbed on the ball-milled olivine[5,8]. However, no FT-IR bands or XRD peaks indicating the presence of Fe_3O_4 (see Eq. 4.2.1) were observed, which could depend on its nanosized conditions reached upon BM process as also experimentally revealed by Kihal et al.[24] To gain more information on the crystalline products, the post milled powders were then calcined at 800 °C. The XRD pattern of the calcined sample, shown in Figure 4.2.4c, reveals the presence of crystalline Fe_3O_4-magnetite (7 wt.%) and Fe_2O_3-

hematite (9 wt.%), together with olivine (78 wt.%) and enstatite (6 wt.%). The peaks related to serpentine (lizardite) disappeared, not unexpectedly given that it decomposes at temperature higher than 660 °C, while the presence of hematite can be explained by the partial oxidation of magnetite during the thermal treatment. Starting from this experimental evidence, a first description of the overall mechanochemical process can be then proposed, although more details on the solid intermediates are necessary for fully defining the mechanism under such unconventional conditions. In the mechanochemical reactor, olivine reacts first with water, producing serpentine and nanostructured magnetite, as well molecular hydrogen. Such products react in a second step with CO_2 producing magnesium/iron carbonate. These two reactions can be summarized by the reaction (Eq. 4.2.1):

$$2\ (Mg_{0.88}Fe_{0.12})_2SiO_4 + 2.16\ H_2O + 0.52\ CO_2 \rightarrow$$
$$Mg_3Si_2O_5(OH)_4 + 0.16\ Fe_3O_4 + 0.16\ H_2\uparrow + 0.52\ MgCO_3 \qquad Eq.\ 4.2.1$$

In this regard, it is worth noting that the hydrogenation of carbon dioxide to produce hydrocarbons takes place after an induction period which is expected to be related to the formation of the FTT catalyst magnetite, as previously observed during experiments conducted under hydrothermal conditions[16].

Mechanochemical insights.

The experimental findings described in the previous sections demonstrate the existence of a similar mechanism in the mechanochemical and thermal FTT reactions of olivine. On the other hand, the rates of formation of hydrocarbons were significantly higher for the mechanically activated process conducted at room temperature. From the current literature, CH_4 production rate of $2.5*10^{-3}$ $\mu mol\ kg^{-1}\ s^{-1}$ was achieved when the reaction of olivine and water was performed under 200°C and 300 bars of CO_2[16]. This value was three/four orders

of magnitude lower than that obtained under the milder conditions characterizing the mechanical process used in this work (30 °C and 3 bars of CO_2) (see Table 4.2.2). A possible reason for this marked difference can be found in the evolution of the reactive surface areas that are expected to significantly increase during the intensive milling treatment.
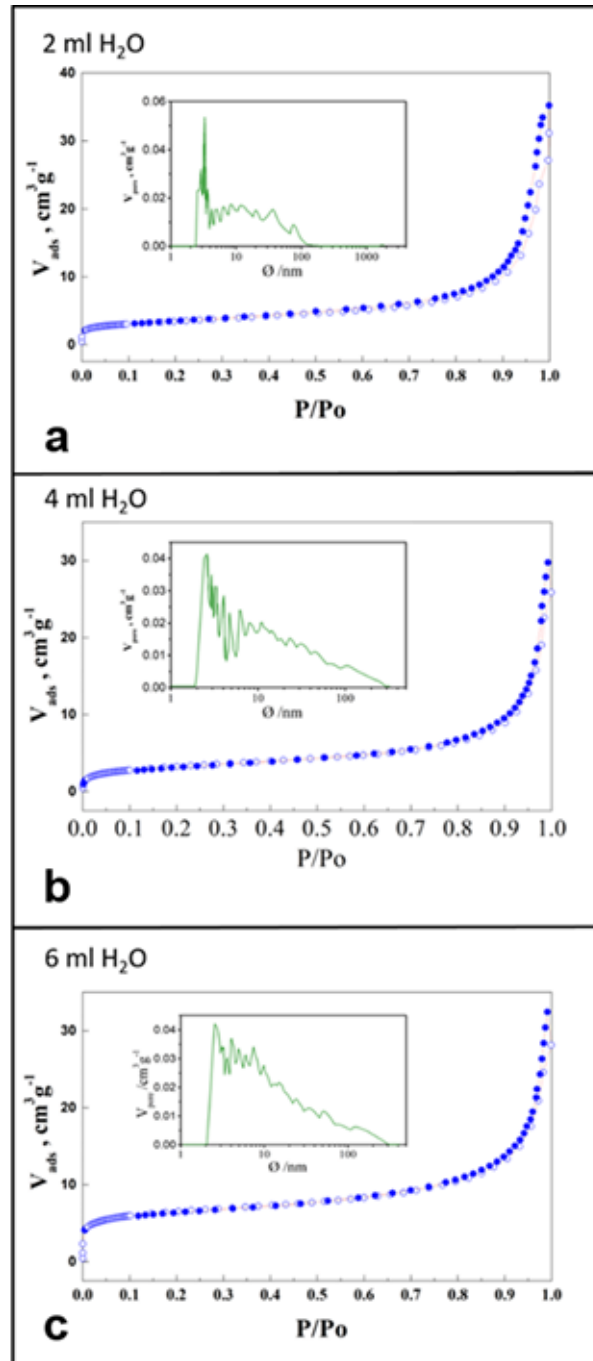

Figure 4.2.5: N_2 physisorption isotherms of the post-milled olivine powders milled with 2 (a), 4 (b) and 6 ml (c), of water. The corresponding volume pore distribution (green line) is depicted in the inset.

81

This is consistent with the BET analysis of the N_2 ad-desorption isotherms performed on the post-milled powders, as the surface area of the three milled systems, 11.82 (2 ml), 14.42 (4 ml) and 22.04 m^2/g (6 ml), resulted significantly higher with respect to that of pristine olivine (1.46 m^2/g – Figure 4.2.1 d).

The isotherms shapes reported in Figure 4.2.5 were very similar for all the range of P/P0. Furthermore, the distribution of the pores volume (green line in the panel) evaluated by the BJH model starts from 2 nm for all the three analysed samples. To better define the role played by the surface area of olivine powders, a further experiment was performed under isothermal conditions by heating to 300° C a slurry composed by 8 g of pre-milled (3h) olivine (surface area ≈ 20 m^2/g) and 6 ml of deionized water.

As for the mechanochemical experiment, an initial pressure of 3 bar of CO_2 was applied and gas sampling was performed at 300 °C for 210 minutes.
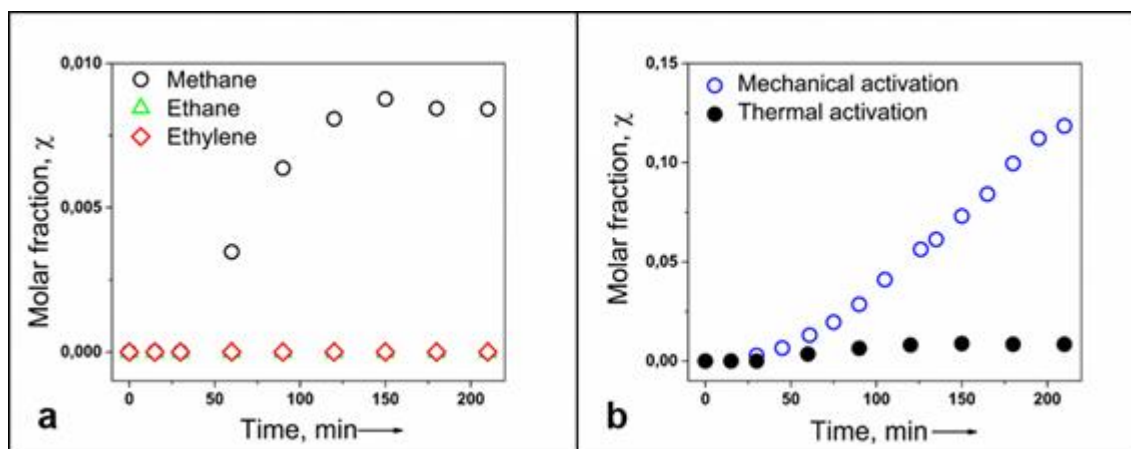

Figure 4.2.6: a. Evolution of methane, ethane and ethylene gases products, generated by the reaction of olivine powders and water (6 ml) under 300°C and 3 bars of CO_2. b. A direct comparison of the methane evolution during the reaction of wet olivine with CO_2 performed under mechanical (empty blue circles) and by thermal (black full circles) activation.

The graph reported in Figure 4.2.6a, shows that methane (black circles) was the most abundant product, while ethane (green triangles) and ethylene (red rhombuses) were revealed in traces.

For this reason, in this specific case, the total hydrocarbons approximately corresponded to the amount of methane evolved. The conversion of methane reached the maximum yield after 120 minutes of isothermal treatment with a rate of 6.78 μmol kg^{-1} s^{-1} (Table 4.2.2). The high selectivity to methane with respect to other hydrocarbons for olivine weathering process conducted under isothermal conditions was already reported in the literature[16-19]. However, although the methane produced was higher here than in previous works, a significant difference between thermal and mechanochemical activation can be appreciated by comparing the two processes reported in Figure 4.2.6b. It is important to notice that the enhanced catalytic activity exhibited during the mechanically activated FTT process, cannot be simply related to the defects produced on the powders. The powders used in both processes were in fact ball milled and, in addition, have similar specific surfaces. Such behaviour confirms that the main contribution to methane formation during the mechanical treatment of olivine powders regards the chemical reaction occurring at each impact: a very small fraction of powder reacts with gases during the collisions forming light hydrocarbons. The difference in light hydrocarbons production rate can be then ascribed to the enhanced reactivity of the powders caused by a dynamic alteration of the olivine structure that takes place at each individual collision during the mechanical processing. A further effort is then necessary to compare, on absolute basis, the catalytic data obtained for the mechanically and thermally activated processes. The number of CH_4 moles, r^*, converted per collision, can be estimated dividing the methane formation rate, $1.03*10^{-7}$ mol s^{-1}, by the average frequency of collision, N, being here equal to about 29.2 Hz. The milling time, t, and the number of impacts, n, exhibit in fact a direct proportionality as indicated by the relation $n = N * t$, but only if an inelastic regime of collisions is maintained during the mechanical process. Considering

the experimental approach used in this work (8 grams of powers and a single ball), the mechanical treatment takes place under constant collision frequency, and r^* corresponds to $3.53*10^{-9}$ mol. Taking into in account that the duration of each inelastic collision, t^*, is 1 ms, a new rate of methane conversion, k_{mech}, derived from the impact, can be obtained. The resulting k_{mech} value is $3.53*10^{-6}$ mol s^{-1} and it can be normalized to m_p^*, that represents the amount of powders trapped on the average at the individual collision. This amount is estimated to be 1 mg in the mechanochemical experiment conducted by using 1 stainless steel ball of 8g[25]. k_{mech} is then roughly equal to $3.53*10^{-3}$ mol g^{-1} s^{-1} and it indicates the apparent rate of production of CH_4 moles over the mass of powder processed at collision. The k_{mech} can be now compared with the apparent rate calculated for the isothermal process using a similar approach. Assuming that the whole powders, m_p, contribute to the isothermal reaction, k_{therm} will correspond to $6.79*10^{-9}$ mol g^{-1} s^{-1}, six orders of magnitude smaller than the apparent rate obtained under mechanical activation. Such a notable conversion activity in the mechanically activated process could be connected with the localized temperature experienced by the trapped powders at each collision. A rough estimate of the temperature difference, $\Delta T = (T_{mech} - T_{therm})$, for the methane conversion processes can be done by assuming that in both processes the apparent rates and are governed by the Arrhenius law. Thus, ΔT corresponds to $\frac{E_a}{k_b} \left(\left(\frac{1}{\ln\frac{Z_{mech}}{k_{mech}}} - \frac{1}{\ln\frac{Z_{therm}}{k_{therm}}} \right) \right.$ where k_b is the Boltzmann constant, E_a the activation energy and Z the collision frequency[13]. For an activation energy of 85 kJ/mol (typical of Fe-based catalysts used on FTT reaction), the resulting ΔT is equal to 348 °C, which means that a local T_{mech} of 648 °C is expected for the production of methane under mechanochemical activation. This scenario is not surprising: numerical calculations and dedicated experiments both evidenced that high temperatures (200-1500 °C) can be achieved as a consequence of the

frictional heat produced and dissipated during each singular collision[25-27]. It is also important to highlight that, together with a relative increase of the local temperature, the powders subjected to each collision undergo very high pressure conditions, of the order of a GPa at each point of contact[28,29]. However, an experimental protocol able to determine the direct influence of the local temperature and pressure, and to characterize the chemical and physical reactivity of the surface of the powders at each collision is still missing. The short duration of collisions (1 ms) and the rearrangements lifetime involved in the frictional processes at the surface (100 ps), combined with the stochastic dynamic motion of the milling ball, represent, to date, important issues from an experimental point view. For these reasons, although with some limitations, the study of kinetics curve is actually the most suitable methodological approach capable of providing qualitative information and few quantitative parameters on the mechanism of mechanochemical reactions, as further verified by this work. The inferences of the here reported investigation are multiple. On the one hand, the fast kinetics and relevant yield of hydrocarbons, ascribable to the extreme local conditions realized under mechanical processing, is certainly promising for converting efficiently CO_2 to chemical fuels. On the other hand, being the serpentinization process related with the abiotic production of methane, activation by mechanical stress represents an hitherto unexplored and fascinating scenario[30]. This is supported by recent studies on laboratory rock friction, carried out by ball milling setups, that revealed how physical and chemical transformation of minerals, which might imply the production of gases, occurs in faults during earthquakes[31-33]. The friction process involved in an earthquake can induce, in fact, several deformations, local temperatures and pressures on the fault rocks, of the same entity to those occurring in mechanochemical reactions[33].

4.2.3 CONCLUSION

This work provides experimental information on the mechanically activated reaction between olivine, a natural Fe-Mg silicate, and water under CO_2 atmosphere. For the first time, to the best of our knowledge, experimental findings establish that serpentinization process of olivine can proceed via *in situ* reactive ball milling, generating, in a second step, hydrocarbons through the hydrogenation of CO_2. XRD and FT-IR together confirm that the reaction mechanism is similar to that occurring under hydrothermal conditions: the olivine powder reacts with water to produce a significant amount of hydrogen gas and serpentine mineral. After an induction period, the hydrogen reduces carbon dioxide to hydrocarbons through the FTT process possibly catalysed by magnetite formed *in situ* as a consequence of the partial oxidation of ferrous Fe^{II} (contained in pristine olivine) to ferric Fe^{III}. An additional detail that emerged from the structural characterization is that carbonation, proved by the detection of the iron-magnesite, competes with serpentinization when olivine is subjected to mechanical processing. This side reaction has a negative effect on the hydrocarbon yield, but represents a valid alternative process for fixing carbon dioxide at low temperature. Nevertheless, a direct comparison with the reaction conducted by conventional hydrothermal methods (200°C - 300 bars) shows that a significantly higher specific conversion rate of methane (0.0025 μmol kg^{-1} s^{-1} vs 13.0 μmol kg^{-1} s^{-1}) is obtained in the mechanically activated process which operates under milder conditions (30°C – 3 bars CO_2). Texture characterization combined with the study of the kinetics of gaseous products evolution, proves that the enhanced activity observed under mechanical activation is not related to an increase of the specific surface area of the starting powders. It originates, instead, from the raised reactivity of the surface catalyst that is consequent to the heat dissipated during the collision event. Indeed, a temperature of about

648°C was estimated at each impact for the investigated reaction. The results reported in this work could then drive future research on the optimization of sustainable processes promoted by ball milling of minerals for mitigating CO_2 level and transforming it into added-value products. At the same time, they could open a new and promising research topic dealing with the origin of life, investigating the implications of mechanical effects on the generation of methane and more complex nitrogen/carbon-based species in ultramafic rocks. Finally, with the indirect estimation of the local temperature, further progress in the field of mechanochemistry have been realized for gas-solid reactions. However, the design of an innovative and direct experimental approach will be necessary to confirm the knowledge gained by the kinetic study of the mechanochemical reactions.

4.2.4 References

[1]   A. Neubeck et al. (2011), Formation of H_2 and CH_4 by weathering of olivine at temperatures between 30 and 70°C, *Geochem. Trans.*, **12**, 1–10.

[2]   F. Delogu et al. (2004), Mechanical work and conversion degree in mechanically induced processes, *Mater. Sci. Eng. A.* **382**, 280–287.

[3]   Scardi P. et al. (1994), Experimental determination of the instrumental broadening in the Bragg–Brentano geometry, *Powder. Diffr.* **9**, 180–186.

[4]   J. Li et al. (2016), Characterization of the microstructure of mechanically-activated olivine using X-ray diffraction pattern analysis, *Miner. Eng.* **86**, 24–33.

[5]   E. Turianicová et al. (2013), A comparison of the reactivity of activated and non-activated olivine with CO_2, *Int. J. Miner. Process.* **123**, 73–77.

[6]   I. Rigopoulos et al. (2015), Carbon dioxide storage in olivine basalts: Effect of ball milling process, *Powder Technol.* **273**, 220–229.

[7]   V.E. Hamilton (2010), Thermal infrared (vibrational) spectroscopy of Mg-Fe olivines: A review and applications to determining the composition of planetary surfaces, *Chemie Der Erde.* **70**, 7–33.

[8]   E. Turianicová et al. (2008), A possible way to storage carbon dioxide on mechanically activated olivine $(Mg,Fe)_2SiO_4$, VI Int. Conf. Mechanochemistry Mech. Alloy, 316–319.

[9]   P. Baláž et al. (2008), Structural changes in olivine $(Mg,Fe)_2SiO_4$ mechanically activated in high-energy mills, *Int. J. Miner. Process.* **88**, 1–6.

[10]   M. Jacquemin et al. (2010), Catalytic production of methane from CO_2 and H_2 at low temperature: Insight on the reaction mechanism, *Catal. Today.* **157**, 462–466.

[11]   D.I. Foustoukos et al. (2004), Hydrocarbons in Hydrothermal Vent Fluids: The Role of Chromium-Bearing Catalysts, *Science*, **304**,1002–1005.

[12]   G. Mulas et al. (2011), Hydrogenation of carbon monoxide over nanostructured systems: A mechanochemical approach, *Appl. Surf. Sci.*

[13]   F. Delogu et al. (2010), Hydrogen reactivity toward carbon monoxide under mechanochemical processing, *Int. J. Hydrogen Energy.* **35**, 4375–4381.

[14]   M.E. Berndt et al. (1996), Reduction of CO_2 during serpentinization of olivine at 300°C and 500 bar, *Geology.* **24**, 351–354.

[15]   T. Yoshida et al. (1993), Methanation of CO_2 with H_2 reduced magnetite, *J. Mater. Sci.* **28**, 1220–1226.

[16]   C. Oze et al. (2012), Differentiating biotic from abiotic methane genesis in hydrothermally active planetary surfaces, *Proc. Natl. Acad. Sci.* U.S.A. **109**, 9750–9754.

[17]   L.C. Jones et al. (2010), Carbonate control of H_2 and CH_4 production in serpentinization systems at elevated P-Ts, Geophys. Res. Lett. 37.

[18]   A. Neubeck et al. (2011), Formation of H_2 and CH_4 by weathering of olivine at temperatures between 30 and 70°C, *Geochem. Trans.*, **12**, 1–10.

[19]   J. Horita et al. (1999), Abiogenic methane formation and isotopic fractionation under hydrothermal conditions, *Science* **285**, 1055–1057.

[20]   T.M. McCollom et al. (2001), A reassessment of the potential for reduction of dissolved

CO$_2$ to hydrocarbons during serpentinization of olivine, *Geochim. Cosmochim. Acta.* **65**, 3769–3778.

[21] J. Li et al. (2016), Carbon dioxide adsorption isotherm study on mine waste for integrated CO$_2$ capture and sequestration processes, *Powder Technol.* **291**, 408–413.

[22] S.A. Wilson, Mineral traps for greenhouse gases in mine tailings: a protocol for verifying and quantifying CO$_2$ sequestration in ultramafic mines, Dissertation, University of British Columbia, Vancouver, 2009.

[23] M. Fabian et al. (2010), The influence of attrition milling on carbon dioxide sequestration on magnesium-iron silicate, *Miner. Eng.* **23**, 616–620.

[24] A. Kihal et al. (2009), Magnetic and Structural Properties of Nanocrystalline Iron Oxides, *Phys. Procedia.* **2**, 665–671.

[25] P. Baláž et al. (2013), Hallmarks of mechanochemistry: From nanoparticles to technology, *Chem. Soc. Rev.* **42**, 7571–7637.

[26] D.R. Maurice et al. (1990), The physics of mechanical alloying: A first report, *Metall. Trans. A.* **21**, 289–303.

[27] J. Joardar et al. (2004), Estimation of entrapped powder temperature during mechanical alloying, *Scr. Mater.* **50**, 1199–1202.

[28] S. Garroni et al. (2017), Mechanically activated metathesis reaction in NaNH$_2$–MgH$_2$ powder mixtures, *J. Mater. Sci.* **52**, 11891–11899.

[29] B. Yao et al. (2000), Effect of local pressure on the crystallization product of amorphous alloys induced by mechanical milling, *J. Non. Cryst. Solids.* **277**, 91–97.

[30] G. Etiope et al. (2018), Widespread abiotic methane in chromitites, *Sci. Rep.* **8**, 1–10.

[31] K. Saruwatari et al. (2004), Generation of hydrogen ions and hydrogen gas in quartz-water crushing experiments: An example of chemical processes in active faults, *Phys. Chem. Miner.* **31**, 176–182.

[32] T. Hirose et al. (2011), Mechanoradical H$_2$ generation during simulated faulting: Implications for an earthquake-driven subsurface biosphere, *Geophys. Res. Lett.* **38**, 1–5.

[33] T. Hirono et al. (2013), Importance of mechanochemical effects on fault slip behavior during earthquakes, *Geophys. Res. Lett.* **40**, 2988–2992.

4.3 HIGH ENERGY MILLING STRATEGY

The present work, based on the preliminary results, still focuses on the mechanically induced production of methane and light hydrocarbons during the interaction between olivine and water under CO_2 atmosphere. In this case, different reaction stoichiometry and different partial pressures of CO_2 have been investigated.

The results have been recently published (doi: 10.3389/fenrg.2019.00107) in *Frontiers in Energy Research* and summarized below.

4.3.1 MATERIALS AND METHODS

Olivine powders were provided by SATEF-HA (Italy). Chemical analysis reported by the supplier indicated the following relative composition expressed as weight % of oxide of each element contained in the material: 50.00% MgO, 41.50% SiO_2, 7.30% Fe_2O_3, 0.29% Cr_2O_3, 0.40% Al_2O_3, 0.30% NiO, 0.10% MnO, 0.10% CaO. High purity Carbon dioxide gas ($\geq 99.995\%$) was provided by Sapio (Italy).

The mechanical activation was carried out by a Spex Mixer Mill mod.8000, which was suitably modified to control the milling dynamic parameters (Delogu et al., 2004). As a mechanochemical reactor, we employed a stainless-steel vial (76 cm^3) equipped with two circular bases which were fitted with sealing valves. On one side, these valves allowed the connection to the gas reservoir (CO_2), and on the other side, to the GC apparatus for the analyses of gaseous reagents and products. The mechanical treatments were carried out on fresh powders at selected milling times. In order to remove the residual air from the vial, a dynamic vacuum of 10^{-3} mbar for 10 min was applied, before

introducing CO_2. Gas sampling was then performing 30 min after stopping milling and the gases analyzed by gas chromatography. Three series of experiments have been performed by charging the vial with 2 g of olivine, 0.3 ml of deionized H_2O, three stainless steel balls of 3.80 g each, and a rotation speed of 875 rpm. The reactor was then closed under CO_2 atmosphere under different conditions: (a) applying a constant pressure of 1.5 bar; (b) pressurizing the milling vial with an initial pressure of 1.5 bar; (c) filling the reactor with 1.0 bar. All the mechanochemical processes were conducted under low pressure of CO_2, in order to reproduce the reaction conditions expected under a real environment.

Methane, Hydrogen, and Light Hydrocarbons Evolution

Gas withdrawal from the reactor and injection in the gas sampling valves of gas chromatographs (GC) were performed by a gastight syringe. A GC Perkin Elmer 8600 equipped with a capillary column (GSQ 115-3432-J&W Scientific) and a FID detector, was used for CH_4 and light hydrocarbons detection. A Fisons 8000 equipped with a molecular sieves column (10 Å) and a hot wire detector (HWD), was used to evaluate H_2 and permanent gases. The conversion of CO_2, expressed as percentage (%), was calculated using the following equation:

$$CO_2 \; conversion \; (\%) \; = \frac{CO_{2 \; initial} - CO_{2 \; final}}{CO_{2 \; initial}} * 100 \qquad \qquad Eq. \; 4.3.1$$

where $CO_{2initial}$ and CO_{2final} correspond to the area of the peak showed by GC measurements before and after the mechanical treatment, respectively. Quantitative analyses were carried out through calibration curves setup by resorting to analytical standards, provided by Linde Gas Italia S.R.L.

Solid-State Samples Characterization

Powders were structurally characterized by means of a Rigaku SmartLab X-ray Diffractometer (XRD) with a Bragg–Brentano geometry using Cu Ka radiation (l = 1.54178 Å) and a graphite monochromator in the diffracted beam. Quantitative evaluation of phase abundance and structural features were obtained for all the XRD patterns, by non-linear least-square refinement procedure, according to Rietveld method, and using the MAUD (Materials Analysis Using Diffraction) software[1]. The thermogravimetric analyses were carried out by a Setaram Labsys DTA-TGA under Argon flux, by heating the specimens from room temperature to 1000° C, at a scanning rate equal to 5°C/min.

4.3.2 RESULTS

The crystallographic characterization of the olivine powders in the as-received state was performed by XRD using the Rietveld refinement method (Figure 4.3.1). In this way, phases were identified and their relative abundance and microstructural features were evaluated (Table 4.3.1).

Phases	a (Å)	b (Å)	c (Å)	α (°)	β (°)	γ (°)	r.m.s.(%)*	Wt (%)
Forsterite	4.77	10.23	5.99	-	-	-	0.0000021	90.8
Clinochlore	5.31	9.23	14.39	90.76	96.68	89.63	0.00523	1.7
Enstatite ferroan	18.24	8.83	5.19	-	-	-	0.00119	7.5

Table 4.3.1: Phase composition and structural parameters of Olivine in the as-received state. All data were obtained by Rietveld analysis on the pattern reported in Fig. 4.3.1, using MAUD software. (*)root mean square microstrain.
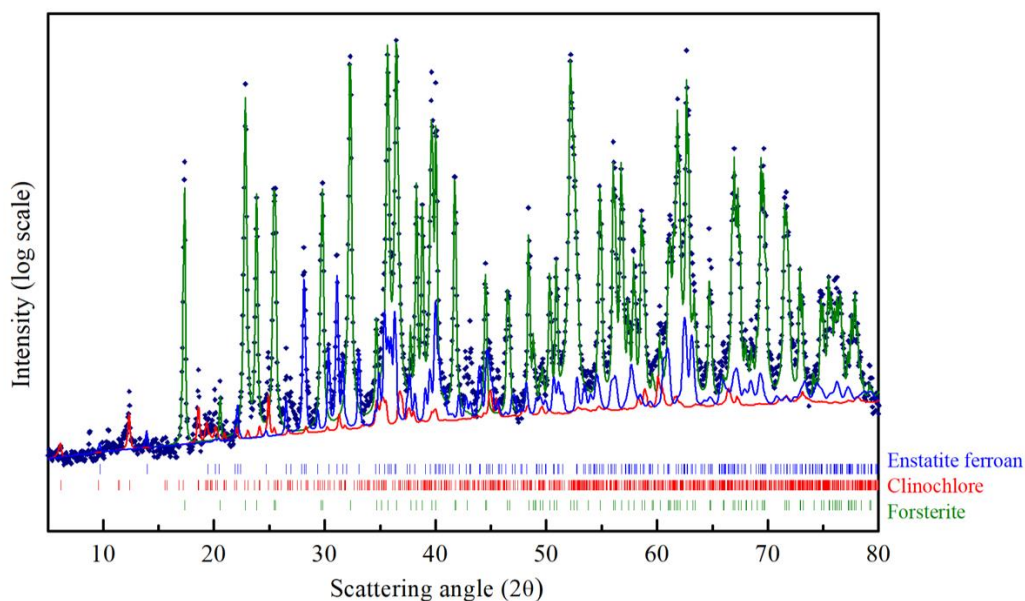
Figure 4.3.1: CuKα XRD pattern of the Olivine in the as received state. The structural refinement procedure by Rietveld method, allowed to quantitatively evaluate the contribution of the three phases indicated in the Figure: Forsterite (green line), Enstatite ferroan (blue line), Clinochlore (red trace).

The Mg-rich Olivine used in these tests (from now Olivine) consists of three phases: Forsterite ($Fe_{0.2}Mg_{1.8}SiO_4$), space group (s.g.) Pbnm, Enstatite ferroan ($Fe_{0.2}Mg_{0.8}SiO_3$), s.g. Pbca, and Clinochlore ($Al_{1.84}Fe_{0.5}H_8Mg_{4.5}O_{18}Si_{3.16}$), s.g. C-1. The Forsterite is the majority phase in the as-received olivine powders (91 wt%), with Enstatite as secondary phase (7.5 wt%).

As a general behaviour, mechanical activation tests of olivine with water under CO_2 atmosphere led to the production of different gas-phase products, which were detected by gas chromatography. The main hydrocarbons produced were methane, CH_4, ethane, C_2H_6, and ethylene, C_2H_4. As an example, the gas-chromatographic trace of olivine mechanically treated for 150 minutes is shown (Fig. 4.3.2).

The relative concentration of light hydrocarbons and other gas phase compounds, within the mechanochemical reactor, was evaluated by a calibration line obtained using certificated standard gas mixtures. Data plotted

in Fig. 4.3.2 indicate that the relative amount is: 0.23% v/v of methane, 0.036% v/v of ethane and 0.099% v/v of ethylene.
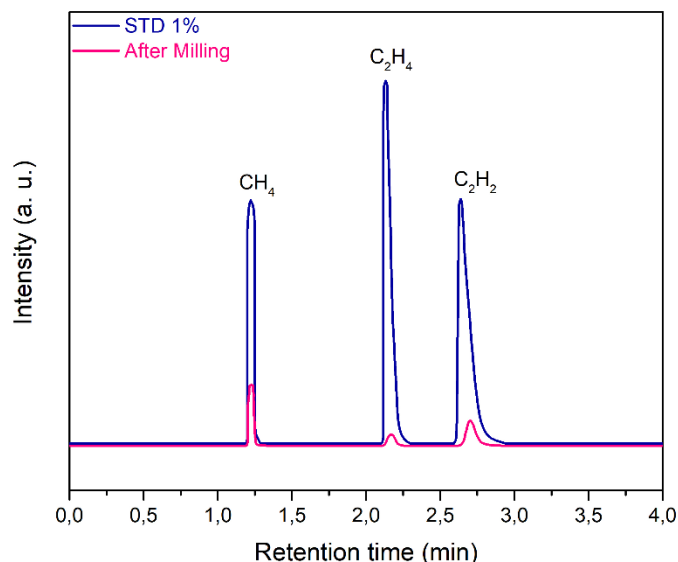

Figure 4.3.2: Gas-Chromatographic analysis, by FID, of the gas phase sampled from the mechanochemical reactor. Experimental data, reported as pink line, are compared with the relevant standard mixture data (STD), relative to 1% concentration value.

Moreover, it is safe to say that, at present, we cannot exclude the formation of traces of further heavier products, which could be in condensed liquid phase, or chemisorbed on the powder surfaces: this point is still under investigation. However, in the concern of the present work, we focused our attention mainly on the formation of methane. It should also be noted that in absence of CO_2 there was no methane formation, during two blank tests carried out by filling the jar with air or Argon.

The evolution of methane during the experiments performed under a constant pressure of 1.5 bar of CO_2 (with continuous flow) is presented in Figure 4.3.3. Data are reported in the graph as degree of conversion α, versus the milling time. The kinetics of evolution of methane concentration followed a sigmoidal shape, a trend often observed in chemical reactions involving solids as well as in gas-solid interaction processes, also activated by mechanical treatment[1,2].

The data suggest that methane formation rate, initially slow ($\alpha = 8{,}3 \cdot 10^{-3}$), increased up to reaching its maximum value after about 150 minutes of milling, and then CO_2 to CH_4 conversion progressively slows down, asymptotically approaching $\alpha = 1$, which corresponds to the CH_4 maximum concentration value, between 0.18–0.2 %v/v.
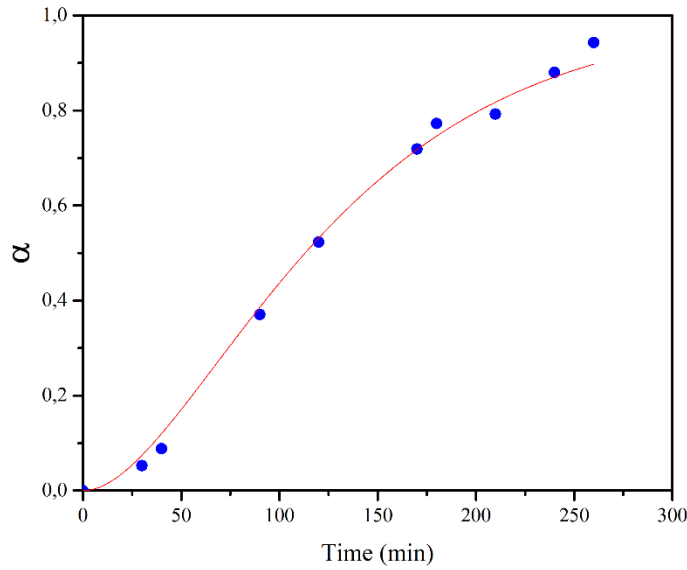

Figure 4.3.3: Methane concentration values in the gas phase mixture, reported as degree of conversion α, as a function of mechanical treatment time, t. Blue dots refer to experimental data, while continuous line represents the fitting curve according to the empirical equation reported in the text.

Experimental points can be fitted by the empirical equation $\alpha = 1 - (1 + kt)exp(-kt)$, in which t represents the milling time and k the apparent kinetic constant of the process and which has a value of $1.484*10^{-2}$ min^{-1}. Apart from the empirical approach, it should be noted that the actual process is rather complex, as it involves several steps, including surface adsorption of H_2O and CO_2, with molecular dissociation occurring over the surface, or after diffusion phenomena through the bulk. Such steps are accompanied by the creation of highly activated and freshly renewed surfaces due to the milling process, corresponding to sites where CO_2 conversion can take place. Despite the

complexity of the process, which difficult defining reliably the different reaction steps, some hints can be obtained by analysing the experimental results, as described below.

In order to evaluate structural and microstructural changes of the olivine during mechanical activation, XRD analyses were performed (Fig. 4.3.4).
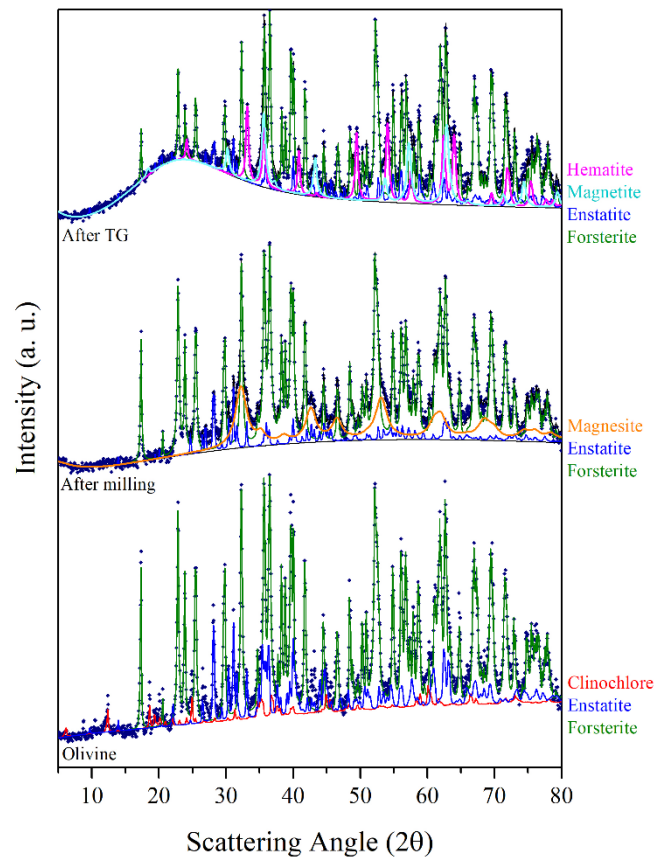

Figure 4.3.4: The CuKα XRD patterns sequence displays, from the bottom, the analyses of the Olivine in the as received state, the one of the sample at the end of 90 min of mechanical activation in the first series of runs, and the one further subjected to the thermogravimetric analysis. Experimental points are fitted by the Rietveld refinement procedure.

A decrease in the crystallite size of the predominant Forsterite phase due to the milling process was obtained by Rietveld refinement (Table 4.3.2). XRD patterns presented in Fig. 4.3.4 do not evidence the formation of a Serpentine phase. However, these patterns display, together with the residual Forsterite, the formation of two Mg-based phases, which can be identified as the trigonal

MgCO$_3$, Magnesite, s.g. R-3C, and the orthorhombic MgSiO$_3$, Enstatite, s.g. Pbca.

Milling time (min)	Forsterite crystallite size (nm)
0	230
30	92
90	85
180	82
240	76

Table 4.3.2: Crystallite size of the Forsterite phase, evaluated by Rietveld analysis of each sample, as a function of the milling time.

Such phases were observed in all the samples at the end of the mechanochemical trials, as displayed in Table 4.3.3. An example is the XRD pattern of the olivine subjected to 90 minutes of mechanochemical activation (central trace of Fig. 4.3.4). The data suggest that the transformation process of olivine was accompanied by CO$_2$ adsorption on the mineral surface, and further activation, which induces the formation of Magnesium carbonates phases. No Fe-based carbonates were detected. However, after heat treatment up to 1000°C of this as-activated olivine (upper trace of Fig. 4.3.4), the precipitation of two crystalline Fe-oxide phases, namely Hematite Fe$_2$O$_3$, s.g. R-3C, and Magnetite Fe$_3$O$_4$, s.g. Fd-3m was observed.

Fig. 4.3.5 shows the TGA curves of the pristine olivine and the samples previously subject to different milling times. While for pristine olivine, did not display significant changes in weight, all the other TG curves are characterized by two weight loss phenomena, occurring within three main temperature ranges (20-100°C,100-400°C and 400-1000°C).
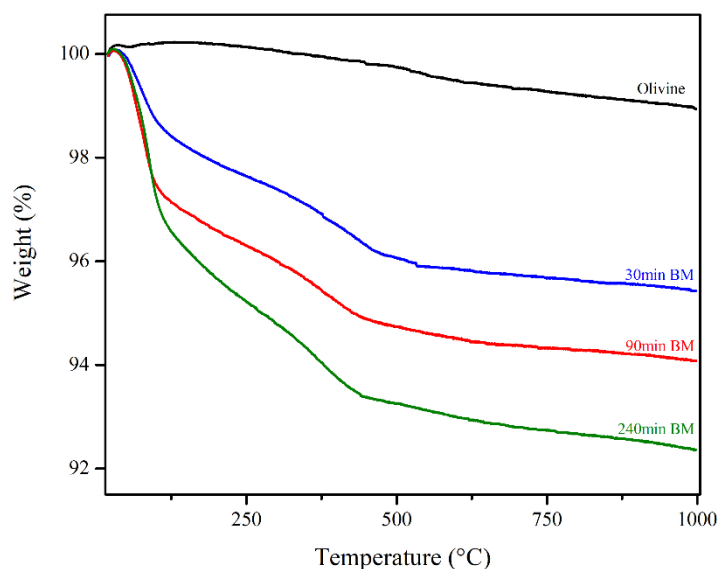
Figure 4.3.5: TGA traces carried out over selected samples at the end of the first series runs, i.e. mechanochemical tests carried out under a CO_2 pressure head equal to 1.5 bar.

The comparison with literature data suggests that the weight loss occurring at lower temperature ranges is related to H_2O desorption by the sample surface[3]; the subsequent signal, whose onset is observable at about 107°C can be related to the dehydration of the bulk; the last weight loss (around 450°C) can be conversely related to CO_2 evolution after decomposition of carbonate phases[4,5]. It can thus be argued that the heat treatment allowed H_2O and CO_2 evolution from these compounds, and that the decomposition of $MgCO_3$ (Magnesite) induced the increase of $MgSiO_3$ concentration (Enstatite) up to about 8%. The precipitation and grain growth of Hematite and Magnetite phases, whose relative amount are reported in Table 4.3.3, deserve further analysis.

Sample	Phases (Wt%)						
	Forsterite	*Clinochlore*	*Enstatite ferroan*	*Enstatite*	*Magnesite*	*Hematite*	*Magnetite*
Olivina AR	90.8 %	1.7%	7.5%				
30 min	79%			2.9%	18.1%		
After TG	82.9%			8.1%		5.9%	3.1%
90 min	85.1%			2.8%	12.1%		
After TG	80.1%			7.6%		7%	5.3%
180 min	80.6%			2.8%	16.6%		
After TG	78.6%			5.8%		8.9%	6.6%
240 min	79.9%			2.5%	17.6%		
After TG	77.1%			7.6%		11.6%	3.7%

Table 4.3.3: Phase composition, as evaluated by Rietveld analysis, of different samples after selected time of mechanical treatment, in the first series of tests. Constant pressure of 1.5 bar of CO_2 (AR: as received; TG: thermogravimetric measurement up to 1000°C).

It is noteworthy that the above findings are in agreement with Klein et al.[6] and Jones et al.[7] who reported the treatment of olivine with H_2O and CO_2, under hydrothermal conditions, at low-temperature and in presence of an excess CO_3^{2-} ions. In that case Fe^{2+} ions were rapidly incorporated to form carbonates, silicates and hydroxides, rather than being oxidized to Fe^{3+}, and can also be included within the serpentine, thus not leading to the precipitation of appreciable amounts of Magnetite. According to this, it could be surmised that, in our tests, the Magnesite carbonate phase, that formed as a consequence of mechanical activation of olivine with H_2O and CO_2, is not a pure Mg^{2+} based phase, but includes Fe ions.

This is confirmed by crystallographic features: values of lattice parameters *a* and *c* of the R-3C carbonate phase, equal to 4,682 Å and 15,218 Å respectively, are consistent with a ca. equimolecular mixture of the two Fe- and Mg- carbonate phases whose corresponding lattice parameters are *a* = 4,686 Å, *c* = 15,383 Å, and *a* = 4,635 Å, *c* = 15,023 Å respectively.

The driving force of the serpentinization process lies in the oxidation of Fe^{2+} to Fe^{3+} that leads to the reduction of water and the formation of molecular hydrogen.

As a matter of fact, the whole analysis of gaseous mixture from the mechanochemical reactor at the end of tests, allowed to confirm the occurrence of a significant amount of gaseous H_2. This hydrogen appeared due to H_2O activation and dissociation, and it was made available, within the vial, as a consequence of its desorption from powders.
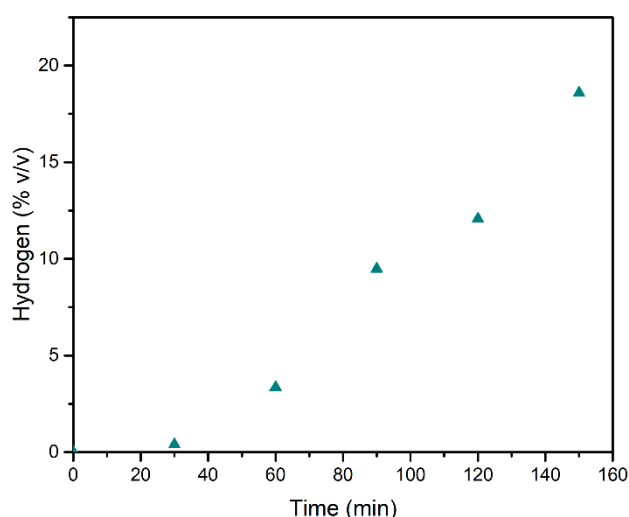
Figure 4.3.6: H_2 concentration in the gas phase within the mechanochemical reactor, as registered at different times of mechanical treatment, in the tests carried out with a pressure head of 1.5 bar of CO_2.

Its kinetic trend parallels the shape of CO_2 to CH_4 transformation (Fig. 4.3.6) and its value is relevant to samples mechanically treated up to 150 minutes, which show that the H_2 concentration rises up to about 20%v/v. Assuming 1atm pressure inside the vial, the amounts of H_2 detected are stoichiometrically possible (54% of the theoretical maximum) based on the available Fe^{2+} amount.

The CO_2 conversion (Fig. 4.3.7) shows that the kinetic trend recalls that observed for H_2: the increasing rate has to be considered as the initial step of a sigmoid-shaped curve, while the observed conversion values indicate, on one hand, the efficiency of the mechanochemical process as a tool for CO_2 storage, and, on the other hand, confirm that CO_2 absorption and activation steps are necessary conditions that precede the reduction to form methane.
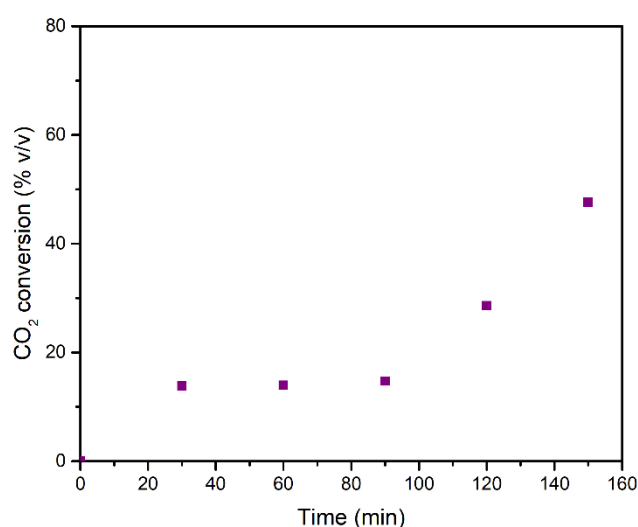

Figure 4.3.7: Conversion data of CO_2, plotted as a function of milling time, as observed during the series of mechanochemical tests performed with a pressure head of 1.5 bar of CO_2.

In order to evaluate the effect of the CO_2 pressure, as registered within the milling vial, on the transformation path under mechanochemical activation, two subsequent series of tests were carried out by changing the value of the CO_2/H_2O ratio by setting the CO_2 initial pressure of the vial at 1.5 bar and at 1.0 bar, respectively.

The CH_4 concentration values reported in Fig.4.3.8, correspond to the above series of experiments. It emerged that CO_2 conversion trend, as well as the H_2 evolution, approach the results of formerly presented runs at corresponding

times of mechanical treatment. The data of the two series have similar trends and are in the same order of magnitude, with a small increase observed in the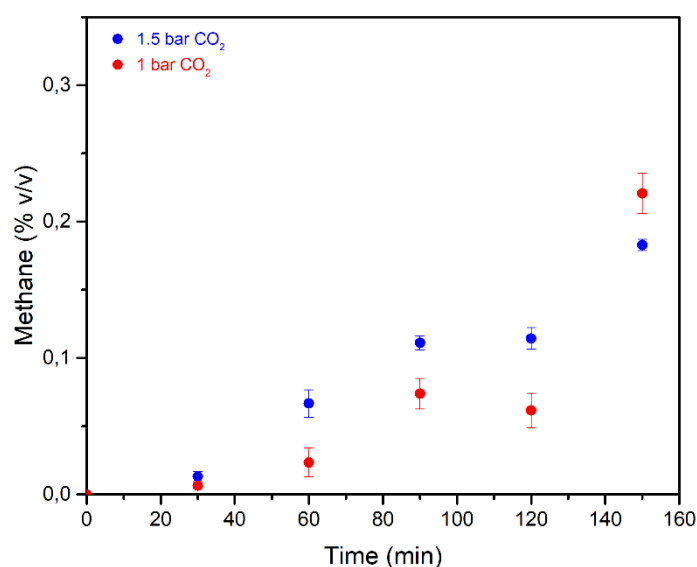 tests carried out at an initial pressure equal to 1.5 bar. The data of the two series have similar trends and are in the same order of magnitude, with a small increase observed in the tests carried out at an initial pressure equal to 1.5 bar.

Figure 4.3.8: Methane concentration data relevant to the three different test series. Blue dots: initial CO2 pressure equal to 1.5 bar. Red dots: initial CO$_2$ pressure equal to 1.0 bar. The data are replicates of two runs and error bars refers to standard deviation values.

For samples milled for 120 minutes, the lower conversion value marks a difference in the rising trend, and it parallels the corresponding data for H$_2$ evolution at the same time of treatment. Although the amount of gaseous H$_2$ available within the vial remains much higher than the stoichiometric requirement for the hydrogenation process, the dependence of the conversion on the H$_2$/CO$_2$ ratio may be a relevant factor.

As for the solid phases, a difference in the evolution of the phases was evidenced by XRD data (Table 4.3.3), which refer to the first series of tests

performed under an initial CO_2 pressure value equal to 1 bar. These results revealed the formation of the hydrated Mg-carbonate phase, the monoclinic $Mg(CO_3)*3H_2O$, Nesquehonite, s.g. P21, while no relevant signals of Magnesite carbonate were observed. The same finding was observed in the second series of tests (carried out at initial CO_2 pressure of 1 bar) in all the samples except for the one milled for 150 minutes, and it is consistent with the reduced value of the CO_2/H_2O ratio (Table 4.3.4). This suggests the sensibility of the chemical transformation to the adopted conditions. In this regard, it is interesting to note that our findings agree with the literature data, referred to the process in a liquid medium, which indicate that the precipitation of Magnesite at room temperature is not observed, despite being the stable carbonate form. Most commonly, only the Nesquehonite mineral can precipitate from aqueous solution at 25°C and with a partial pressure of CO_2 close to ambient pressure. At higher temperatures, above 40°C, several basic carbonates were observed to precipitate, in the form of hydromagnesite. Conversely, Magnesite production takes place only if the temperature is around 60-100°, and at high CO_2 pressure[8-12]. A further point deserves a comment: the Clinochlore phase, observed in the above tests, was present in a low amount (about 1.7wt.%) in the as-received Olivine and it was not found in the first series of experiments, where the mixed carbonate, Magnesite-type, was recovered. However, its content increased in the other series, where hydrated Nesquehonite compound was formed. In other words, during the process, decreasing the CO_2/H_2O ratio, the concentration of the resulting carbonate form decreases, and, under such conditions, the formed carbonate phase is hydrated. Then, the absence in XRD data of the signals related to the Serpentine, at the end of the mechanochemical runs, could be related to a possible phase amorphization during the process. A further possible interpretation is the occurrence of a consecutive process. The former step is

related to olivine hydrolysis, with the induced formation of Serpentine minerals, which still evolve, in the latter step, to give carbonates when CO_2 is available in the proper amount. Otherwise, in the tests carried out with a lower value of CO_2/H_2O ratio, the kinetics of the latter step slows down, allowing to observe the rise of the Clinochlore phase concentration.

Sample	Phases (Wt%)							
	Forsterite	*Clinochlore*	*Enstatite ferroan*	*Enstatite*	*Magnesite*	*Nesquehonite*	*Hematite*	*Magnetite*
Olivina AR	90.8%	1.7%	7.5%					
30 min	89.8%	2%		8.2%				
After TG	86.6%			8.1%			4.3%	1%
60 min	84.1%	2.8%		9.5%		3.7%		
After TG	83.9%			6.5%			7.1%	2.5%
90 min	84.4%	3.8%		6.8%		5.5%		
After TG	84.2%			6.4%			6.6%	2.7%
120 min	86.5%	3.8%		3.1%		6.6%		
After TG	83.2%			5.6%			8.6%	2.6%
150 min	83.6%			2.9%	13.5%			
After TG	80.2%			5.2%			11.9%	2.7%

Table 4.3.4: Phase composition, as evaluated by Rietveld analysis, of different samples after selected time of mechanical treatment, in the second series of tests, run under the initial CO2 pressure of 1 bar.

Finally, it is noteworthy that Magnetite, reported as the active catalytic phase in situ generated during FTT after olivine hydrolysis under hydrothermal conditions[7,11], was not observed during our mechanochemical runs, but only after thermal annealing at TGA. However, it is safe to say that, under mechanochemical activation, a necessary condition for the occurrence of FTT after olivine weathering process, is the presence of Fe^{3+} ions more than actual Magnetite particles.

The observed concentration values of methane and hydrocarbons may be influenced by the experimental set up: the analyses of the effects of parameters

like the geometry reactor, as well as the milling dynamic parameter, i.e. frequency of collision, will be the focus of future work aimed at improving chemical results and deepening the knowledge of the whole process.

4.3.3 References

[1]   F. Delogu et al. (2004). Mechanical work and conversion degree in mechanically induced processes. *Mater. Sci. Eng. A* **382**, 280–287.

[2]   P. M. Ahmedabadi , Kain V. (2019). Modelling transformation kinetics of different solid-state reactions using sigmoidal model. *Materialia* **5**, 100235.

[3]   M. M. Maroto-Valer et al. (2005). Activation of magnesium rich minerals as carbonation feedstock materials for CO_2 sequestration. *Fuel Process. Technol.* **86**, 1627–1645.

[4]   R. Bisbal et al. (2015). Evaluación de las características y propiedades de fundición de Arena de Olivino Venezolana (Parte I). *Rev. la Fac. Ing. Univ. Cent. Venez.* **30**, 95–110.

[5]   S. Stopic et al.(2018). Synthesis of magnesium carbonate via carbonation under high pressure in an autoclave. *Metals* **8**, 993.

[6]   F. Klein et al.(2014). Magnetite in seafloor serpentinite-Some like it hot. *Geology* **42**, 135–138.

[7]   L. C. Jones et al. (2010). Carbonate control of H_2 and CH_4 production in serpentinization systems at elevated P-Ts . *Geophys. Res. Lett.* **37**, L14306.

[8]   P. Zhang et al. (2000). Kinetics and Mechanisms of Formation of Magnesite from in Brine Hydromagnesite. *Appl. Geochemistry* **286**, 1748–1753.

[9]   A. I. Fernández et al. (2000). Procedure to obtain hydromagnesite from a MgO-containing residue. Kinetic study. *Ind. Eng. Chem. Res.*39, 3653–3658.

[10]   J. T. Kloprogge et al. (2003). Low Temperature Synthesis and Characterisation of nesquehonite. *J. Mater. Sci. Letters* **22**. 11, 825-829.

[11]   D. E. Giammar et al. (2005). Forsterite dissolution and magnesite precipitation at conditions relevant for deep saline aquifer storage and sequestration of carbon dioxide. *Chem. Geol.* **217**, 257-276.

[12]   M. Hänchen et al. (2008). Precipitation in the Mg-carbonate system-effects of temperature and CO_2 pressure. *Chem. Eng. Sci.* **63**, 1012–1028.

4.4 TEXTURAL PROPERTIES

Specific surface area (m²/g) and pore volume (cm³/g) of the samples are listed in Table 4.4.1, which shows the variation of the morphology at increasing milling times.

Milling time	Surface area (m²/g)	Pore volume (cm³/g)
0	1,19	0,0410
60	6,50	0,0715
90	28,80	0,0765
120	40,64	0,0787
180	75,20	0,1074
240	87,85	0,1031

Table 4.4.1: textural properties of the samples.

The low surface area value of the pristine olivine is in agreement with literature data[1,2]. The mechanical treatment allowed an increase of such parameter, initially small, up to 60 min of ball milling, and which became noticeable for prolonged milling times (Fig. 4.4.1).
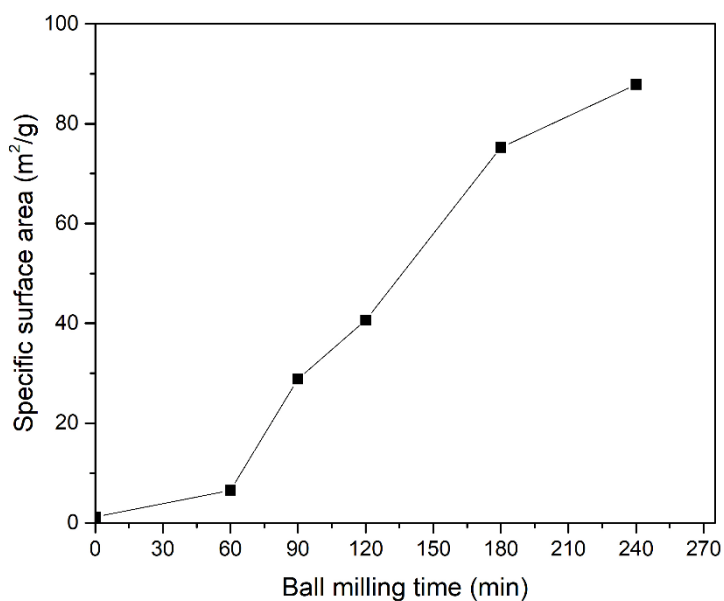
Figure 4.4.1: BET specific surface area plotted versus the milling time.

The pores volume showed an asymptotic trend up to 120 min, followed by an increase, reaching the maximum value at 180 min of milling (Fig. 4.4.2)
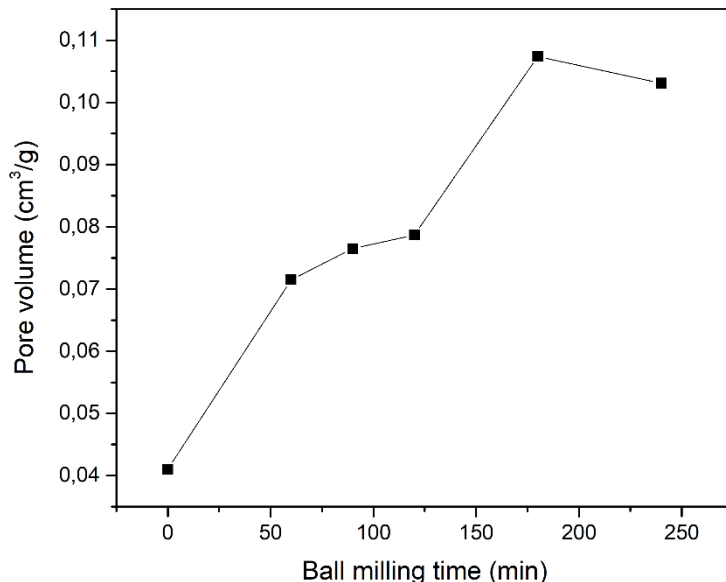
Figure 4.4.2: BET pore volume plotted versus the ball milling time.

The texture characterization proved the efficiency of the mechanical treatment, as demonstrated by the increasing value of surface area and pore volume. These trends are supported by the crystallite size of the main phase Forsterite (Tab. 4.3.2 previous paragraph) obtained by Rietveld refinement. The decrease in crystallite dimensions evidenced the formation of more uniform particles compared to the pristine olivine. So, the enhanced activity at increasing milling times may be related to the increased reactivity of the sample surface, that can play a catalytic role for the conversion process.

4.5 SPECTROSCOPIC INVESTIGATIONS

4.5.1 INTRODUCTION

One of the main difficulties encountered studying the mechanochemical activation of olivine in the presence of water and CO_2 was the inability to demonstrate that the CO_2 conversion to hydrocarbons was favoured by the oxidation of Fe^{II} contained in pristine olivine. As mentioned in the previous paragraphs, in fact, through XRD characterization it was not possible to highlight the formation and evolution of new phases containing Fe^{III} immediately after the mechanochemical runs, but only after heat treatment of the powders up to 1000°C by TGA analysis. Also the presence of Fe-based carbonates in the samples needed to be confirmed in order to better understand the reaction mechanism. For these purposes, we decided to deepen the characterization of our samples, carrying out ^{57}Fe Mössabuer and Raman spectroscopy measurements.

4.5.2 RAMAN ANALYSIS

All the samples were analyzed using a blue diode laser (D473, $\lambda \approx 473$ nm) with a scan time of 120-240 s. Given the small size of the Raman probe (about 5 μm), spectra of the studied samples were collected twice in different areas to identify any inhomogeneity. Experimental data were analyzed comparing peaks of mineral standards from the RRUFF database, using the program Crystal Sleuth[3,4].

As mentioned in Chapter 2, Olivine minerals have the general formula [M(1)M(2)SiO$_4$], where M = Fe^{2+}, Mg^{2+} and Mn^{2+}. Because of its small unit cell and relatively simple structure, many vibrational spectroscopic studies were carried out on Olivine. The quality of the Raman spectra has been continuously improved since 1991 when Chopelas[5,6] presented new vibrational mode assignments. The Olivine used in this study consisting of a solid solution of Forsterite (Fo), Mg$_2$SiO$_4$, and Fayalite (Fa), Fe$_2$SiO$_4$, with a composition of approximately Fo$_{90}$Fa$_{10}$. The experimentally measured wavenumbers and wavenumber shifts for pristine Olivine (Fig. 4.5.1) have been compared with those reported in literature[7]. All the observed Raman shift have values close to those typical of Forsterite, which is not unexpected given the high content of Mg in the material.
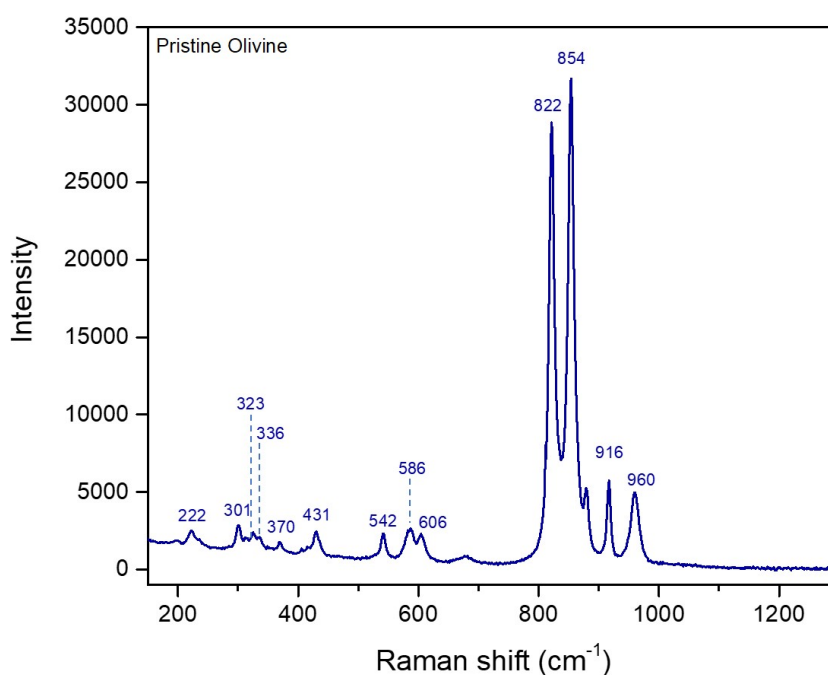
Figure 4.5.1: Raman powder spectra of pristine Olivine (Fo$_{90}$Fa$_{10}$).

The band at 222 cm^{-1} is related to the translation modes of (SiO$_4$) and M2 site. The bands in the region between 301 and 370 cm^{-1} are assigned to the vibration

modes of (SiO₄) and M2 site. From 431 to 606 cm⁻¹ there are the bands consisting of SiO₂ bending and, finally, from 822 to 960 cm⁻¹ those of SiO₂ stretching.

Figure 4.5.2 shows the comparison between the Raman spectra of all the samples and the known standards (RRUFF database).
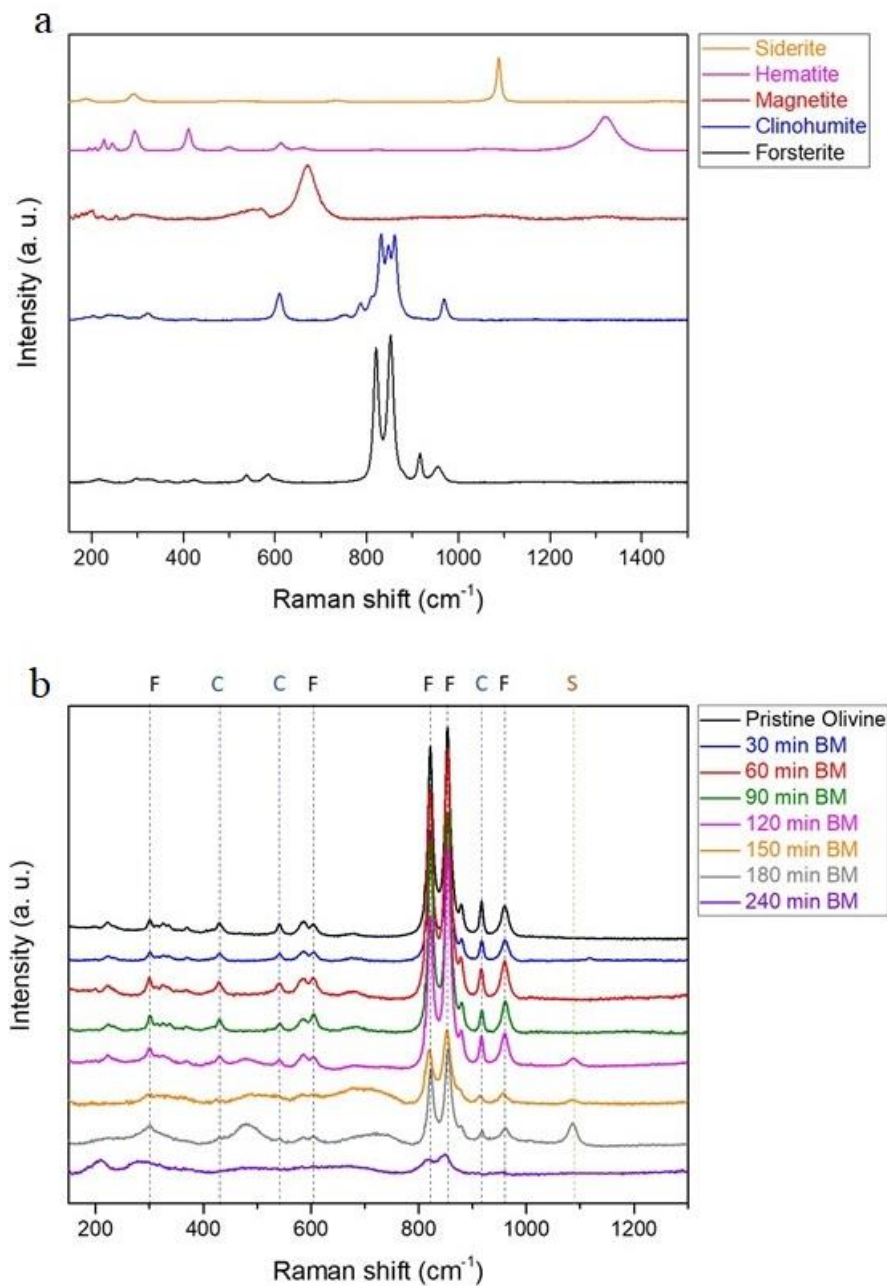

Figure 4.5.2: a) Raman spectra of know standards; b) Raman spectra one each time of milling explored. Notes: F = Forsterite, C = clinohumite, S = Siderite.

The dominating phase for all the samples was Forsterite. In some samples was possible to find the presence of Clinohumite, $[(Mg,Fe)_9(SiO_4)_4(OH)_2]$ whose main bands, easily detectable from those of Forsterite, are at 323, 610 and 970 cm^{-1}. The presence of this phase is due to the addition of water before the mechanical activation. At increasing milling times the mineralogy showed significant changes: in fact, starting from the sample milled for 120 min, the Raman spectra show the bands at 300, 480 and 710 cm^{-1} probably related to the presence of hill-defined Fe^{3+} oxides, as a consequence of the mechanical process (Fig. 4.5.3). In this region of the Raman spectra, appear the bands typical of iron (III) oxides. In some samples, also the presence of some Siderite, a Fe-based carbonate, could be detected, because of the presence of the typical band at 1088 cm^{-1}.
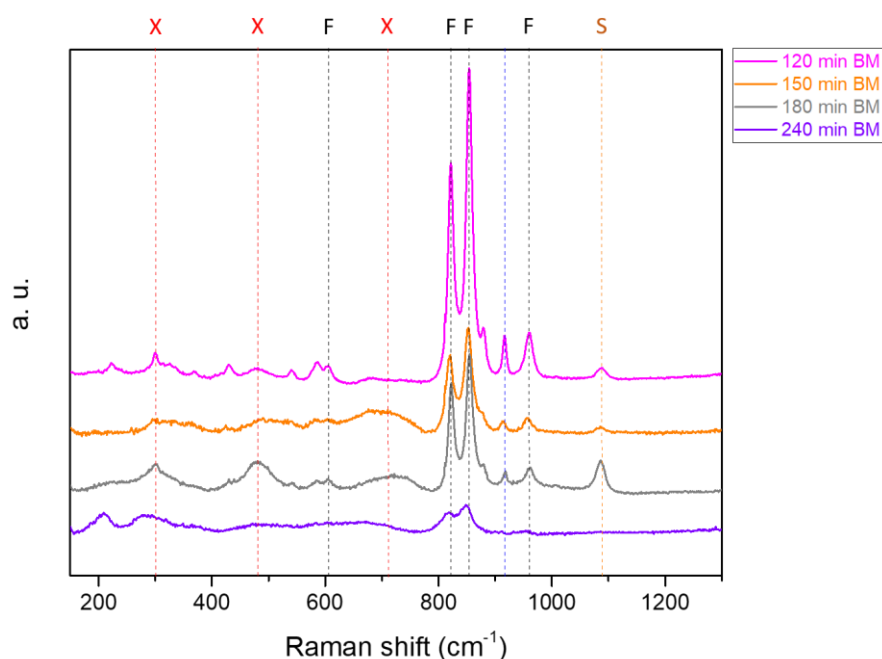
Figure 4.5.3: Zoom of Fig 4.5.2: here reported the Raman spectra of the samples milled 120 min to 240 min. Notes: F = Forsterite, X = hill-defined Fe (III) oxides, S = Siderite.

Figure 4.5.4 shows the comparison between pristine olivine and the sample milled for 150 min, before and after heat treatment at 1000°C in Ar atmosphere.
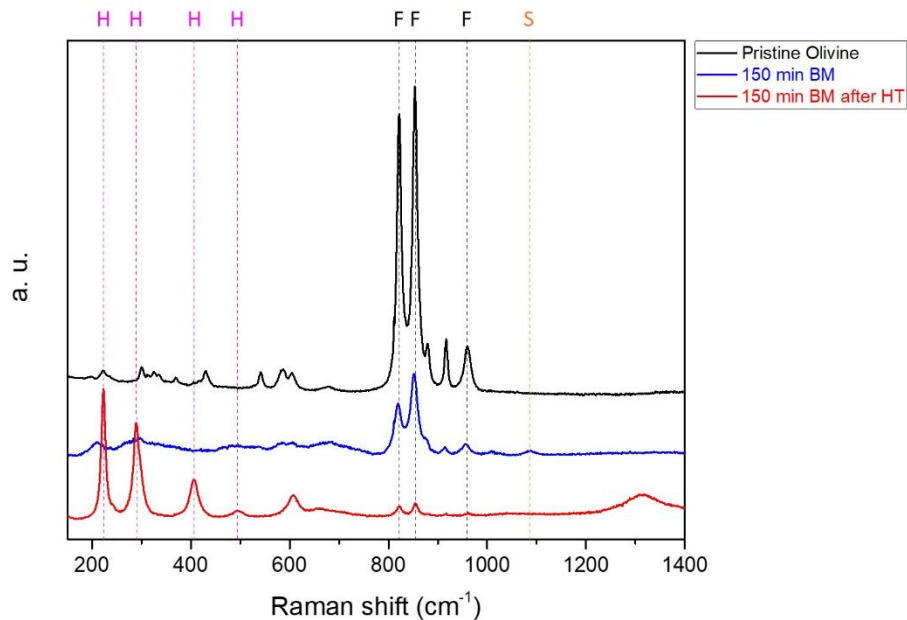

Figure 4.5.4: Comparison between the Raman spectra of Pristine Olivine and the sample milled for 150 min, before and after the heat treatment. Notes: F = Forsterite, H = Hematite, S = Siderite.

We decided to carry out the heat treatment in order to observe significant weight losses due to the CO_2 evolution after decomposition of the carbonate phases. The weight loss was rather limited, but the heat treatment favoured the precipitation and grain growth of Hematite, already detected by XRD (Tab. 4.3.4 previous paragraph). It is possible to observe, in the Raman spectra, the decreasing intensity of the most intense Forsterite bands at 824 and 856 cm^{-1}, especially after the heat treatment, whereas Hematite becomes the dominant phase. Comparing the Raman results with the phase composition data obtained by XRD (Table 4.5.1), it is possible to highlight the occurring of Fe^{II} oxidation through a *Serpentinization-like* process. The Clinochlore phase determined by XRD and related to the hydrated Olivine, due to the presence of water during

the milling process, was detected by Raman on the surface as Clinohumite. This last, in fact, corresponds to the hydrated form of magnesium and iron silicate. Furthermore, as shown by Raman spectra and summarized in Table 4.5.1, at prolonged milling times the appearance of typical Fe^{3+} oxides bands was observed. These Fe^{III} containing species, therefore, were formed immediately after the end of the mechanical activation, and they could be detected by Raman spectroscopy because the latter is eminently sensitive to the surface, unlike the XRD which is a bulk analysis technique. These results were also confirmed and supported by Mössbauer measurements, as it will be shown in the following paragraph.

Sample	Experimental conditions	XRD	Raman
Pristine Olivine	-	Forsterite, Clinochlore, Enstatite ferroan	Forsterite, Clinohumite
1	Milled for 30 min, 1.5 bar CO_2	Forsterite, Clinochlore, Enstatite	Forsterite, Clinohumite
2	Milled for 60 min, 1.5 bar CO_2	Forsterite, Clinochlore, Enstatite, Nesquehonite	Forsterite, Clinohumite
3	Milled for 90 min, 1.5 bar CO_2	Forsterite, Clinochlore, Enstatite, Nesquehonite	Forsterite, Clinohumite
4	Milled for 120 min, 1.5 bar CO_2	Forsterite, Clinochlore, Enstatite, Nesquehonite	Forsterite, Clinohumite, Magnetite, Siderite
5	Milled for 150 min, 1.5 bar CO_2	Forsterite, Enstatite, Magnesite	Forsterite, Clinohumite, Fe(III) oxide, Siderite
6	Milled for 180 min, 1.5 bar CO_2	Forsterite, Enstatite, Magnesite	Forsterite, Fe (III) oxides
7	Milled for 240 min, 1.5 bar CO_2	Forsterite, Enstatite, Magnesite	Forsterite, Fe (III) oxides
3_Air	Milled for 90 min, Air atmosphere	Forsterite, Clinochlore, Enstatite	Forsterite, Clinohumite
3_Argon	Milled for 90 min, Ar atmosphere	Forsterite, Clinochlore, Enstatite	Forsterite, Clinohumite
5b	Heat treatment at 1000°C in Ar atmosphere, after 150 min of milling	Forsterite, Enstatite, Magnetite, Hematite	Forsterite, Hematite

Table 4.5.1: summary of the mineralogy results obtained through XRD and Raman spectroscopy.

4.5.3 MÖSSBAUER ANALYSIS

[57]Fe Mössbauer spectra were measured at ambient temperature and for specific samples at the temperature of 5K. A source of [57]Co:Rh, always kept at room temperature, was used, and run times ranged from 24 to 48 hours. Isomer shifts are calibrated against an α-Fe metal foil. Spectra were fitted with appropriate combinations of Lorentzian line shapes using the PC-Mos II computer program[8]. In this way, typical hyperfine parameters such as the isomer shift (IS), the electric quadrupole splitting (QS), the linewidth at half maximum (LW) and the relative absorption area of the different components were determined.

Olivine is a nesosilicate which structure consists of oxygen ligand each bonded to only one silicon atom, forming isolated SiO_4 tetrahedra. This leads to the formation of two non-equivalent octahedrally coordinated metallic sites in the olivine structure, in which are located the divalent Mg and Fe cations. These differences would lead to a cationic site preference as a function of temperature and/or the ratio of the cation concentration, as reported in literature[9-11]. The Mössbauer spectra of pristine Olivine, used in this work, shows an asymmetric quadrupole doublet (Fig. 4.5.5). At least three independent spectral components are necessary to fit this doublet. Comparing the experimental values of isomer shift, IS, and quadrupole splitting, QS, (Tab. 4.5.2) with those reported in literature[12-16], it emerged that the two doublets with high intensities (red and blue lines in Fig. 4.5.5) belong to Fe^{2+} at M1 and M2 sites, respectively, confirming that also in this case, there is no cationic site preference for the iron ions. The third minor doublet, represented by the green line, is characteristic of Fe^{2+} in the octahedral ionic site of pyroxene $[(Mg,Fe)Si_2O_6]$[8,13].

As mentioned in the previous paragraph, the olivine used is constituted by the following phases: Forsterite ($Fe_{0.2}Mg_{1.8}SiO_4$), 90.8 wt.%; Enstatite ferroan

($Fe_{0.2}Mg_{0.8}SiO_3$), 7.5 wt.%; and Clinochlore ($Al_{1.84}Fe_{0.5}H_8Mg_{4.5}O_{18}Si_{3.16}$), 1.7 wt.%. Therefore, the Mössbauer results confirm the composition previously determined by XRD analysis.
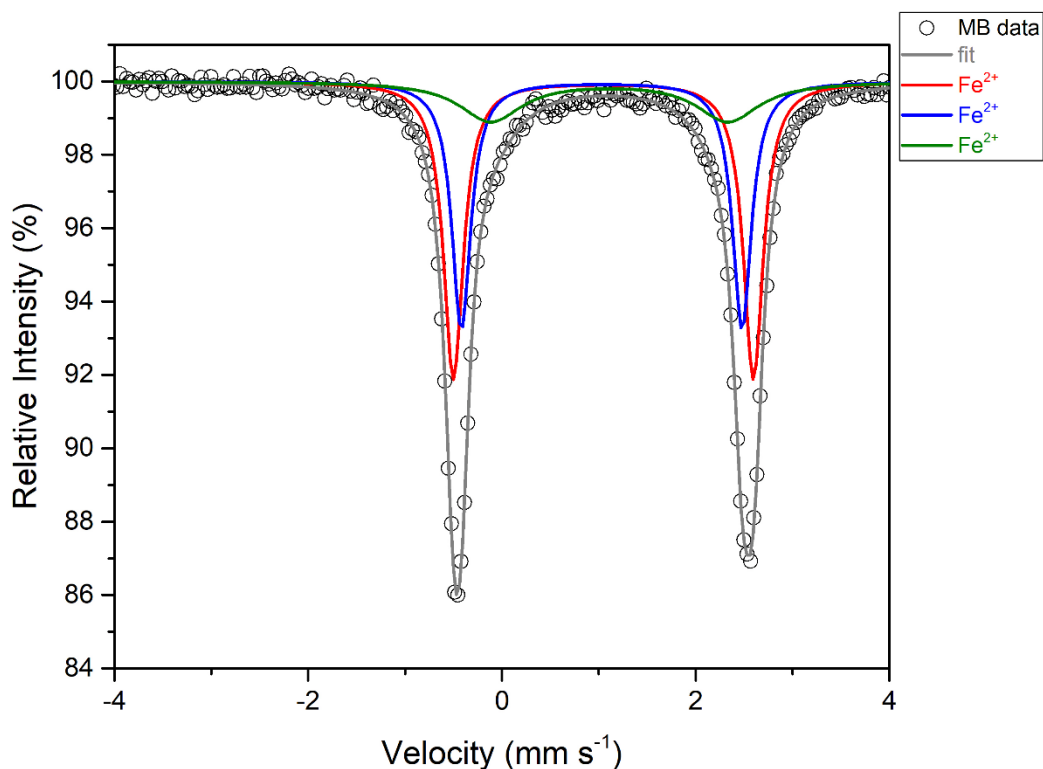

Figure 4.5.5: room temperature Mössbauer spectra of pristine Olivine.

In order to verify the evolution of the oxidation state of the iron sites at increasing milling time, Mössbauer spectra were measured after increasing milling times and compared to that of pristine olivine (Figure 4.5.6).
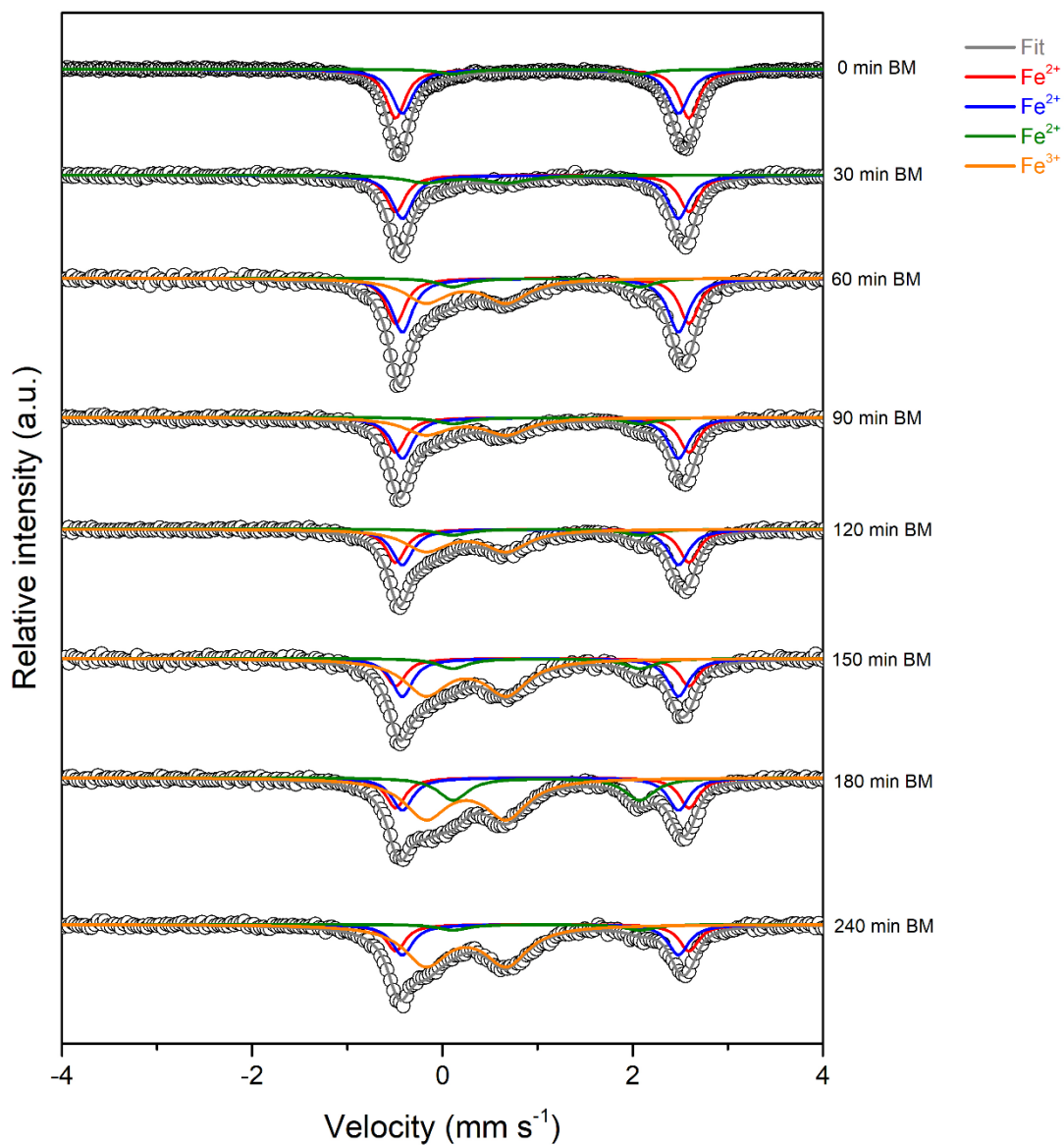
Figure 4.5.6: Mössbauer spectra measured at room temperature of all the samples, plotted for increasing milling time.

Table 4.5.2 summarizes the hyperfine parameters of the four quadrupole doublets that were necessary to fit simultaneously the series of collected spectra.

	QS (mms^{-1})	IS (mms^{-1})	LW (mms^{-1})	Fe type
Olivine Site M1	3.08 ± 0.01	1.15 ± 0.00	0.25 ± 0.01	Fe^{2+}
Olivine Site M2	2.90 ± 0.01	1.13 ± 0.00	0.24 ± 0.01	Fe^{2+}
Pyroxene (Mg,Fe)Si$_2$O$_6$	1.96 ± 0.01	1.19 ± 0.00	0.38 ± 0.01	Fe^{2+}
Fe (III) oxides	0.85 ± 0.01	0.35 ± 0.00	0.54 ± 0.00	Fe^{3+}

Table 4.5.2: Mössbauer parameters for each component presented in Fig. 4.6.6.
Olivine site M1: red line; olivine site M2: blue line; pyroxene: green line; Fe III: orange line.

The additional doublet with hyperfine parameters typical of trivalent iron with hyperfine parameters in the range of iron oxides/hydroxides appears already after 30 min of milling, indicating that the oxidation of Fe^{II} to Fe^{III} occurs already after such a short time. The oxidation increases with increasing milling time, as confirmed by the increasing relative resonance area of the Fe^{3+} doublet (Fig. 4.5.7 and Table 4.5.3). These results allowed us to validate the preliminary hypothesis, according to which the hydrogen evolution during the CO$_2$ conversion to hydrocarbons, was the proof of the occurrence of a *Serpentinization-like* process. Moreover, the observed formation of Fe^{3+}, agree well with the observations of Raman spectroscopy (vide supra).

As the relative area of Fe^{3+} doublet increases, that of Fe^{2+} related to the olivine sites decreases, while the relative area of Fe^{2+} related to the pyroxene site remains almost constant up to 180 min, then it varies slightly, indicating a possible participation of this phase to the reaction. Hence, even though Fe^{II} is consumed during the process, at 240 min a small amount of it is still available, both as Fe^{II} in M1 and M2 sites of olivine and in pyroxene. In principle, therefore, CO$_2$ conversion to hydrocarbons might continue for prolonged milling times.

Milling time (min)	Olivine site M1	Olivine site M2	Pyroxene $(Mg,Fe)Si_2O_6$	Fe (III) oxides
	Relative Area (%)			
0	$0,47 \pm 0,03$	$0,46 \pm 0,05$	$0,07 \pm 0$	
30	$0,35 \pm 0,03$	$0,45 \pm 0,04$	$0,04 \pm 0,01$	$0,15 \pm 0,01$
60	$0,27 \pm 0,03$	$0,35 \pm 0,03$	$0,08 \pm 0,01$	$0,30 \pm 0,01$
90	$0,28 \pm 0,03$	$0,35 \pm 0,03$	$0,08 \pm 0,01$	$0,29 \pm 0,01$
120	$0,26 \pm 0,03$	$0,30 \pm 0,03$	$0,08 \pm 0,01$	$0,36 \pm 0,01$
150	$0,17 \pm 0,02$	$0,26 \pm 0,02$	$0,1 \pm 0,01$	$0,48 \pm 0,01$
180	$0,16 \pm 0,02$	$0,19 \pm 0,02$	$0,2 \pm 0,01$	$0,46 \pm 0,01$
240	$0,17 \pm 0,02$	$0,21 \pm 0,02$	$0,05 \pm 0,01$	$0,56 \pm 0,01$

Table 4.5.3: Summary of the relative area of each doublet plotted in Fig. 4.6.7.
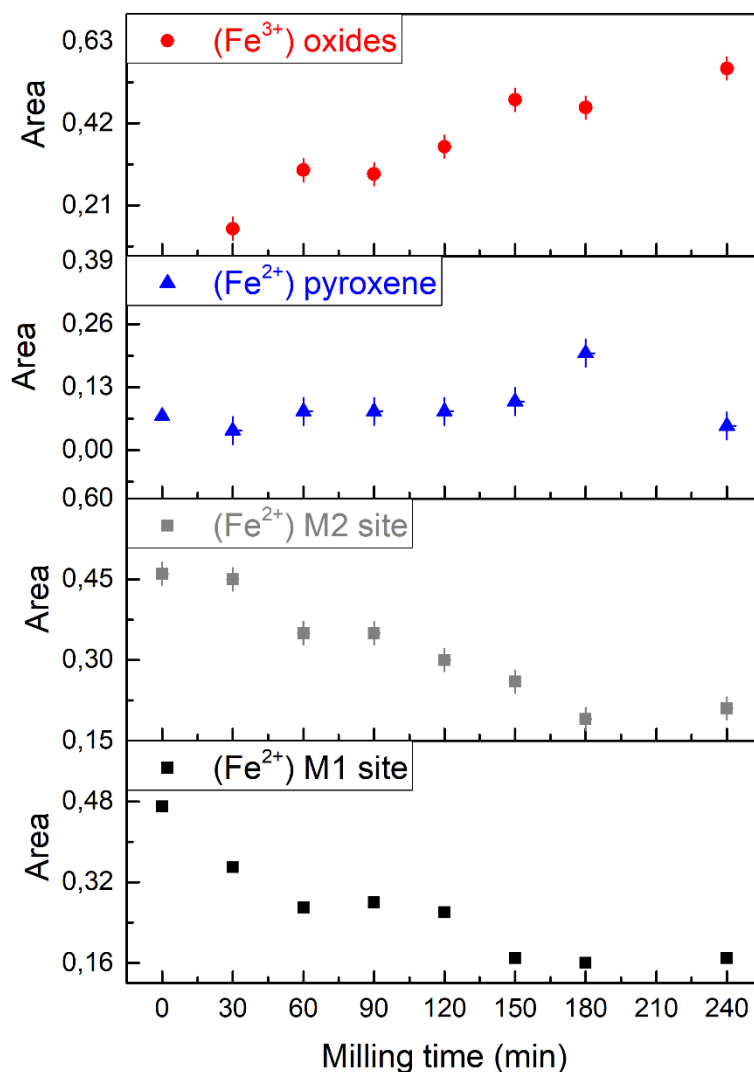
Figure 4.5.7: Relative area of each doublet for all the samples, plotted as a function of the milling time.

As for the Raman analysis, we made the comparison between pristine Olivine and the sample milled for 150 min, before and after the heat treatment in Ar atmosphere at 1000°C, also through the Mössbauer technique. It can be observed, from Figure 4.6.8, that after 150 min of milling the resulting doublets arise from Fe^{2+} of the two sites of olivine (M1: IS =1.15 mms^{-1}, QS = 3.08 mms^{-1}; M2: IS = 1.13 mms^{-1}, QS = 2.90 mms^{-1}), of the pyroxene site (IS = 1.19 mms^{-1} and QS = 1.96 mms^{-1}) and from Fe^{3+} oxides site (IS = 0.35 mms^{-1} and QS = 0.85 mms^{-1})[8,11-12]. Repeating the Mössbauer measurement after heating this sample up to 1000°C, the spectra include two new components that are magnetic sextets.
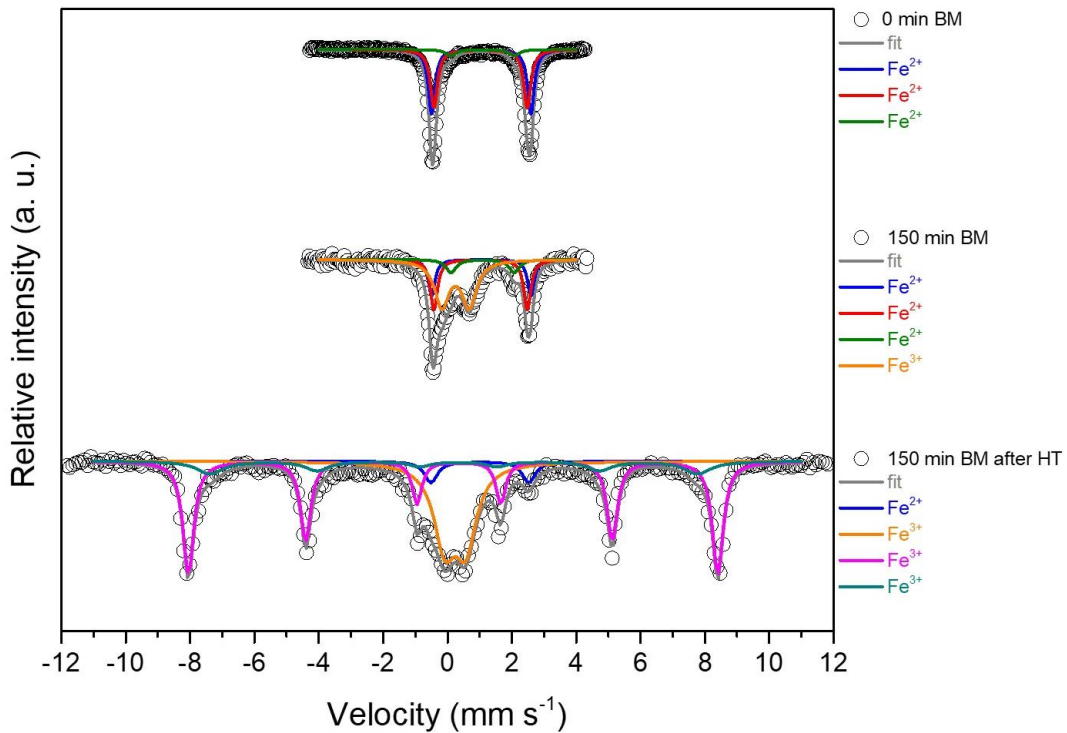
Figure 4.5.8: comparison between the Mössbauer spectra of the sample milled for 150 min, before and after the heat treatment.

The parameters of the first sextet (violet line), IS = 0.38 mms^{-1}, QS = -0.18 mms^{-1} and hyperfine field B = 51.01 T, are characteristic of crystalline Hematite at room temperature, Fe_2O_3[6]. The parameters of the second sextet (dark cyan line),

IS = 0.27 mms^{-1}, QS = -0.14 mms^{-1} and B = 46.98 T, could be related to not crystalline Hematite, which may contain Mg cations in the structure that decrease the magnetic hyperfine field value, or to Maghemite at room temperature. For this sample, we have observed by XRD (sample 5b, Tab. 4.5.1) the presence of Magnetite and Hematite phases, so we can conclude that the second sextet can reasonably be attributed to Maghemite. In order to better understand the evolution of the iron oxide species before the heat treatment, a Mössbauer spectrum of the sample milled for 150 min (before the heat treatment) was also recorded at 5 K (Fig. 4.5.9).
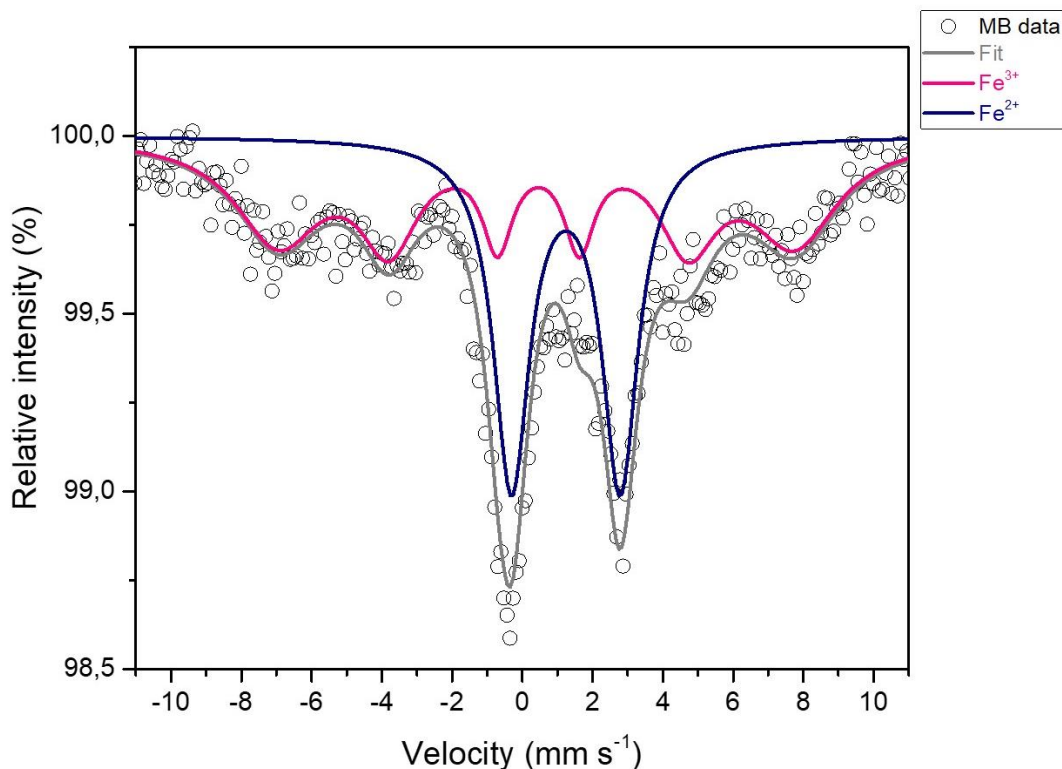
Figure 4.5.9: ^{57}Fe Mössbauer spectra recorded at 5K, of the sample milled for 150 min.

In this spectrum, in addition to the olivine doublets, which retain their shape, the Fe^{III} components is not anymore represented by a quadrupole doublet, but has transformed into a broadened magnetic sextet, with isomer shift and

121

quadrupole splitting of IS = 0.55 mms^{-1} and QS = - 0.13 mms^{-1}, respectively. Such modification of the spectrum at low temperature is characteristic of disordered or nanosized Fe^{III} oxides undergoing superparamagnetic relaxation, and thus showing magnetic order only below the so-called blocking temperature. This additional experiment confirms their formation already after the milling. The following heat treatment favours the grain growth and then the crystallization of these oxides so as to make them easily detectable through each characterization technique.

4.5.4 REFERENCES

[1]   P. Baláž et al. (2008). Structural changes in olivine (Mg, Fe)$_2$SiO$_4$ mechanically activated in high-energy mills. *Int. J. Miner. Process.* **88**, 1-6.

[2]   I. Rigopoulos et al. (2018). Effect of ball milling on the carbon sequestration efficiency of serpentinized peridotites. *Min. Engineering.* **120**, 66-74.

[3]   B. Lafuente et al. (2016). The power of databases: The RRUFF project. Highlights in Mineralogical Crystallography. 1-29.

[4]   J. Knafelc et al. (2019). The effect of oxidation on the mineralogy and magnetic properties of olivine. *American Mineralogist.* **104**, 694-702.

[5]   A. Chopelas (1990). Thermal properties of forsterite at mantle pressures derived from vibrational spectroscopy. *Phys. Chem. Minerals.* **17**, 149-156.

[6]   A. Chopelas (1991). Single crystal Raman spectra of forsterite, fayalite, and monticellite. *American Mineralogist.* **76**, 1101-1109.

[7]   B. A. Kolesov et al. (2004). A Raman spectroscopic study of Fe-Mg olivines. *Phys. Chem. Minerals.* **31**, 142-154.

[8]   G. Grosse (1993). PC-Mos II, Version 1.0 Manual and Program Documentation.

[9]   E. C. Sklute (2006). Mössbauer Spectroscopy of Synthetic Olivine across the Mg-Fe Solid Solution. B.A. thesis, Mount Holyoke College, South Hadley.

[10]   S. Chatterjee et al. (2009). Site preference of Fe atoms in FeMgSiO$_4$ and FeMg(SiO$_3$)$_2$ studied by density functional calculations. *Phys. Rev. B* **79**, 115103.

[11]   B. A. Kolesov et al. (1996). Raman spectra and cation distribution in the lattice of olivines. *Mat. Res. Bullettin* 31, 8, 1035-1044.

[12]   R. M. Cornell , Schwertmann U. (2000). The Iron Oxides – Structure, properties, reactions, occurrences and uses. 2nd Edition. Wiley VCH.

[13]   L. Stievano & F. E. Wagner (2012). Mössbauer Spectroscopy and magnetometry. Wiley-VCH.

[14]   R. V. Morris et al. (2004). Mineralogy at Gusev Crater from the Mössbauer spectrometer on the Spirit Rover. *Science.* **305**, 833-836.

[15]   D. Świerczyński et al. (2006). Oxidation reduction behaviour of iron-bearing olivines (Fe$_x$Mg$_{1-x}$)$_2$SiO$_4$ used as catalysts for biomass gasification. *Chem. Mater.* **18**, 897-905.

[16]   M. I. Oshtrakh et al. (2007). Determination of quadrupole splitting for [57]Fe in M1 and M2 sites of both olivine ad pyroxene in ordinary chondrites using Mössbauer spectroscopy with high-velocity resolution. *Hyperf. Interact.* **177**, 65-71.

4.6 INFLUENCE OF THE MILLING DYNAMIC PARAMETERS ON THE CO_2 CONVERSION KINETICS

It is well known that modulation of the vial motion frequency corresponds to different kinetic energy transferred at each impact by the collisions between balls and powders. Therefore, to carry out a deepen kinetic study of the conversion process, three series of tests were performed using 2 g of olivine, 0.3 ml of H_2O at initial pressure of 1.5 bar of CO_2, varying the rotation frequency of the mill engine, respectively at 745, 875 and 1000 rpm.

Table 4.6.1 summarize the operative condition for each series of tests.

Series	Olivine	Water	Ball milling time (min)
745 rpm	2 g	0,3 mL	30
			60
			90
			120
			150
875 rpm	2 g	0,3 mL	30
			60
			90
			120
			150
1000 rpm	2 g	0,3 mL	30
			60
			90
			120
			150

Table 4.6.1: operative condition parameters.

As shown in Figure 4.6.1, methane, ethane and ethylene were produced at each investigated frequency. The main hydrocarbon product is always methane.

In Fig. 4.6.1. the hydrocarbon evolution is plotted as a function of milling time for different vial motion frequency values. Graphs seem to suggest different trends depending on the operative conditions. In the test carried out at 745 rpm,

the kinetic data were characterised by an almost linear trend. At 875 rpm the amount of produced hydrocarbons initially smoothly rise, according to an almost-linear fit, then approaching an asymptotic value; similar behaviour characterised the experiments performed at 1000 rpm, in this case the maximum conversion values were observed in the samples milled 90 min, which was then followed by a reduction of the total hydrocarbons amounts at prolonged milling times.
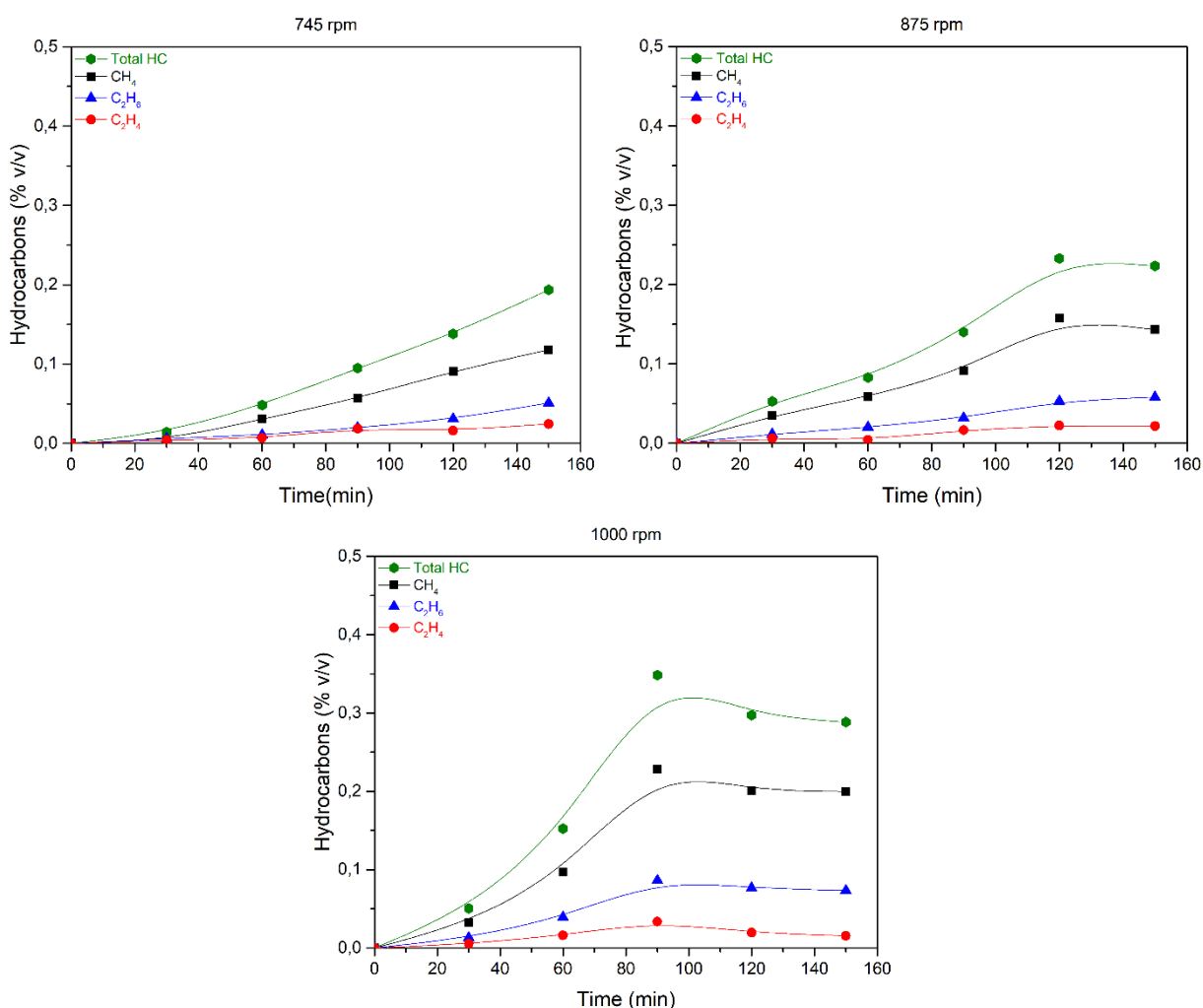

Figure 4.6.1: hydrocarbon evolution plotted versus the ball milling time for each investigated frequency.

It should be noticed that the variation in the milling vial rotation speed, respectively 745, 875 and 1000 rpm, affects the milling dynamics and influences

simultaneously two parameters, i.e. the collision frequency and the impact energy, which, in turn, play a key role in defining the process kinetics, mainly in the time scale. Then, it is probably safe to say that the apparent different behaviour is the result of the simultaneous variation of such parameters and is not the expression of different mechanisms underlying the three series of tests. More interesting is, however, focusing on methane kinetics evolution during the mechanical activation (Fig. 4.6.2 a): it can be seen that increasing the motion frequency, the maximum value is reached at decreasing milling times. In details, 150 min at 745, 120 min at 875 and 90 min at 1000 rpm. Comparing these results with the amount of hydrogen evolution during the process (Fig. 4.6.2 b), these last trend parallels the shape of the methane production for each series.

As a matter of fact, the driving force of the serpentinization process lies in the oxidation of Fe^{2+} to Fe^{3+} that leads to the reduction of water and the formation of molecular hydrogen.

The CO_2 conversion trend is slightly different, but the observed conversion values evidenced the efficiency of the process and suggest that the CO_2 adsorption, and subsequent absorption, is a necessary step to methane formation.
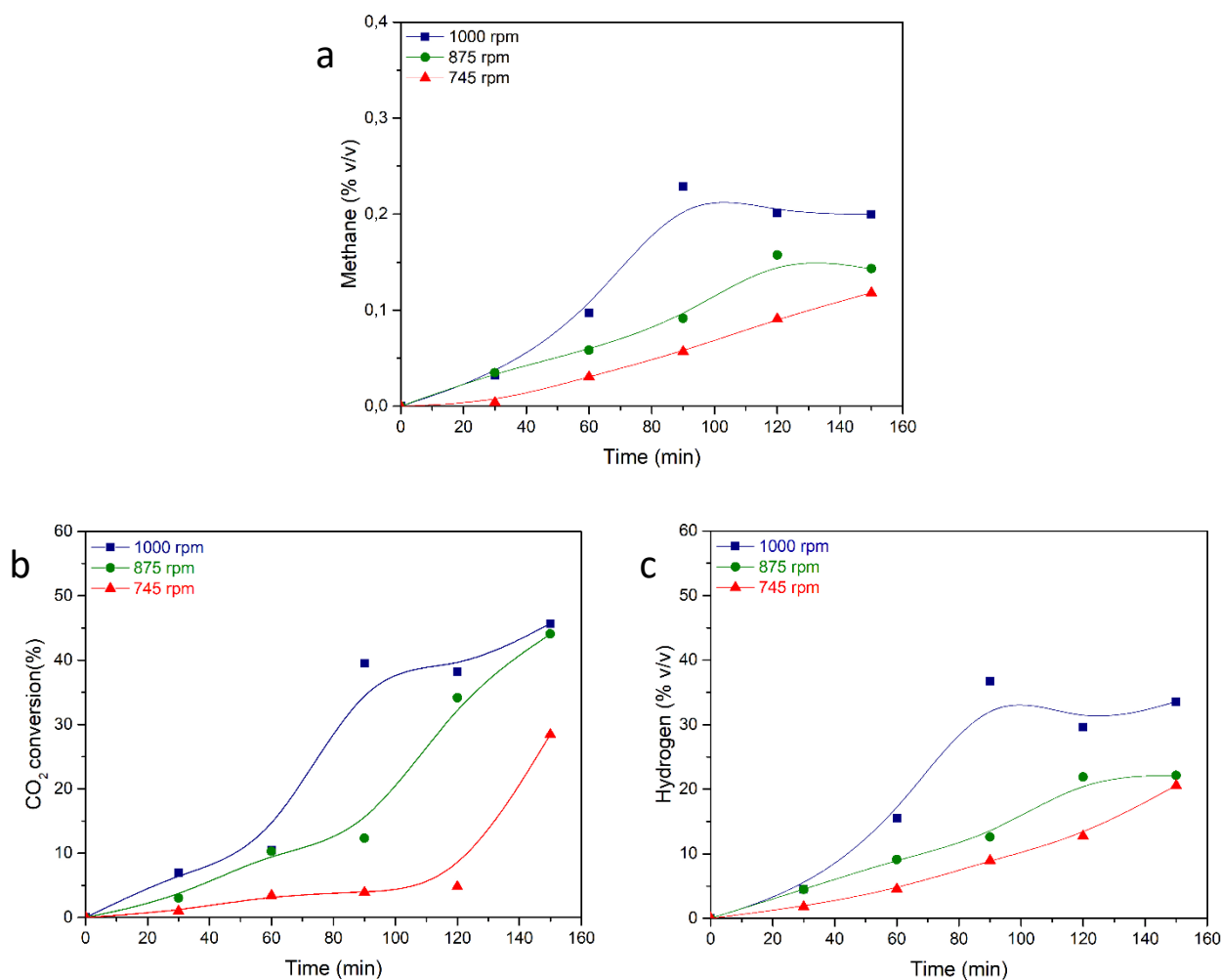
Figure 4.6.2: comparison between a) methane concentration values, b) hydrogen evolution, c) CO₂ conversion values, plotted as a function of the different vial motion frequency investigated.

As confirmed by XRD results, summarized in Table 4.6.2, the maximum amount of produced methane was observed in correspondence with the highest amount of Magnetite, carbonate phase, detected on the sample powders (evidenced in Tab. 4.6.3). In particular, at 745 rpm, at 150 min of milling were recorded the maximum CO_2 conversion value, the maximum amount of

produced methane and the maximum amount of detected Magnesite of the whole series. At 875 rpm, at 120 min of milling were observed the maximum amount of methane and Magnesite, while the highest value of CO_2 conversion has been reached at 150 min. Finally, at 1000 rpm, the highest values of CO_2 conversion were recorded at 90 and 150 min, and the maximum amount of methane and Magnesite at 90 min of milling.

Sample		Forsterite $Fe_{0.2}Mg_{1.8}SiO_4$	Clinochlore $Al_{1.84}Fe_{0.5}H_8Mg_{4.5}O_{18}Si_{3.16}$	Enstatite ferroan $Fe_{0.155}Mg_{0.845}SiO_3$	Nesquehonite $MgCO_3*3H_2O$	Magnesite $MgCO_3$
	0 min	91%	2%	7%	-	-
745 rpm	30 min	88%	5%	5%	2%	-
	90 min	84%	7%	1%	2%	6%
	150 min	79%	3%	4%	1%	13%
875 rpm	30 min	86%	5%	3%	2%	4%
	90 min	85%	4%	3%	1%	5%
	120 min	77%	4%	2%	-	17%
	150 min	76%	3%	4%	-	17%
1000 rpm	30 min	77%	9%	3%	1%	10%
	90 min	77%	-	2%	-	30%
	150 min	76%	9%	1%	1%	13 %

Table 4.6.2: phase composition, determined by Rietveld analysis, of some selected samples of each test series.

Furthermore, the evolution of the solid phases revealed the decrease of weight percentage of Forsterite and Enstatite ferroan, which contain the Fe^{2+} ions involved in the redox process, and the formation of the carbonate phases. As mentioned in paragraph 4.3, crystallographic data confirmed that the Magnesite phase is not a pure Mg^{2+} based phase, but includes Fe ions.

Sample	CO_2 conversion (% v/v)	Methane (% v/v)	Magnesite (wt. %)
90 min (1000 rpm)	40	0,2285	30
120 min (875 rpm)	34	0,1576	17
150 min (745 rpm)	28	0,11821	13

Table 4.6.3: best results of methane concentration, CO_2 conversion and Magnesite weight percentual values for each series of tests.

From these experimental observations, we can hypothesize that the formation of carbonate is not a competitive reaction with respect to the CO_2 conversion to hydrocarbons, but constitutes a necessary step of this reaction, catalysed by olivine. Therefore, we can presume the following reaction mechanism for the whole process (Fig. 4.6.3), as a gas-solid reaction that occurs on the mineral surface.

1° STEP: $2(Mg,Fe)_2SiO_4 + 4H_2O + 3CO_2 \rightarrow (Mg,Fe)Si_2O_5(OH)_4 + (Mg,Fe)CO_3 + 2H_2$

2° STEP: $2(Mg,Fe)Si_2O_5(OH)_4 + 4(Mg,Fe)CO_3 + 4H_2 \rightarrow (Mg,Fe)Si_2O_5(OH)_4 + (Mg,Fe)CO_3 + 2(Mg,Fe)_2SiO_4 + 3CH_4 + 5O_2$
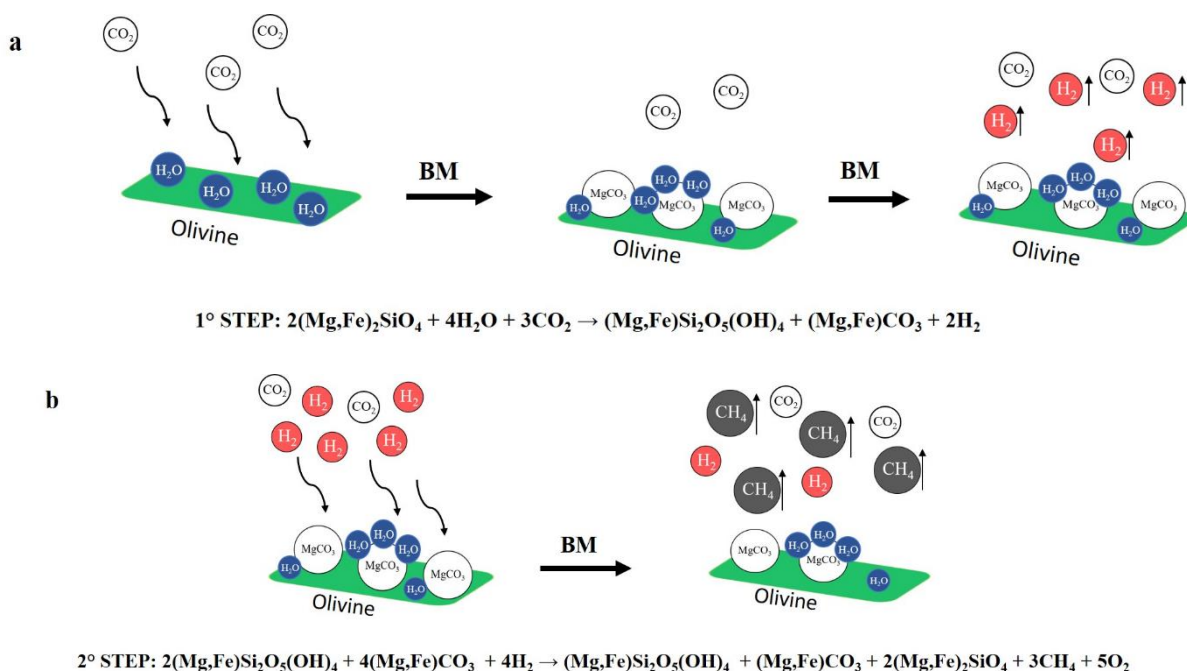
Figure 4.6.3: reaction mechanism hypothesized.

In the first step of the mechanochemical process, (Fig. 4.6.3 a) olivine powders react with water and carbon dioxide, leading to the formation of serpentine mineral, magnesium-iron carbonate and molecular hydrogen. In the following step (Fig. 4.6.3 b), the carbon dioxide already activated in the form of carbonates reacts with the molecular hydrogen to give methane (and light hydrocarbons). Then these latter are not produced by direct CO_2 hydrogenation. To be underlined, in the reaction related to the second step of the reaction, molecular hydrogen is indicated also as possible products, not only as a reagent. Such mechanism hypothesis seems to be confirmed by the formation of molecular oxygen, which was detected, on a qualitative basis, by the gas chromatographic analyses carried out along the process, and whose occurrence was required, among the products of the second step, by the reaction stoichiometry.

A further deepening on these specific mechanistic inferences is however needed and it will be the focus of further experimental work, at present under examination.

4.7 PLANETARY MILLING STRATEGY

In the second strategy of the work, we decided to modify some milling dynamic parameter, in order to verify how these could affect the whole process, the reaction mechanism in particular.

4.7.1 MATERIALS AND METHODS

Olivine powders were provided by SATEF-HA (Italy). The mechanical activation was carried out by a Fritsch Pulverisette 6 planetary mill, and the jar used as a mechanochemical reactor is shown in Fig. 4.7.1.

Figure 4.7.1: mechanochemical reactor adapted for planetary mill.

The mechanical treatments were carried out on fresh powders, using 2 g of olivine, 0.3 ml of deionized water at 500 rpm (ball to powder ratio = 47), at selected milling times (15, 30, 60, 90 and 120 minutes) and different CO_2 pressures: 0.25, 0.5 and 1 bar. In order to remove the residual air from the vial, vacuum was applied, before introducing CO_2. To obtain the selected pressure at 0.25 and 0.5 bar a mixture of Argon and CO_2, with a total pressure of 1 bar, was prepared (75% and 50% of Argon respectively). Additional tests were performed using 4 g of olivine and 0.6 ml of water, at the selected pressures of 0.5 and 1 bar of CO_2. Gas sampling was performed 30 min after stopping milling and the gases were analyzed by FTIR through a homemade gas cell equipped by two KBr windows (Fig. 4.7.2).
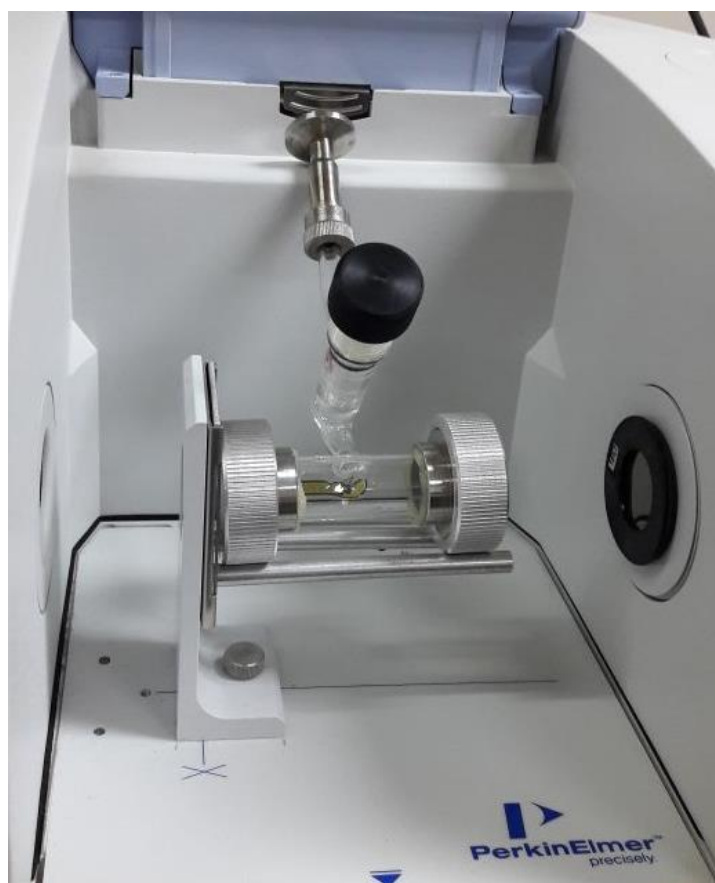
Figure 4.7.2: cell for FTIR analysis of gas mixtures.

All the mechanochemical processes were conducted under low pressure of CO_2, in order to reproduce the reaction conditions expected under a real environment.

Samples have been indicated as VN_{x-y}, where x is related to the CO_2 operative pressure and y to the milling time.

Gas mixture analyses were performed by Perkin Elmer FT-IR Spectrometer, equipped with a MCT (mercury-cadmium-tellurium) detector, after the connection to the jar, through the expansion of the mixture to the gas cell, where vacuum was previously applied. Quantitative analyses were carried out through the construction of calibration curves.

The structural characterization of the powders was realized by X-ray diffraction, FT-IR spectroscopy, carried out on samples in tablet form diluited with KBr, and scanning electron microscopy (SEM).

4.7.2 RESULTS

As shown in paragraph 4.3, the Mg-rich Olivine used in these tests consists of three phases: Forsterite ($Fe_{0.2}Mg_{1.8}SiO_4$), Enstatite ferroan ($Fe_{0.2}Mg_{0.8}SiO_3$), and Clinochlore ($Al_{1.84}Fe_{0.5}H_8Mg_{4.5}O_{18}Si_{3.16}$). The Forsterite is the majority phase in the as-received olivine powders (91 wt%), with Enstatite as secondary phase (7.5 wt%).

After the mechanical activation, all the samples showed the characteristic bands of methane, CH_4, and carbon monoxide, CO, in the gas phase, analyzed by FT-IR spectroscopy. In addition to methane, at prolonged milling time, the samples also showed the characteristic bands of other hydrocarbons, such as ethane and propane, which were not included in the quantitative analysis.

Figure 4.7.3 shows the FTIR spectrum of the gas mixture for each test series.
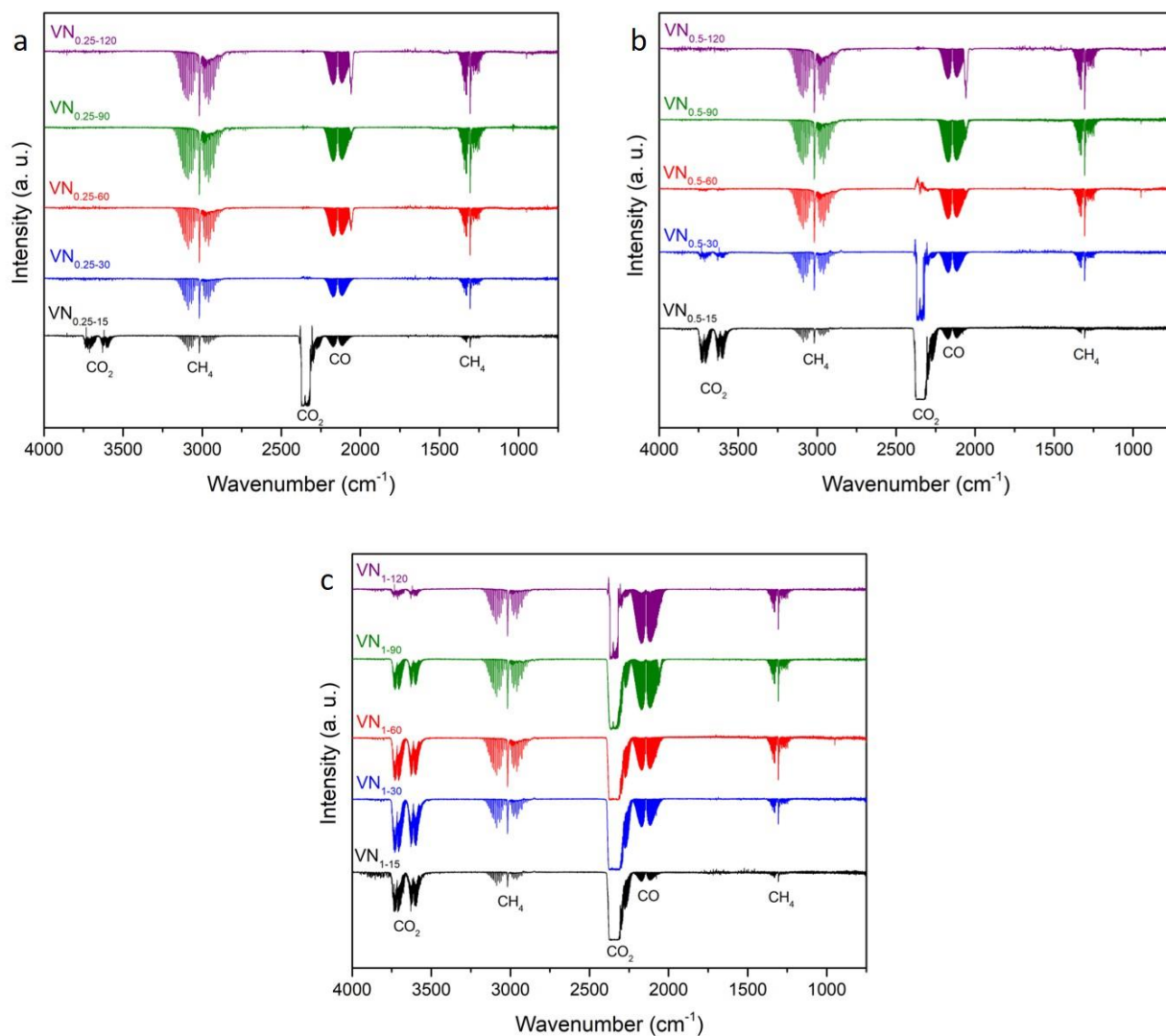
Figure 4.7.3: FTIR spectra of the gas mixtures as a function of the milling time. a) tests carried out at 0.25 bar of CO_2; b) tests carried out at 0.5 bar of CO_2; c) tests carried out at 1 bar of CO_2.

It can be seen that in the run series realized at an initial pressure of 0.25 bar (Fig. 4.6.3 (a)), after only 30 minutes of milling, carbon dioxide was completely converted. The FTIR spectra at prolonged milling times, indeed, did not show its characteristic bands. The same observation arises from the tests carried out at 0.5 bar (Fig. 4.7.3 b), where the total CO_2 consumption occurred after 60 min of milling. Finally, for the tests carried out at 1 bar, the CO_2 was not totally

converted even at the longest milling time. For each series of test, carbon monoxide is detected as a product of the reaction between olivine, water and CO_2. Hence, from these first results, seems that the reaction proceeds with a different mechanism than that observed in the previous tests carried out with the Spex mill, in which the presence of carbon monoxide in the gas phase has never been found (or at least not in a concentration above the detection limit). Comparing the total amount of methane produced during the mechanical treatment (Fig. 4.7.4), until 60 min of milling, an increasing amount of methane as been detected for each test. While after 90 min, some fluctuations have been observed in the produced amount.
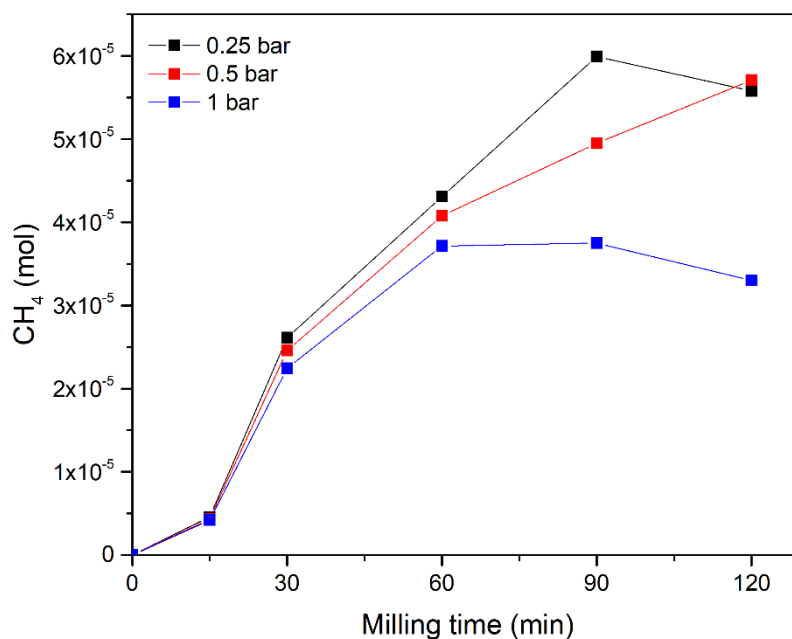
Figure 4.7.4: CH$_4$ evolution in function of the milling time for the three series of tests at different CO$_2$ pressure conditions.

It can be observed, from Figure 4.7.4, that the higher conversion to hydrocarbons occurred in the series carried out with a lower pressure of CO_2: 0.25 and 0.5 bar.

The comparison between the produced amount of methane and carbon monoxide as a function of the CO_2 pressure conditions (Fig. 4.7.5) evidenced that in the series at 0.25 and 0.5 bar of CO_2, the amount of methane is higher than the amount of CO; while at 1 bar, an opposite trend is observed at prolonged milling times. Therefore, the conversion to methane is favoured at lower partial pressure of CO_2.
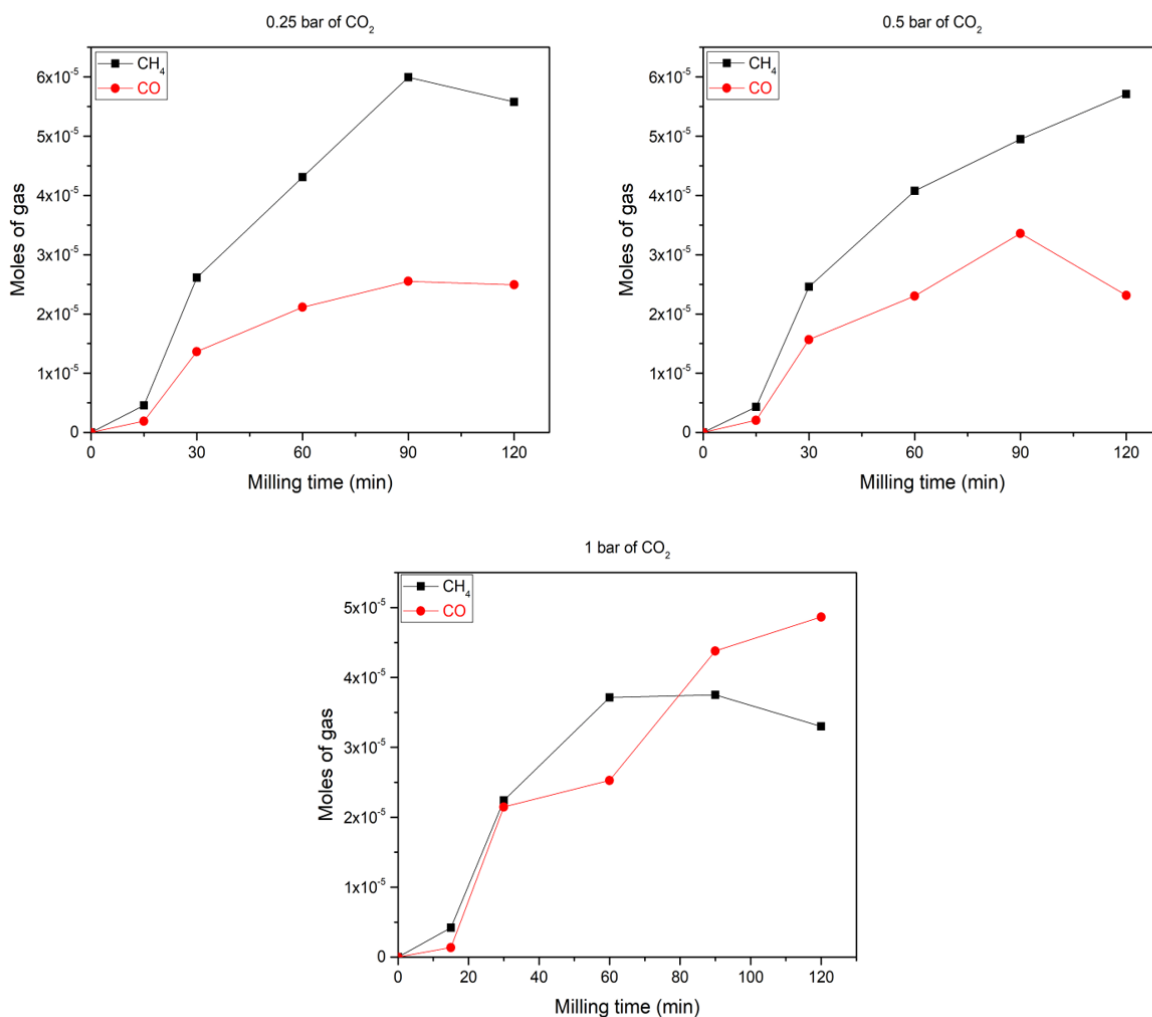
Figure 4.7.5: comparison between CH_4 and CO evolution for each serie of tests.

Since lower concentrations of CO_2 would favour methane production, additional tests were performed using the double amount of olivine, keeping the olivine/water ratio unchanged, and the same pressure of CO_2 in order to

verify how these different operative conditions can affect the conversion process.

Figure 4.7.6, shows the comparison between the total amounts of CH_4 and CO produced at 0.5 and 1 bar of CO_2. Working with a doubled amount of olivine and water, the quantity of carbon monoxide produced considerably decreases.
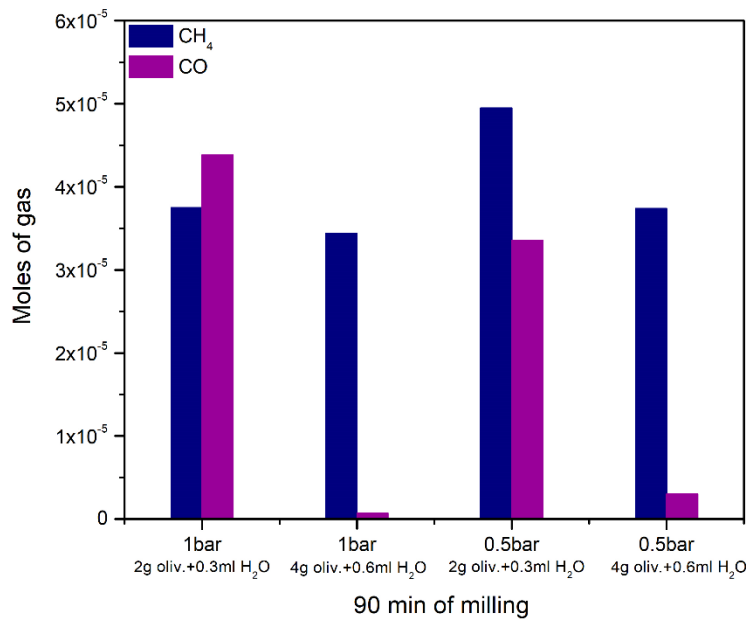
Figure 4.7.6: comparison between the absolute amount of methane and carbon monoxide, produced at 1 bar and 0.5 bar of CO_2, in different operative conditions.

Then, these operative conditions favour the direct conversion process (FTT type)[1,2] of CO_2 to methane (Eq. 4.7.1), not through the reversed water gas shift reaction (Eq. 4.7.2 e 4.7.3), which leads to the formation of carbon monoxide as intermediate of the reaction:

$$CO_2 + 4H_2 \rightarrow CH_4 + 2\,H_2O \qquad\qquad Eq.\ 4.7.1$$

$$CO_2 + H_2 \rightarrow CO + H_2O \qquad\qquad Eq.\ 4.7.2$$

$$CO + 3\,H_2 \rightarrow CH_4 + H_2O \qquad\qquad Eq.\ 4.7.3$$

These results are emphasized also by Figure 4.7.7, which report the CH_4/CO molar ratio as a function of the operative conditions. In particular, the best result is obtained at 1 bar of CO_2 with 4g of olivine and 0.6 ml of H_2O.
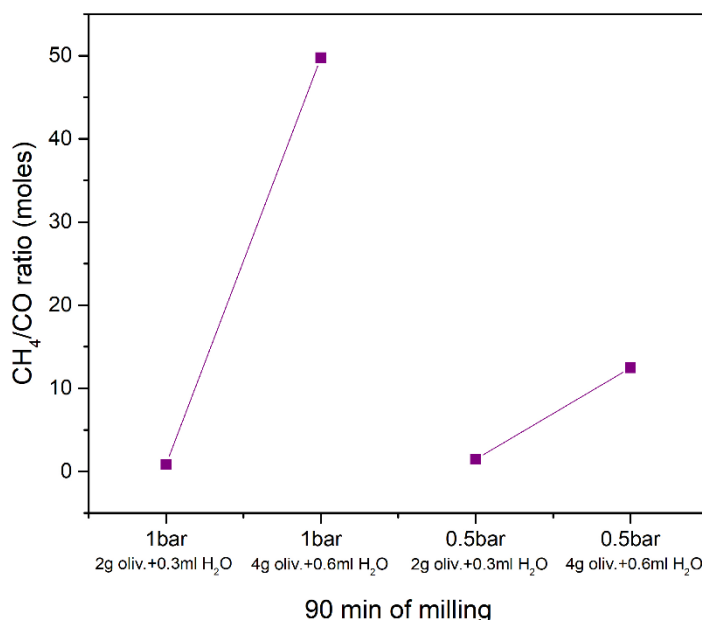
Figure 4.7.7: CH_4/CO molar ratio plotted as a function of the operative conditions.

Furthermore, comparing the FTIR gas measurements, shown in Figure 4.7.8, it was possible to observe that at 0.5 bar of CO_2 and the same time of milling (90 min) in both cases the CO_2 signal is absent because it was completely converted, but working with the double amount of olivine and water (green line), a lower amount of CO has been detected. The comparison of the tests carried out at 1 bar of CO_2 showed, working with doubled quantities, the total consumption of the CO_2 and the production of a lower amount of CO.
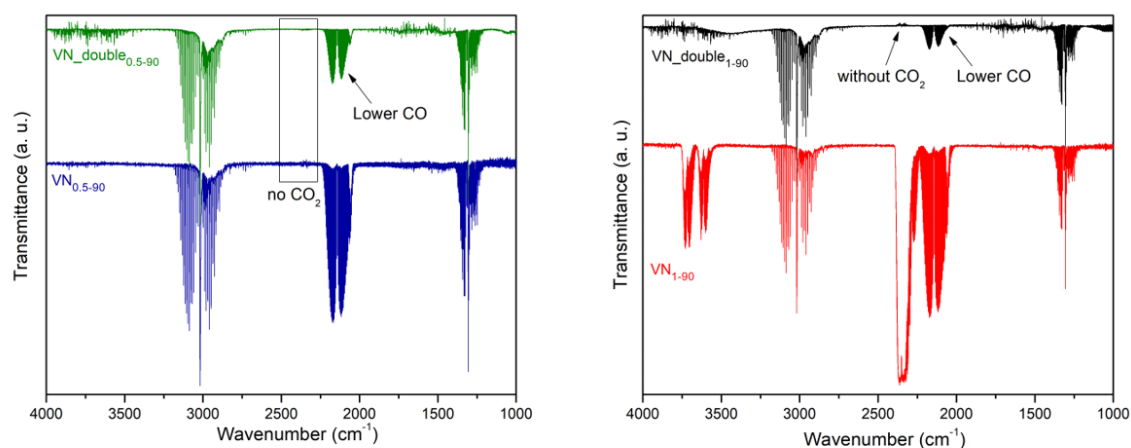
Figure 4.7.8: comparison of the FTIR spectra of the gas mixture a) tests at 0.5 bar of CO_2 and b) tests at 1 bar of CO_2.

The FTIR solid spectrum of pristine olivine is shown in Figure 4.7.9. The peaks positions compared with literature data[3-5], confirmed the XRD results (paragraph 4.3).
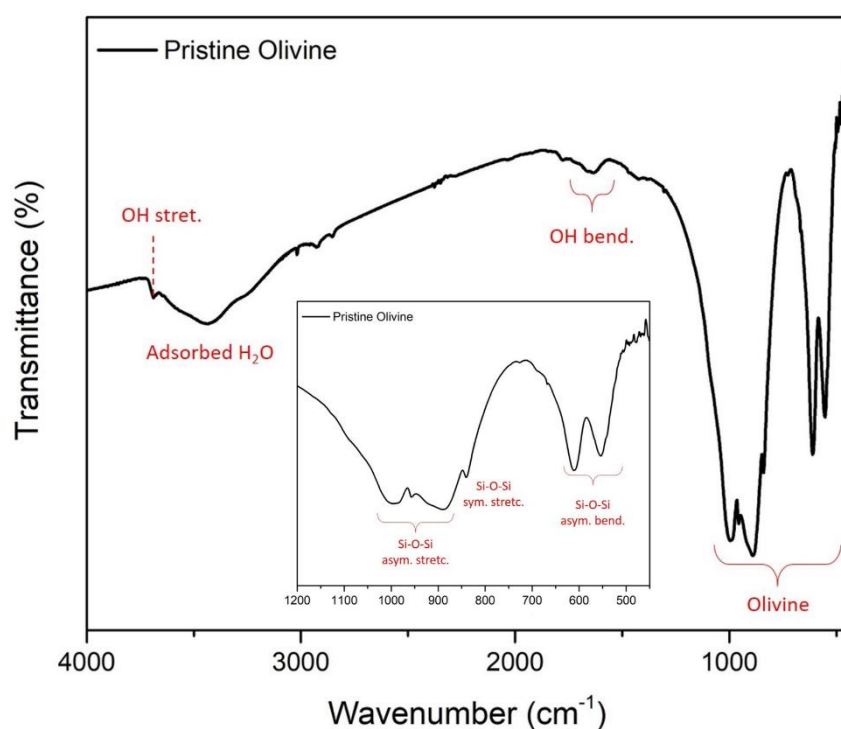
Figure 4.7.9: FTIR spectra of pristine Olivine powders: zoom of the peakss in the 1100 - 450 cm^{-1} region.

The bands in the region between 1100 - 450 cm^{-1} (zoom in Fig. 4.7.9) arise from olivine. Specifically, the peaks at 994, 957 and 888 cm^{-1} correspond to the asymmetric stretching of Si-O-Si groups; the peak at 839 cm^{-1} to the symmetric stretching.

The asymmetric bending peaks of the same functional groups are located at 609 and 553 cm^{-1}. The peak around 1664 cm^{-1} and 3688 cm^{-1} correspond respectively to the bending and stretching of O-H groups and the band at 3400 cm^{-1} to physisorbed water.

Figure 4.7.10 shows the FTIR spectra of the post milled samples (series of 1 bar of CO_2) compared with pristine olivine.
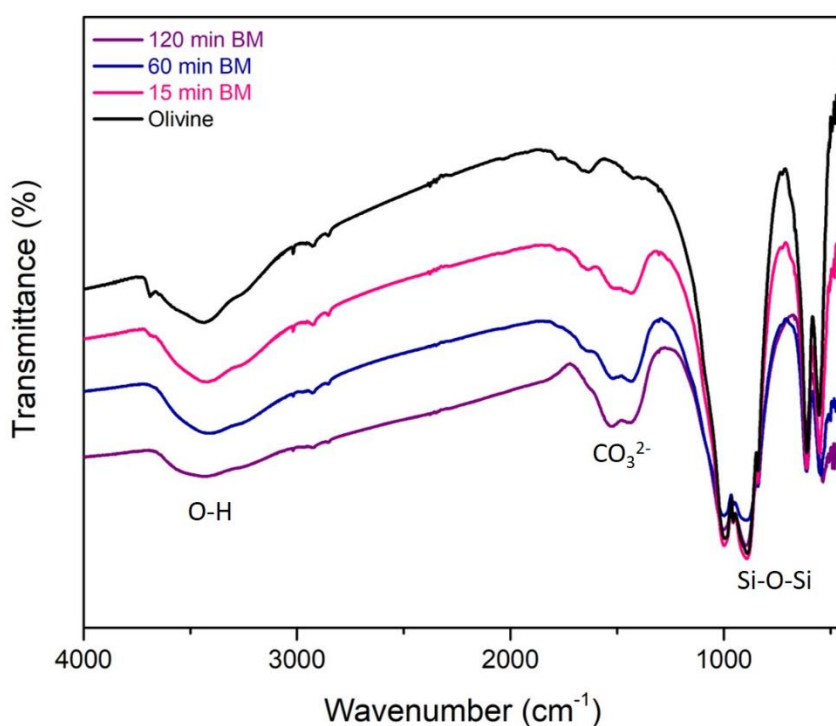
Figure 4.7.10: comparation between the FTIR solid spectra of some milled samples (under 1 bar of CO_2) with pristine Olivine.

These analyses evidenced the presence of two new peaks around 1500 cm^{-1} related to the carbonate group, CO_3^{2-} (with lower intensities for the series at 0.25 and 0.5 bar of CO_2), and the absence at prolonged milling times of the peaks at

3688 cm^{-1} related to the O-H groups, but still adsorbed water is present on the milled sample surface.

The presence of the characteristic bands of the carbonate group evidenced the formation of a carbonate phase after the mechanical treatment, with more intense signals at increasing CO_2 pressure. However, these results were not confirmed by XRD measurements, as shown in Figure 4.7.112, where are reported the XRD patterns of some samples milled under 1 bar of CO_2.
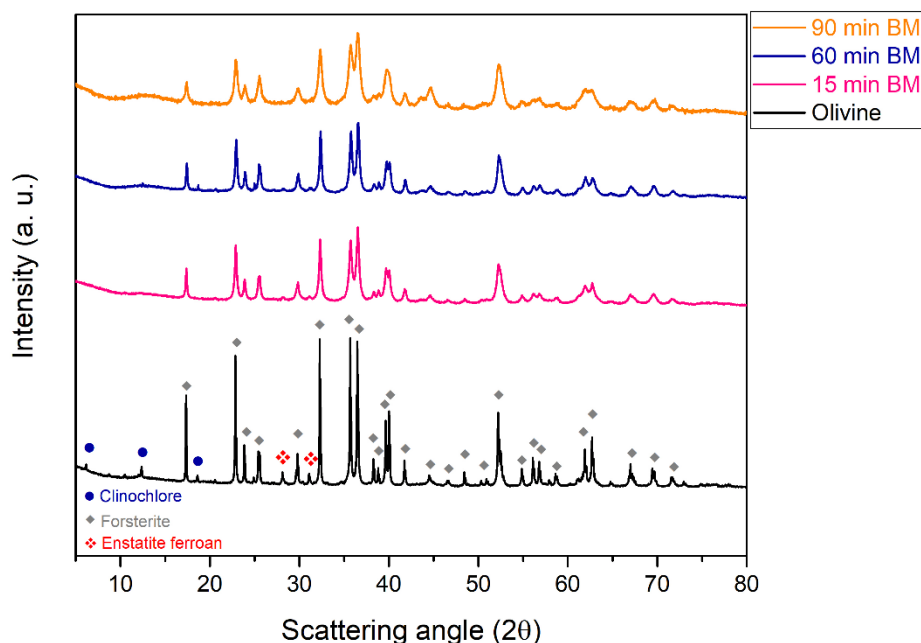

Figure 4.7.11: XRD patterns of some milled samples (under 1 bar of CO$_2$) compared with the pristine Olivine pattern. Experimental points are fitted by Rietveld refinement procedure.

It can be seen that after the milling, the only phase detected is Forsterite and any peaks indicating the presence of Mg-Fe carbonate phase have been observed. Moreover, the lower intensity of the Forsterite peaks is a consequence of the mechanical process that leads to generalized reflections broadening and

amorphization. So, in this case, the XRD analyses did not bring useful information for understanding the reaction mechanism.

In order to identify microstructural differences and the presence of crystalline carbonate phases in the samples, SEM images were collected at different milling times and compared to that of pristine olivine (Fig. 4.7.12). Figure 4.7.12 (a) shows the pristine olivine; figure (b) a sample milled for 15 minutes (under 0.5 bar of CO_2); figures (c) and (d) show the samples milled for 120 minutes in different pressure conditions, respectively 0.5 and 1 bar of CO_2. These last two showed no obvious microstructural differences, despite the different experimental conditions. The main evidence observed through this technique is the general decrease of particles dimensions, typical of the mechanical process. It was no possible to detect the presence of crystalline carbonate phases on the sample surface.
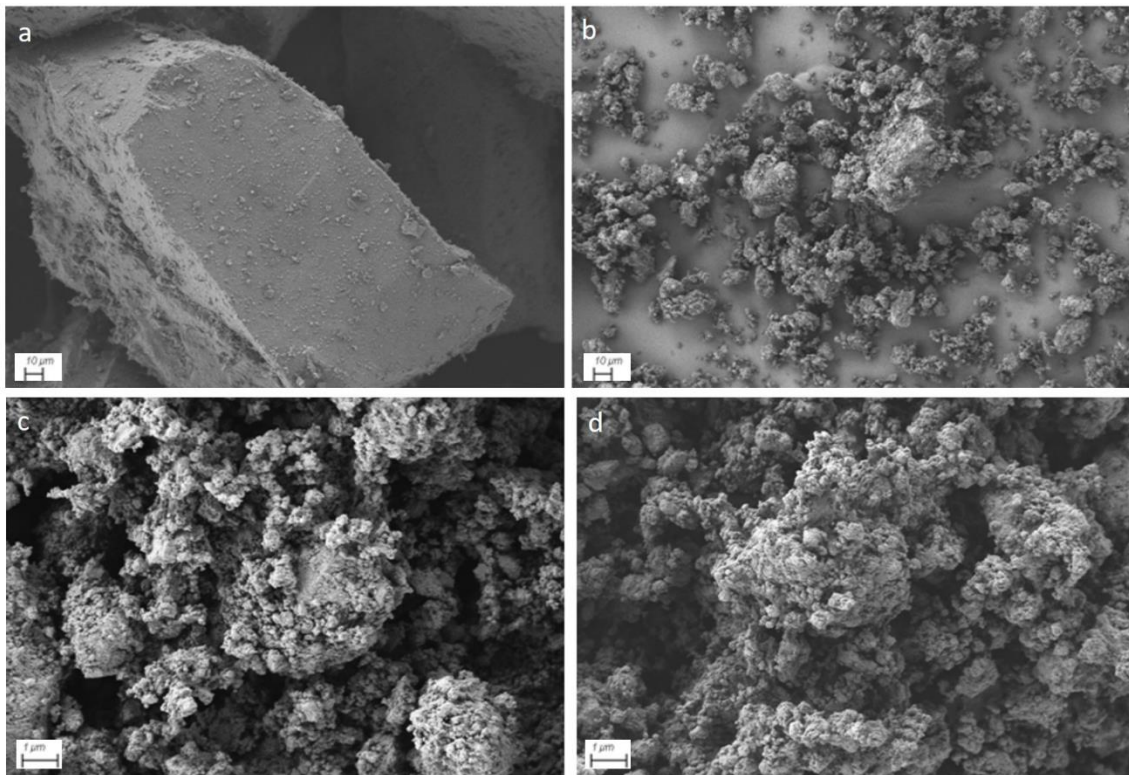
Figure 4.7.12: SEM images of: a) pristine Olivine; b) sample milled for 15 min under 0.5 bar of CO_2; c) sample milled for 120 min under 0.5 bar of CO_2; d) sample milled for 120 min under 1 bar of CO_2.

4.6.3 CONCLUSIONS

The mechanical activation of olivine with water under CO_2 pressure led to the production of CH_4 and light hydrocarbons, also using a planetary mill. The amount of methane is affected by the different operative conditions, in particular by the amount of olivine and water, and the partial pressure of CO_2. The lower mechanical energy transferred by planetary milling favoured the conversion process through a different mechanism that involves the formation of carbon monoxide as a reaction intermediates. The carbonate phase formation, evidenced by FTIR solid analyses but not confirmed by XRD measurements, set as future perspective the use of alternative characterization technique like Raman spectroscopy, to get useful information about the reaction mechanism. Finally, the optimization of the operative conditions, such as olivine/CO_2 ratio and the amount of olivine and water, will be the focus of future work in order to improve the chemical results and the knowledge of the process mechanism.

4.6.4 REFERENCES

[1]   A. Neubeck et al. (2011), Formation of H_2 and CH_4 by weathering of olivine at temperatures between 30 and 70°C, *Geochem. Trans.*, **12**, 1–10.

[2]   N. G. Holm et al. (2015). Serpentinization and the Formation of H_2 and CH_4 on Celestial Bodies (Planets, Moons, Comets). *Astrobiology*15, 587-600.

[3]   M. Fabian et al. (2010), The influence of attrition milling on carbon dioxide sequestration on magnesium-iron silicate, *Miner. Eng.* **23**, 616–620.

[4]   E. Turianicová E., P. Baláz (2008). A possible way to storage carbon dioxide on mechanically activated olivine (Mg, Fe)$_2$SiO$_4$. *VI Int. Conf. Mechanochemistry Mech. Alloy.* 316–319.

[5]   E. Turianicová et al.(2013). A comparison of the reactivity of activated and non-activated olivine with CO_2. *Int. J. Miner. Process.***123**, 73–77.

Chapter 5: *Conclusions*

The mineral carbonation technology is capturing wide interest as a useful strategy for both CO_2 storage and its utilization, and in this context, the chemical transformations driven by olivine weathering process appear worthy of investigation. In particular, while the very slow kinetics of the natural process is not practical for CO_2 storage and conversion purpose, the activation by mechanical treatment of olivine in the presence of H_2O and CO_2 has been demonstrated to be efficient to promote both the solid phases evolution and the gas-phase synthesis of light hydrocarbons, in particular of methane. The formation of carbonate solid phases and the methanation reaction, displayed faster kinetics compared to the hydrothermally activated ones and similar or higher conversion data. The whole pattern of physical and chemical transformations activated by mechanical treatment allowed to clarify some mechanistic aspects and suggested a possible line of future investigation. This process promoted H_2O dissociation with consequent H_2 formation, which in turn can promote FTT reactions over the mineral surface, and CO_2 hydrogenation rate can then increase, after an induction period related to CO_2 and H_2 activation, according to a sigmoidal trend often observed in mechanochemical processes. Structural evolution of solid phases suggests the occurrence of a complex process that appears to be defined by the CO_2/H_2O ratio values. The presence of a "mechanochemical effect" is evident, i.e., the occurrence of an increased system reactivity specifically related to the activation by mechanical treatment.

The observed concentration values of methane and hydrocarbons may be influenced by the experimental set up: the analyses of the effects of parameters

like the geometry reactor, as well as the milling dynamic parameter, i.e., frequency of collision.

Raman and Mössbauer spectroscopy proved to be useful techniques, complementary to X-ray diffraction. These techniques allowed to evidence the occurring of a *Serpentinization*-like process, i.e. the oxidation of the Fe II to Fe III of olivine, during the CO_2 conversion to light hydrocarbons, activated by mechanical treatment. Despite the remarkable evolution of H_2, in fact, through XRD analyses was not found the presence of any serpentine mineral on the samples powders to confirm the occurrence of the process.

The investigation of the influence of the energy impact, carried out modulating the vial motion frequency of the Spex mill, allowed to improve the knowledge of the reaction mechanism and to doubt that the carbonate formation is a competitive reaction with the CO_2 conversion, as we thought at first.

The modification of dynamic parameters, such as the transferred energy during the mechanical treatment using a different mill, Fritsch-type, revealed the different mechanism followed by the whole process, through the formation of carbon monoxide as intermediate. The use of complementary characterization techniques, as Raman spectroscopy and elementary analysis, to the carbon quantitative determination, will be the focus of future work aimed at deepening the knowledge of the process.

Conscious that methane is a potent greenhouse gas too, the future objects of this work will be aimed to optimize the obtained results and to evaluate the potential applications. In particular, through the development of a device based on our findings that will be used to capture the CO_2 from the atmosphere, perhaps directly from the main point sources such as power plants, oil refineries, etc., and to convert it into methane, that could be used as energy

source to the same plants. In this way, CO_2 would be led into a closed cycle, converted into a new resource and would no longer be an environmental issue.

ACKNOWLEDGEMENTS.